FACULTY OF ENGINEERING
DEPARTMENT OF CIVIL ENGINEERING
**STRUCTURAL MECHANICS**
KASTEELPARK ARENBERG 40 B-3001 HEVERLEE

KATHOLIEKE
UNIVERSITEIT
LEUVEN

# STUDY OF DETERMINING FACTORS FOR TRAFFIC INDUCED VIBRATIONS IN BUILDINGS

DWTC Research Programme Sustainable Mobility
Research Project MD/01/040

FINAL REPORT

BWM-2001-06

Geert LOMBAERT and Geert DEGRANDE

July 2001.

Repeat the title page here.

NOTE

This documentation was prepared with LaTeX.

# Acknowledgements

This research project is supported by the Prime Minister's Services of the Belgian Federal Office for Scientific, Technical and Cultural Affairs within the frame of the research programme Sustainable Mobility under contract number MD/01/040. This support is hereby gratefully acknowledged.

# Abstract

This report summarizes the results that have been obtained within the frame of the DWTC research project MD/01/040 'Study of determining factors for traffic induced vibrations in buildings' (1 July 1998 - 30 June 2001). The main objective of the project is to obtain more insight in the relevant physical phenomena and the relative importance of determining factors related to traffic induced vibrations.

Traffic vibration nuisance in buildings is mainly due to heavy lorries that pass at relatively high speed on a road with an uneven surface profile. Interaction between the wheels and the road surface causes a dynamic excitation which generates waves that propagate in the soil and impinge on the foundations of nearby structures.

As a part of this research project, a numerical model has been developed for the prediction of free field traffic induced vibrations. The model accounts for dynamic road-soil interaction (SSI) and includes a wide range of parameters that characterize the vehicle, the road and the soil.

A parametric study shows that the shape and the dimensions of the road unevenness, the mass of the vehicle's axles, the stiffness of the tyres and the damping of the suspension system determine the dynamic component of the axle loads. Compared to the characteristics of the soil, the road's characteristics have a negligible influence on the free field vibrations.

The numerical model has been validated by the results of two measurement campaigns where the truck's and the free field response have been measured during the passage on an artificial unevenness. Given the wide range of parameters and the uncertainty on these parameters, the model predicts the free field vibrations well, with a maximum ratio of 2 between the predicted and the measured signals.

# Contents

**Acknowledgements** iii

**Abstract** v

**Contents** vii

**List of Figures** xi

**List of Tables** xv

**1 Introduction** 1

1.1 Problem outline and motivation . . . . . 1

1.2 The aim of the present research . . . . . 2

1.3 The state of the art . . . . . 2

1.4 Outline of the text . . . . . 6

**2 The numerical model** 7

2.1 Introduction . . . . . 7

2.2 The dynamic axle loads . . . . . 7

2.2.1 The road surface unevenness . . . . . 7

2.2.2 The vehicle dynamics . . . . . 9

2.2.3 The equations of motion of the vehicle . . . . . 10

2.2.4 The vehicle-road interaction problem . . . . . 12

2.2.5 The vehicle frequency response functions . . . . . 12

2.3 The road-soil interaction problem . . . . . 14

2.3.1 Introduction . . . . . 14

2.3.2 The equations of motion of the road . . . . . 14

2.3.3 The road-soil transfer function . . . . . 17

2.4 The response to moving loads . . . . . 18

**3 Parametric study** **21**

3.1 Introduction . . . 21

3.2 The longitudinal road unevenness . . . 21

3.3 The vehicle FRF . . . 26

3.3.1 The vehicle FRF's for a Volvo FE7 truck model . . . 26

3.3.2 The influence of the suspension characteristics . . . 26

3.3.3 The influence of the tyre characteristics . . . 27

3.3.4 The influence of the mass of the vehicle body and the axles . . . 28

3.4 The dynamic axle loads . . . 29

3.4.1 A sine-shaped plateau . . . 29

3.4.2 A joint in the road surface . . . 30

3.5 The free field vibrations . . . 32

3.5.1 Introduction . . . 32

3.5.2 A sine-shaped plateau . . . 32

3.5.3 A joint in the road surface . . . 35

3.5.4 An alternative sine-shaped plateau . . . 37

3.5.5 The influence of the road's structure . . . 39

3.5.6 The influence of the soil's material damping . . . 41

3.5.7 The influence of the soil's stratification . . . 42

3.6 Conclusion . . . 45

**4 Experimental validation** **47**

4.1 Introduction . . . 47

4.2 Design of the experiment: the artificial unevenness . . . 48

4.3 The experimental configuration and data acquisition . . . 49

4.3.1 The truck's response . . . 50

4.3.2 The soil's response . . . 51

4.4 The numerical prediction model . . . 53

4.4.1 The vehicle model . . . 53

4.4.2 The road model . . . 55

4.4.3 The soil model . . . 57

4.5 The validation of the vehicle's response . . . 60

4.5.1 The predicted axle loads . . . 60

4.5.2 Time history and frequency content of the axles' response . . . 62

4.5.3 Peak acceleration of the axles' response . . . 63

4.6 The validation of the soil's response . . . . . 64
4.6.1 The road-soil interaction problem . . . . . 64
4.6.2 Time history and frequency content of the free field response . . . . . 66
4.6.3 Frequency content of the response for different vehicle speeds . . . . . 69
4.6.4 Peak particle velocity of the free field response . . . . . 70
4.7 Conclusion . . . . . 70

**5 Conclusions and further research** **75**

**Bibliography** **77**

**A Publications** **85**

# List of Figures


2.1 2D 4 DOF model for a passenger car. . . . . 9

2.2 Eigenmodes of the 2D 4-DOF model for a passenger car: (a) pitch and bounce motion mode; (b) axle hop mode. . . . . 11

2.3 The road-soil interaction problem. . . . . 14

3.1 The longitudinal road profile of a sine-shaped traffic bump (a) as a function of the coordinate $y$ along the road and (b) in the wavenumber domain. . . . . 22

3.2 The longitudinal road profile of a traffic plateau with a trapezoidal form (a) as a function of the coordinate $y$ along the road and (b) in the wavenumber domain. . . . . 23

3.3 The longitudinal road profile of a traffic plateau with sine-shaped ramps (a) as a function of the coordinate $y$ along the road and (b) in the wavenumber domain. . . . . 23

3.4 A comparison of the factor that distinguishes the wavenumber content of a plateau with a trapezoidal form (dash-dotted line) from a plateau with sine-shaped ramps (solid line) for ramps with a length $l = 1.20$ m. . . . . 24

3.5 The longitudinal road profile of a joint with a height $H = 0.02$ m (a) as a function of the coordinate $y$ along the road and (b) in the wavenumber domain. . . . . 25

3.6 The vehicle FRF's $\hat{h}_{f_k u_l}(\omega)$ of the 4 DOF Volvo FE7 truck model. . . . . 26

3.7 The vehicle FRF's of the original 4DOF Volvo FE7 truck model (solid line) and the same model whith the stiffness coefficient $k_{p2}$ of the front suspension multiplied by a factor of 1.5 (dash-dotted line). . . . . 27

3.8 The vehicle FRF's of the original 4DOF Volvo FE7 truck model (solid line) and the same model with the damping coefficient $c_{p2}$ of the front suspension multiplied by a factor of 1.5 (dashed line). . . . . 27

3.9 The vehicle FRF's of the original 4DOF Volvo FE7 truck model (solid line) and the same model with the stiffness coefficient $k_{t2}$ of the front tyre multiplied by a factor of 1.5 (dashed line). . . . . 28

3.10 The vehicle FRF's of the original 4DOF Volvo FE7 truck model (solid line) and the same model with the damping coefficient $c_{t2}$ of the front tyre multiplied by a factor of 1.5 (dashed line). . . . . 28

3.11 The vehicle FRF's of the original 4DOF Volvo FE7 truck model (solid line) and the same model with the mass $m_b$ of the vehicle body multiplied by a factor of 1.5 (dashed line). . . . . 28

3.12 The vehicle FRF's of the original 4DOF Volvo FE7 truck model (solid line) and the same model with the mass $m_{a2}$ of the front axle multiplied by a factor of 1.5 (dashed line). . . . . 29

3.13 (a) Frequency content $\hat{u}_{w/r}(\omega)$ of the unevenness, (b) FRF $\hat{h}_{f_1 u}(\omega)$, (c) frequency content $\hat{g}_1(\omega)$ and (d) time history $g_1(t)$ of the predicted rear axle load for the passage of the Volvo FE7 truck on a traffic plateau. . . . . 30

3.14 (a) Second order Chebyshev low-pass filter with a cut-off wavenumber $k_y = 2\pi/0.3$ rad/m and (b) comparison of the original (dash-dotted line) and filtered (solid line) wavenumber content $\tilde{u}_{w/r}(k_y)$ of the unevenness profile of a joint in a road surface. . . 31

3.15 (a) Frequency content $\hat{u}_{w/r}(\omega)$ of the unevenness, (b) FRF $\hat{h}_{f_1 u}(\omega)$, (c) frequency content $\hat{g}_1(\omega)$ and (d) time history $g_1(t)$ of the predicted rear axle load for the passage of the Volvo FE7 truck on a joint in a road surface. . . . . 31

3.16 Time history of the free field velocity $v_{si}(x, y = 0, z = 0, t)$ at a distance $x$, equal to 8, 24 and 40 m due to the passage of a Volvo FE7 truck on a traffic plateau with sine-shaped ramps. . . . . 33

3.17 Frequency content of the free field velocity $\hat{v}_{si}(x, y = 0, z = 0, \omega)$ at a distance $x$, equal to 8, 24 and 40 m due to the passage of a Volvo FE7 truck on a traffic plateau with sine-shaped ramps. . . . . 34

3.18 Time history of the free field velocity $v_{si}(x, y = 0, z = 0, t)$ at a distance $x$, equal to 8, 24 and 40 m due to the passage of a Volvo FE7 truck on a joint in the road surface. . 35

3.19 Frequency content of the free field velocity $\hat{v}_{si}(x, y = 0, z = 0, t)$ at a distance $x$, equal to 8, 24 and 40 m due to the passage of a Volvo FE7 truck on a joint in the road surface. 36

3.20 Time history of the free field velocity $v_{si}(x, y = 0, z = 0, t)$ at a distance $x$, equal to 8, 24 and 40 m due to the passage of a Volvo FE7 truck on a plateau with sine-shaped ramps with a length $l = 1.20$ m (dash-dotted line) and $l = 2.40$ m (solid line). . . . . 37

3.21 Frequency content of the free field velocity $\hat{v}_{si}(x, y = 0, z = 0, \omega)$ at a distance $x$, equal to 8, 24 and 40 m due to the passage of a Volvo FE7 truck on a plateau with sine-shaped ramps with a length $l = 1.20$ m (dash-dotted line) and $l = 2.40$ m (solid line). . . . . 38

3.22 Time history of the free field velocity $v_{si}(x, y = 0, z = 0, t)$ at a distance $x$, equal to 8, 24 and 40 m due to the passage of a Volvo FE7 truck on a traffic plateau with sine-shaped ramps for road section 1 (dash-dotted line) and road section 2 (solid line) where the thickness of the layers of section 1 is multiplied by a factor of 3. . . . . 39

3.23 Frequency content of the free field velocity $\hat{v}_{si}(x, y = 0, z = 0, \omega)$ at a distance $x$, equal to 8, 24 and 40 m due to the passage of a Volvo FE7 truck on a traffic plateau with sine-shaped ramps for road section 1 (dash-dotted line) and road section 2 (solid line) where the thickness of the layers of section 1 is multiplied by a factor of 3. . . . . 40

3.24 Time history of the free field velocity $v_{si}(x, y = 0, z = 0, t)$ at a distance $x$, equal to 8, 24 and 40 m due to the passage of a Volvo FE7 truck on the traffic plateau with sine-shaped ramps for the case where the soil's hysteretic damping ratio $\beta$ equals 0.025 (dash-dotted line) and 0.050 (solid line). . . . . 41

3.25 Frequency content of the free field velocity $\hat{v}_{si}(x, y = 0, z = 0, \omega)$ at a distance $x$, equal to 8, 24 and 40 m due to the passage of a Volvo FE7 truck on the traffic plateau with sine-shaped ramps for the case where the soil's hysteretic damping ratio $\beta$ equals 0.025 (dash-dotted line) and 0.050 (solid line). . . . . 42

3.26 Time history of the vertical free field velocity $v_{sz}(x, y = 0, z = 0, t)$ at a distance $x$, equal to 8, 24 and 40 m due to the passage of a Volvo FE7 truck on a traffic plateau with sine-shaped ramps for a road supported by (a) a homogeneous halfspace, (b) a layer built in at its base and (c) a single layer on a halfspace. . . . . 43

3.27 Frequency content of the vertical free field velocity $\hat{v}_{sz}(x, y = 0, z = 0, \omega)$ at a distance $x$, equal to 8, 24 and 40 m due to the passage of a Volvo FE7 truck on a traffic plateau with sine-shaped ramps for a road supported by (a) a homogeneous halfspace, (b) a layer built in at its base and (c) a single layer on a halfspace. . . . . 44

4.1 The passage of a DAF FT85 truck and trailer on the artificial unevenness at the DAF test circuit in Sint-Oedenrode (The Netherlands). . . . . 47

4.2 Top and side view of the artificial profile. . . . . 48

4.3 The longitudinal profile of the artificial unevenness (a) as a function of the coordinate $y$ along the road and (b) in the wavenumber domain. . . . . 49

4.4 The unevenness experienced by the vehicle at a speed (a) $v = 30$ km/h, (b) $v = 50$ km/h and (c) $v = 70$ km/h. . . . . 49

4.5 The profile installed at the test site. . . . . 50

4.6 The accelerometers on the front part of the vehicle body and the front axle. . . . . 51

4.7 Position of the measurement line and the accelerometers. . . . . 51

4.8 View from the end of the measurement line towards the road. . . . . 52

4.9 The accelerometers FF2y, FF2z and FF2x (from left to right) mounted on aluminium stakes with a cruciform cross section. . . . . 52

4.10 Stabilization diagram with the SSI method. The symbols in this diagram represent respectively: '$\oplus$' a stable pole; '.v' a pole with a stable frequency and vector; '.d' a pole with a stable frequency and damping; '.f' a pole with a stable frequency and '.' a new pole. . . . . 54

4.11 Modulus of the FRF $\hat{h}_{f_k u_l}(\omega)$ for the 2D 4 DOF vehicle model of the Volvo FL6 truck. 55

4.12 Experimental configuration with two geophones in a common mid-point configuration with a distance of 0.80 m between the geophones. . . . . 56

4.13 The experimental dispersion points as obtained by the SASW test on the road. . . . . 56

4.14 The experimental dispersion points and the experimental dispersion curve. . . . . 58

4.15 The cone and the hydraulic press. . . . . 59

4.16 (a) The shear wave velocity profile as determined by means of the SASW method (dash-dotted line), the SCPT method (crosses) and the theoretical profile (solid line) and (b) the longitudinal wave velocity profile as determined by means of the SCPT method (crosses) and the theoretical profile (solid line). On figure (a), the results of the SASW test and the theoretical profile coincide upto a depth of 8.20 m. . . . . 59

4.17 (a) Frequency content $\hat{u}_{w/r}(\omega)$ of the experienced unevenness, (b) FRF $\hat{h}_{f_2 u}(\omega)$, (c) frequency content $\hat{g}_2(\omega)$ and (d) time history $g_2(t)$ of the predicted front axle load for a passage of the Volvo FL6 truck on the artificial profile at a vehicle speed $v = 30$ km/h. 61

4.18 (a) Frequency content $\hat{u}_{w/r}(\omega)$ of the experienced unevenness, (b) FRF $\hat{h}_{f_2u}(\omega)$, (c) frequency content $\hat{g}_2(\omega)$ and (d) time history $g_2(t)$ of the predicted front axle load for a passage of the Volvo FL6 truck on the artificial profile at a vehicle speed $v = 58$ km/h. 61

4.19 Predicted (solid line) and measured (dash-dotted line) time history (left hand side) and frequency content (right hand side) of the acceleration of the front axle for vehicle speeds $v = 30\,\text{km/h}$ (top) and $v = 58\,\text{km/h}$ (bottom). . . . . 62

4.20 Predicted (solid line) and measured (dash-dotted line) time history (left hand side) and frequency content (right hand side) of the acceleration of the rear axle for vehicle speeds $v = 30\,\text{km/h}$ (top) and $v = 58\,\text{km/h}$ (bottom). . . . . 63

4.21 Predicted (circles) and measured (crosses) peak axle acceleration of (a) the front axle and (b) the rear axle as a function of the vehicle speed. . . . . 64

4.22 (a) soil model 1 for the calculation of the soil's impedance and (b) soil model 2 for the calculation of the transfer functions. . . . . 65

4.23 The frequency content of the radial (left hand side) and vertical (right hand side) component of the free field velocities at 8 m, 16 m and 24 m for a concentrated vertical pulse at the free surface of soil model 1 (solid line) and at the interface between the layers 1 and 2 of soil model 2 (dash-dotted line). . . . . 65

4.24 Time history of the predicted (solid line) and the measured (dash-dotted line) free field velocity at 8 m, 16 m and 24 m for a vehicle speed $v = 30\,\text{km/h}$ (passage v30c). . . . . 67

4.25 Frequency content of the predicted (solid line) and the measured (dash-dotted line) free field velocity at 8 m, 16 m and 24 m for a vehicle speed $v = 30\,\text{km/h}$ (passage v30c). . 68

4.26 Time history of the predicted (solid line) and the measured (dash-dotted line) free field velocity at 8 m, 16 m and 24 m for a vehicle speed $v = 58\,\text{km/h}$ (passage v60b). . . . . 69

4.27 Frequency content of the predicted (solid line) and the measured (dash-dotted line) free field velocity at 8 m, 16 m and 24 m for a vehicle speed $v = 58\,\text{km/h}$ (passage v60b). . 70

4.28 Frequency content of (a) the acceleration of the front and (b) the rear axle of the truck and frequency content of the vertical free field velocity at (c) 8 m and (d) 24 m from the center of the road for vehicle speeds $v = 30\,\text{km/h}$, $v = 40\,\text{km/h}$, $v = 49\,\text{km/h}$ and $v = 58\,\text{km/h}$ (from top to bottom). . . . . 71

4.29 Predicted (circles) and measured (crosses) peak particle velocity of the free field response at a distance $x$ equal to 8 m, 16 m and 24 m as a function of the vehicle speed. . . . . 72

4.30 Predicted (circles) and measured (crosses) peak particle velocity of the vertical free field response at a distance $x$ equal to 32 m, 40 m and 48 m as a function of the vehicle speed. 72

# List of Tables


2.1 Classification of road roughness. . . . . 8

2.2 ISO 8608 road roughness classification ($k_{y0} = 1$ rad/m). . . . . 9

2.3 Eigenmodes of the 4DOF Volvo FE7 model. . . . . 11

3.1 Road section. . . . . 32

3.2 Vertical peak particle velocity (mm/s) for the passage of a Volvo FE7 truck on a sine-shaped plateau with ramps with a length $l = 1.20$ m and $l = 2.40$ m. . . . . 37

3.3 Road section 2. . . . . 39

3.4 Vertical peak particle velocity (mm/s) for the passage of a Volvo FE7 truck on a traffic plateau for road section 1 and road section 2 where the thickness of the layers of section 1 is multiplied by a factor of 3. . . . . 40

3.5 Vertical peak particle velocity (mm/s) for the passage of a Volvo FE7 truck on a traffic plateau for the case where the soil's hysteretic damping ratio $\beta$ equals 0.025 and 0.050. 42

3.6 Road profile. . . . . 44

4.1 Front axle mass, rear axle mass and total mass in empty and full loading state. . . . . 53

4.2 Estimated and predicted eigenfrequencies of the Volvo FL6 truck. . . . . 53

4.3 Vehicle data provided by the truck manufacturer for the Volvo FL6 truck. . . . . 54

4.4 Road section. . . . . 56

4.5 The theoretical road profile. . . . . 57

4.6 Final profile after an inversion procedure with 3 layers on a halfspace. . . . . 58

4.7 The theoretical soil profile. . . . . 60

# Chapter 1

# Introduction

## 1.1 Problem outline and motivation

Ground-borne traffic induced vibrations in buildings are a matter of growing environmental concern. The increasing volume of road traffic, the higher vehicle speeds and the increasing axle loads are generally referred to as the cause for the increasing hindrance due to vibrations induced by road traffic. Considering rail traffic, vibration nuisance is related to increasing train speeds and increasing freight loads. Belgium is an important link in the European high speed train network.

Foreign norms and guidelines recognize discomfort to people, malfunctioning of sensitive equipment and damage to buildings as possible consequences of vibrations. An extensive survey by Morton-Williams et al. [1] of Social and Community Planning Research in the UK has shown that 37 % of the population is bothered by ground-borne vibrations, while 8 % is seriously bothered. Whereas 90 % of the respondents reports nuisance due to noise, the number of people seriously bothered by vibrations (8 %) has the same order of magnitude as the number of people seriously bothered by noise (9 %). In the MIRA-2 report, 7 % of the people is estimated to be seriously bothered by vibrations. Road traffic is the most important source (65 %), whereas other sources are railway traffic (16 %), industrial activities (15 %) and building construction (4 %). Between 1995 and 2000, the Department of Environment and Infrastructure of the Ministry of the Flemish Community that is responsible for the maintenance of the regional road network in Flanders has performed a total of 51 measurements to evaluate nuisance and the possibility for damage due to traffic induced vibrations [2].

The existing gap in knowledge regarding the physical interpretation of in situ measurements, the formulation of norms and guidelines defining allowable vibration levels and the estimation of the efficiency of vibration isolating measures justify continuing scientific research.

Traffic vibration nuisance in buildings is mainly due to heavy lorries that pass at relatively high speed on a road with an uneven surface profile. Interaction between the wheels and the road surface causes a dynamic excitation which generates waves that propagate in the soil and impinge on the foundations of nearby structures. After attenuation at the foundation level, vertical vibration components can be amplified at the resonance frequencies of flexible floors, while the horizontal components are amplified over the height of the building. Dominant frequencies are typically situated in a low frequency band between 8 and 20 Hz.

## 1.2 The aim of the present research

The objective of the DWTC research project MD/01/040 'Study of determining factors for traffic induced vibrations in buildings' is to obtain more insight in the relevant physical phenomena and the relative importance of determining factors related to traffic induced vibrations. Within the frame of the 'Sustainable Mobility' programme of the Prime Minister's Services of the Belgian Federal Office for Scientific, Technical and Cultural Affairs, only the present research project deals with the problem of traffic induced vibrations.

As a part of this research project, a numerical model is developed for the prediction of traffic induced vibrations. The model accounts for dynamic soil-structure interaction (SSI) and includes a wide range of parameters that characterize the vehicle, the road unevenness, the road and the soil. In situ measurements are used to perform an experimental validation and demonstrate the predictive qualities of the numerical model. Furthermore, the model will be used to perform an extensive parametric study that allows to identify the determining factors ("pressures") for traffic induced vibrations in buildings and the measures ("responses") that can be taken to diminish or avoid problems related to ground-borne vibrations. The development of the numerical model and the results support the development of other numerical models for the prediction of railway induced vibrations or the vibrations induced by underground metro or tram traffic.

Compared to the project proposal, considerably more effort has been put in the development and the experimental validation of the source module. As a result, less attention has been spent to the study of the interaction of the incident wave field and structures nearby the road. Preliminary results [3], however, have been obtained during a 6 months post-doctoral stay of Dr. Anita Uscilowska of the Institute of Mathematics of the Poznan University of Mathematics in Poznan (Polen) within the frame of the DWTC programme 'Scientific and Technology Cooperation with Central and Eastern Europe'.

For a medium long period, the results of the research project support the development of a sustainable mobility policy. The insight that has been gained can be used to formulate national or international guidelines for nuisance due to traffic induced vibrations. Furthermore, the results of the extensive parametric study show the effectiveness of measures such as a limitation of the gross vehicle weight, a speed limit, an alternative design of a traffic plateau and an adjustment of the road's structure.

These results are not only of great importance to the administrations that are responsible for the maintenance of the road network, but also to contractors or consulting engineers that are confronted with problems related to traffic induced vibrations.

In the following, the state of the art that has been achieved in the experimental and theoretical study of road traffic induced vibrations is briefly revised. Special emphasis goes to studies in which the link between structural damage and ground-borne vibrations is investigated and to a description of existing theoretical models.

## 1.3 The state of the art

### Experimental research

The Transport and Road Research Laboratory (TRRL) in Crowthorne, Berkshire (UK) has performed a lot of experimental research related to traffic induced vibrations in the past twenty years. Several surveys were carried out to investigate the causes and the relation between the degree of nuisance experienced by residents and their exposure to traffic noise and vibrations [4, 5]. At a particular site, the dynamic properties of the vehicle's suspension system, the vehicle speed and the elevation of the

road surface unevenness determine the vibration levels [6]. Heavy goods vehicles and buses are found to produce the most perceptible vibrations. Discrete irregularities in the road surface dominate the more continuous vibrations induced by the global road unevenness. The TRRL has also performed tests to determine the discomfort experienced by people both in vehicles and nearby houses due to road humps and speed control cushions [7]. The results of these tests have been translated by the Department of the Environment, Transport and Regions in the UK into practical guidelines in several advisory leaflets [8, 9].

Based on experimental observations, Al-Hunaidi et al. [10, 11] have found that the axle hop frequency of the Montréal city buses is close to the first natural frequency of the soil at this site. It was therefore concluded in this study that the level of vibration nuisance can be reduced when the properties of the suspension system of the buses are modified to achieve an axle hop frequency that is below the cut-off frequency of the soil.

In order to confirm the experimental observations, a numerical model that incorporates the vehicle, the road and the soil is indispensible.

### Damage due to traffic induced vibrations

The results of a questionnaire [5] by the Transport and Road Research Laboratory (TRRL) in the UK indicate that an important cause for people to be bothered by traffic induced vibrations is the fear that these vibrations damage their property. In several surveys by the TRRL [12, 13, 14], the possible link between vibrations and damage to heritage buildings is investigated. In all cases, however, it is found that the observed structural damage is due to other site-related factors rather than traffic induced vibrations.

Sutherland [15] has performed a detailed investigation of possible structural damage due to vibrations induced by trolley buses in the city of Winnipeg, Canada in 1949. Artificial ramps with a height of 0.03 m to 0.08 m and a length of approximately 0.30 m have been installed on roads to generate vibration levels in buildings that are exceptionally high. The vibration levels, however, are still much lower than the treshold values reported for minor structural damage as plaster cracking. Sutherland indicates that the treshold for human perception is much lower than the one for damage and concludes that vibrations that would barely cause plaster cracking can already be very uncomfortable to people.

Bocquenet [16] discusses 4 practical cases of structural damage due to road traffic induced vibrations between 1950 and 1960. In two of these cases, the vibrations have caused fatigue effects of brittle materials [17]. In the two other cases, the damage is due to settlements that are presumably caused by traffic induced vibrations [18]. Heller [19] has also found that vibrations induced by railway or tramway traffic lead to a compaction of sandy soils in the immediate vicinity of the railway track. Peak particle velocities upto 2 mm/s at the foundation level are reported.

At the TRRL, the possibility of building damage due to vibration induced soil densification has been investigated experimentally [20]. During four months, a two-storey house, founded on a medium to low density dry sand layer, has been subjected to vibrations induced by a hydraulic vibrator, mounted on a small area of flexible pavement surface. The house was subjected to 888000 vibrator pulses with a fundamental frequency of 12 Hz and a duration of 1 s, equivalent to the passage of 4 vehicle axles. At the foundation level, peak particle velocities (PPV) have been measured between 2.5 mm/s close to the source and 1 mm/s at larger distances. Although a settlement of 22 mm was measured under the vibrator pad, no significant building settlements have been recorded. Furthermore, only a small amount of additional plaster cracking at wall-ceiling junctions has been observed. Similar to the observations by Sutherland, it is concluded that, for any risk of damage to exist at all, considerable hindrance has to be experienced.

House gives an extensive overview of criteria that are used to evaluate the possibility for damage [21]. Compared to the treshold value of 0.3 mm/s for human perception, much higher values are reported for structural damage. For minor damage to buildings, such as plaster cracking, the treshold value of the peak particle velocity equals 5 mm/s at a frequency of 10 Hz [21]. House indicates that a further investigation of the generation and propagation of the waves in the free field and the relation between the incident wave field and the building response is required. An experimentally validated numerical prediction model is a well suited instrument for this task.

Even when the mechanisms and the possibility for damage are not entirely clear, Watts [1] conludes that the nuisance by traffic induced vibrations justifies the development of prediction tools to determine whether a road surface defect is likely to cause problems related to hindrance.

### Empirical models

Empirical prediction models formulate the experimental experience into practical rules of thumb. These models account in an approximating way for the attenuation of the vibrations with distance and resulting from soil-structure interaction.

The extensive database of measurements that has been collected by the TRRL leads to the development of a formula [1, 14] that predicts the PPV as:

$$\text{PPV} = 0.028H\left(\frac{v}{48}\right) sp\left(\frac{r}{6}\right)^n \tag{1.1}$$

where $H$ represents the maximum height or depth of a surface unevenness (in mm), $v$ the vehicle speed (in km/h), $p$ is a factor that indicates wether the defect is present in one ($p = 0.75$) or both ($p = 1$) wheel paths and $r$ is the distance between the source and the receiver. $s$ and $n$ are two parameters that characterize the soil. The value of $s$ follows from the modulus of the ground transfer function at a distance of 6 m and a frequency of 12 Hz, while the value of $n$ determines the attenuation with the distance from the source. Both parameters have been experimentally determined at several sites with different soil characteristics, where free field vibrations are generated on a road with a falling weight device (FWD) [22]. For an unevenness with a height $H$ of 10 mm in both wheel paths ($p = 1$), a speed $v = 50$ km/h and an average value of 1 for $s$, the predicted PPV at 6 m is 0.3 mm/s, corresponding to the treshold level for human perception. The empirical model has been used to develop guidelines for the minimum distance between a road hump and a building as a function of the type of subsoil [9]. Based on the range of moduli and attenuation coefficients, predictions can differ by a factor of 4 for a single soil type, however.

Jakobsen presents an empirical model for the prediction of the vibration level inside a building from the one third-octave spectrum of the free field response close to a railway line [23]. For each one third-octave band, an experimentally determined constant value is added to predict the attenuation with distance and the attenuation that results from the interaction between the building and the subsoil. It is indicated that the predictions can differ upto 10 dB, or a factor of 3, from the actual vibration levels. Other empirical models make use of an experimental transfer function between the source and the receiver [24]. This approach offers the advantage that all relevant phenomena in the transmission path are implicitly accounted for.

Empirical models, however, do not clarify the mechanisms involved, are not suited for parametric studies and cannot be used for an extrapolation to more complex situations.

### Theoretical models

Theoretical models contain elements that are related to the source, the transmission path and the receiver. These models are well suited to investigate the physical phenomena related to traffic induced vibrations, as put forward by House [21], Hill [25], Watts [14] and Block [26].

The study of traffic induced vibrations is a three-dimensional (3D), dynamic soil-structure interaction problem, where wave propagation in the soil couples the source and the receiver. Three subproblems can be distinguished: the characterization of the source, wave propagation in the soil and the interaction of the incident wave field and the structure. At present, there are no coupled models that incorporate both the source and the receiver. The following discussion is therefore restricted to the prediction of free field vibrations. The models that are presently used for road and railway induced vibration have important common elements and are therefore discussed simultaneously.

Traffic induced vibrations are generated by the moving axle loads of the vehicle. A distinction can be made between the static component that follows from the distribution of the weight of the vehicle and the dynamic component that is determined by the interaction between the vehicle and the substructure. The contribution of the static component is referred to as the quasi-static excitation, which is important in the near field and when the vehicle speed is close to or larger than the wave velocities in the soil.

The dynamic component of the axle loads is induced by the road surface unevenness that subjects the vehicle to vertical oscillations. The dynamic axle loads are determined by the vehicle characteristics, the vehicle speed, the road unevenness and the deformations of the road. However, as the road is much stiffer than the vehicle's suspension or tyres [27, 28, 29, 30, 31, 32], the calculation of the dynamic axle loads can be uncoupled from the calculation of the soil response in a first approximation. The vehicle models that are used to describe the dynamic behaviour of a vehicle are composed of discrete masses, springs, friction elements and dampers [27, 33, 34, 31, 35, 36]. In the case where a linear vehicle model is used, vehicle frequency response functions (FRF) facilitate the calculation of the axle loads [27, 37, 33]. Local road unevenness is described by a deterministic function that represents the deviation of the traveled surface from a true planar surface. Global road unevenness can also be described in a stochastic way by a power spectral density (PSD) [38, 39]. Although the global road unevenness is frequently taken into account in theoretical studies [40, 33], practical vibration problems are seldomly related to the global road unevenness. Discrete irregularities that produce impact-like forces are more important [41, 14]. Very recently, prediction models for free field traffic induced vibrations have been used in the UK [7] and the Netherlands [42, 43, 44, 45] to estimate the vibration nuisance from road humps and speed regulators.

The calculation of the response to moving loads is often based on the dynamic reciprocity theorem [46] or a Galilean coordinate transformation to a moving frame of reference. Müller [47] and Müller and Huber [48] have solved the problem of a layered visco-elastic halfspace subjected to a moving load in the frequency-wavenumber domain. In an analogous way, de Barros and Luco [49, 50] have studied the steady-state response of a layered visco-elastic halfspace due to a constant moving load. For a problem geometry that is invariant in the direction in which the vehicle moves, Clouteau [51] and Aubry et al. [52] have proposed an efficient solution procedure where the longitudinal coordinate is transformed to the longitudinal wavenumber.

The contact forces between the road or the track and the soil are determined by the dynamic interaction between the substructure and the soil. A thin layer method has been applied by Mamlouk and Davis [53] to simulate the dynamic response of a pavement. Hardy and Cebon [29, 54] have modelled the road as a beam on a Winkler foundation. A comprehensive overview of road-soil interaction models is given by Cebon [27]. For the prediction of the vibrations in the free field, however, the presence of the road is often disregarded and the axle loads are applied directly to the soil [55, 40, 56, 57].

## 1.4 Outline of the text

In this report, the study of the determining factors of ground-borne vibrations due to road traffic is discussed.

Chapter 2 deals with the numerical model that has been developed. The free field vibrations are predicted in two stages. In chapter 3, the numerical model is used to study the importance of a wide range of parameters that characterize the shape and the dimensions of the road unevenness, the dynamic vehicle characteristics, the road's section, the soil's stratification and the material damping in the soil. In chapter 4, it is shown how in situ measurements are used for the experimental validation of the numerical model. Both the prediction of the vehicle's response and the free field response are validated. The results are summarized finally in chapter 5. Furthermore, it is indicated how further research can additionally contribute to a further understanding of the relevant phenomena. In appendix A, it is shown how the experience and the knowledge that have been gained within the project are distributed at both the national and international level.

# Chapter 2

# The numerical model

## 2.1 Introduction

In the following, a numerical model for the prediction of free field road traffic induced vibrations is presented. The prediction is performed in two stages. First, the dynamic axle laods are calculated from the road unevenness and the vehicle dynamics. Next, the dynamic Betti-Rayleigh reciprocal theorem is applied to calculate the free field vibrations from the axle loads and a transfer function between the road and a point in the free field. The calculation of the transfer function requires the solution of the dynamic road-soil interaction problem for the case where a pulse load is applied at the road's surface.

## 2.2 The dynamic axle loads

The vehicle's vertical axle loads are composed of a static and a dynamic component. The static component follows from the distribution of the vehicle weight over the vehicle axles. The dynamic component is induced by the road unevenness that subjects the vehicle to vertical oscillations. It depends on the road unevenness, the vehicle characteristics and the vehicle speed. In the case where the vehicle speed is low compared to the wave velocities in the soil, the contribution of the static component to the free field vibrations is negligible. In this chapter, it is shown how vehicle frequency response functions are used to predict the dynamic component of the vertical interaction forces between the vehicle and the road.

### 2.2.1 The road surface unevenness

The road unevenness is defined as the deviation of a traveled surface from a true planar surface with characteristic dimensions that affect ride quality, vehicle dynamics, dynamic pavement loads and pavement drainage [58]. Road unevenness can be either local or global. Local road unevenness is only present at a limited distance along the road, while global road unevenness corresponds to the overall unevennes along the road. For a 2D vehicle model, only the longitudinal unevenness profile $u_{w/r}(y)$ that represents the deviation at a point $y$ along the road is considered.

Road unevenness is measured by two general types of equipment: profilometers, which measure the unevenness in a straight-forward way and response-type devices, which measure the unevenness in an indirect way as the dynamic response of the measuring equipment [58].

Local as well as global unevenness can be described by a deterministic function $u_{w/r}(y)$. Traffic plateaus, poorly filled trenches and joints in a road surface are examples of local road unevenness profiles that generate vibrations in buildings during the passage of heavy traffic [59, 60, 61].

| Class | Range | | | | |
|---|---|---|---|---|---|
| Microtexture | | | $\lambda_y$ | $<$ | $5 \times 10^{-4}$ m |
| Macrotexture | $5 \times 10^{-4}$ m | $<$ | $\lambda_y$ | $<$ | $5 \times 10^{-2}$ m |
| Megatexture | $5 \times 10^{-2}$ m | $<$ | $\lambda_y$ | $<$ | 0.5 m |
| Uneveness | 0.5 m | $<$ | $\lambda_y$ | $<$ | 50 m |

Table 2.1: Classification of road roughness.

A forward Fourier transformation of the coordinate $y$ along the road to the wavenumber $k_y$ reveals the wavenumber content $\tilde{u}_{w/r}(k_y)$ of the unevenness profile $u_{w/r}(y)$. Table 2.1 shows a classification of road roughness according to the wavelength $\lambda_y = 2\pi/k_y$ of the road irregularities [62]. The range of road unevenness which is important for vehicle dynamics is characterized by wavelengths $\lambda_y$ between 0.5 m and 50 m. The largest wavelengths are only relevant at high vehicle speeds.

The global road surface unevenness is a standard example of a random process. In a classical paper by Dodds and Robson [38], it is shown how the road surface roughness is described as a two-dimensional Gaussian random process with a single power spectral density as a function of a wavenumber $k_y = 2\pi/\lambda_y$. In the case where the road shows discrete or periodic irregularities, such as joints or potholes, a description by a PSD is not suitable. The approach by Dodds and Robson was proposed for the International Standard ISO/TC108/WG9 and resulted in the ISO 8608 [39] norm that deals with the classification of road surface profiles. The classification is based on a comparison of the measured, single-sided PSD and eight categories labelled from $A$ to $H$, that are defined by a range of artifical PSD of the following form:

$$S_{w/r}(k_y) = S_{w/r}(k_{y0}) \left( \frac{k_y}{k_{y0}} \right)^{-w} \tag{2.1}$$

where $w$ equals 2 and the value of $S_{w/r}(k_{y0})$ depends on the unevenness class, as defined in table 2.2. The wavenumber content decreases with an increasing wavenumber or a smaller wavelength. It is indicated in the ISO 8608 norm that the profiles in table 2.2 can be used as the input for theoretical parametric studies. As an alternative to the single-sided PSD function in equation (2.1), a double-sided PSD function can be used. The amplitude of the latter has half the value of the amplitude for a single-sided PSD.

Compared to local road unevenness, however, the practical importance of global road unevenness is low for road traffic induced vibrations [63]. The Transport and Road Research Laboratory has investigated several sites where nuisance occurs due to road traffic induced vibrations [12, 13]. In each of these cases, the vibrations are generated by the passage of heavy traffic on a discrete irregularity of the road surface. Al-Hunaidi [41] has observed experimentally that the vibration levels due to local irregularities are ten times larger than the levels due to the global road unevenness. Several case studies by the Structural Mechanics Division [59, 60, 61] have confirmed these observations. The focus in the following will therefore be on local irregularities.

| Roughness class | $S_{w/r}(k_{y0})[\times 10^6\ \mathrm{m}^3]$ | | |
|---|---|---|---|
| | Minimum | Mean | Maximum |
| A | 0 | 1 | 2 |
| B | 2 | 4 | 8 |
| C | 8 | 16 | 32 |
| D | 32 | 64 | 128 |
| E | 128 | 256 | 512 |
| F | 512 | 1024 | 2048 |
| G | 2048 | 4096 | 8192 |
| H | 8192 | 16384 | 32768 |

Table 2.2: ISO 8608 road roughness classification ($k_{y0} = 1$ rad/m).

### 2.2.2 The vehicle dynamics

The basic mathematical models for the simulation of the vehicle ride behaviour are also used to predict the dynamic axle loads for the study of the response of roads or bridges subjected to a vehicle passage [27, 33, 34, 31, 35, 36]. These vehicle models are composed of discrete masses, springs, friction elements and dampers (figure 2.1). The vehicle body and axles are modelled as rigid inertial elements. The influence of the vibrations of continuous structural elements as the vehicle frame is small and is therefore neglected [27]. The vehicle body is connected to the axles through the suspension system, which isolates the body from the vibrations induced by the road unevenness. The vehicle body is therefore referred to as the sprung mass, whereas the vehicle's axles are the unsprung masses. A parallel connection of springs, dampers and friction elements is used to represent the suspension system, while a spring-dashpot system represents the tyres.

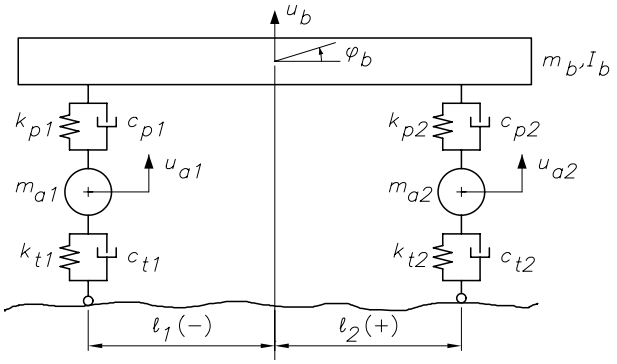


Figure 2.1: 2D 4 DOF model for a passenger car.

The vehicle models for the prediction of the vehicle comfort or safety can have a high number of degrees of freedom (DOF). Such complex models are not required for the estimation of the axle loads and the prediction of traffic induced vibrations. Complex vehicle models can be reduced to simpler ones with fewer DOF by distinguishing between master and slave DOF and applying an Irons-Guyan reduction to the system matrices [64]. In the European standard for traffic loads on bridges [36], it is indicated how these models can be further simplified as a succession of quarter car models, neglecting the coupling of the vehicle's axles through the frame.

Either 2D or 3D vehicle models can be used. 2D vehicle models only account for the motion of the vehicle in the vertical plane, while 3D vehicle models include effects as vehicle rolling. Under

normal driving conditions, when no discrete irregularities are encountered in a single wheelpath, the contribution of vehicle rolling to the axle loads is small [27].

Linear vehicle models do not account for non-linear effects such as the loss of contact between the vehicle and the road or non-linear suspension characteristics. The loss of contact occurs for empty trucks that encounter large discrete irregularities at a high vehicle speed [65]. Leaf-spring suspension systems exhibit a non-linear characteristic due to the inter-leaf friction [65, 35]. Elaborate tests are required for the characterization of the suspension system by a parallel connection of a spring, a damper and a friction element [35]. The use of these validated vehicle models, however, allows for a good prediction of the vehicle ride behaviour. Drosner [65] has compared the axle loads for a model that incorporates a friction element and a linearized vehicle model. For a relatively low friction, the inter-leaf friction contributes to the energy dissipation in the vehicle's suspension system. A large inter-leaf friction locks the suspension system and cancels the isolation of the vehicle body. This leads to a lightly damped motion, accompanied by high dynamic loads. This phenomenon only occurs in the case of roads with a smooth surface [27].

Since the size $p$ of the footprint of the tyre typically varies between 100 mm and 350 mm and is small with respect to the relevant range of wavelengths between 0.5 m and 50 m, the contact between the tyre and the road can be approximated as a point contact. For very small wavelengths, the unevenness to which the vehicle is subjected is filtered by the finite contact area [66, 67]. This phenomenon is known as the tyre enveloping effect [27, 68]. In the case of railway traffic, Knothe and Grassie [66] approximate this effect by a filter that is applied on the roughness profile of the rails and wheels to suppress the spurious components at small wavelengths or large wavenumbers.

### 2.2.3 The equations of motion of the vehicle

The equilibrium equations of motion are written in a general form that is valid for an arbitrary linear vehicle model [30]:

$$\begin{bmatrix} \mathbf{M}_{bb} & \mathbf{0} \\ \mathbf{0} & \mathbf{M}_{aa} \end{bmatrix} \begin{Bmatrix} \ddot{\mathbf{u}}_b \\ \ddot{\mathbf{u}}_a \end{Bmatrix} + \begin{bmatrix} \mathbf{C}^p_{bb} & \mathbf{C}^p_{ba} \\ \mathbf{C}^{pT}_{ba} & \mathbf{C}^p_{aa} + \mathbf{C}^t_{aa} \end{bmatrix} \begin{Bmatrix} \dot{\mathbf{u}}_b \\ \dot{\mathbf{u}}_a \end{Bmatrix} + \begin{bmatrix} \mathbf{K}^p_{bb} & \mathbf{K}^p_{ba} \\ \mathbf{K}^{pT}_{ba} & \mathbf{K}^p_{aa} + \mathbf{K}^t_{aa} \end{bmatrix} \begin{Bmatrix} \mathbf{u}_b \\ \mathbf{u}_a \end{Bmatrix}$$
$$= \begin{Bmatrix} \mathbf{F}^{\text{ext}}_b \\ \mathbf{F}^{\text{ext}}_a \end{Bmatrix} + \begin{bmatrix} \mathbf{0} & \mathbf{0} \\ \mathbf{0} & \mathbf{K}^t_{aa} \end{bmatrix} \begin{Bmatrix} \mathbf{0} \\ \mathbf{u}_r + \mathbf{u}_{w/r} \end{Bmatrix} + \begin{bmatrix} \mathbf{0} & \mathbf{0} \\ \mathbf{0} & \mathbf{C}^t_{aa} \end{bmatrix} \begin{Bmatrix} \mathbf{0} \\ \dot{\mathbf{u}}_r + \dot{\mathbf{u}}_{w/r} \end{Bmatrix} \tag{2.2}$$

where the vectors $\mathbf{u}_b$ and $\mathbf{u}_a$ collect the displacement components of the car body and the axles, respectively, while the vectors $\mathbf{F}^{\text{ext}}_b$ and $\mathbf{F}^{\text{ext}}_a$ contain external forces that are applied directly to the car body and the wheel axles. $\mathbf{M}_{aa}$ and $\mathbf{M}_{bb}$ represent the mass matrix of the vehicle body and the axles. $\mathbf{K}$ and $\mathbf{C}$ are the stiffness and damping matrix, where the superscript $p$ and $t$ refer to the contribution of the primary suspension and the tyres. $\mathbf{u}_{w/r}$ and $\mathbf{u}_r$ collect the road unevenness and the road's deformations at the contact points between the vehicle and the road.

These equations illustrate that the suspension system connects the vehicle body to the axles, while the tyres are the link between the axles and the road. The damping $\mathbf{C}^t_{aa}$ of the vehicle tyres is generally small compared to the damping of the suspension system $\mathbf{C}^p_{aa}$ [65, 35], that accounts for most of the energy dissipation.

The real eigenmodes of the vehicle are calculated through the solution of the undamped eigenvalue problem corresponding to equation (2.2):

$$\left( \begin{bmatrix} \mathbf{K}^p_{bb} & \mathbf{K}^p_{ba} \\ \mathbf{K}^{p\ T}_{ba} & \mathbf{K}^p_{aa} + \mathbf{K}^t_{aa} \end{bmatrix} - \omega^2 \begin{bmatrix} \mathbf{M}_{bb} & 0 \\ 0 & \mathbf{M}_{aa} \end{bmatrix} \right) \begin{Bmatrix} \mathbf{U}_b \\ \mathbf{U}_a \end{Bmatrix} = 0 \tag{2.3}$$

These equations are solved for a 4DOF vehicle model (figure 2.1) of a Volvo FE7 truck that has been derived from a larger 17 DOF vehicle model by means of Irons-Guyan reduction [64]. The following vehicle characteristics have been found: $m_b = 13280\,\text{kg}$, $I_b = 60397\,\text{kgm}^2$, $m_{a1} = 1250\,\text{kg}$, $m_{a2} = 650\,\text{kg}$, $l_1 = -1.775\,\text{m}$, $l_2 = +2.225\,\text{m}$, $k_{p1} = 1.26(1 + 0.80i) \times 10^6\,\text{N/m}$, $c_{p1} = 8000\,\text{Ns/m}$, $k_{p2} = 0.66(1 + 0.20i) \times 10^6\,\text{N/m}$, $c_{p2} = 0\,\text{Ns/m}$, $k_{t1} = 2.80 \times 10^6\,\text{N/m}$, $c_{t1} = 4200\,\text{Ns/m}$, $k_{t2} = 1.40 \times 10^6\,\text{N/m}$ and $c_{t2} = 2100\,\text{Ns/m}$. The real values for $k_{p1}$ and $k_{p2}$ are used for the calculation of the stiffness matrix.

| Description of mode | Eigenfrequency | Eigenmode | | | |
|---|---|---|---|---|---|
| | | $u_b$ | $\varphi_b$ | $u_{a1}$ | $u_{a2}$ |
| | [Hz] | [m] | [rad] | [m] | [m] |
| Pitch and bounce front | 1.3 | 0.0047 | 0.0034 | -0.0004 | 0.0040 |
| Pitch and bounce rear | 1.7 | 0.0072 | -0.0022 | 0.0036 | -0.0008 |
| Axle hop front axle | 9.0 | 0.0006 | 0.0003 | -0.0009 | -0.0390 |
| Axle hop rear axle | 9.1 | 0.0009 | -0.0003 | -0.0280 | -0.0012 |

Table 2.3: Eigenmodes of the 4DOF Volvo FE7 model.

For this 4-DOF vehicle model, 4 eigenmodes are found: 2 pitch and bounce modes and 2 axle hop modes (table 2.3 and figure 2.2a). The low eigenfrequencies correspond to a pitch and bounce motion of the front or the rear part of the vehicle (figure 2.2), accompanied by a smaller in-phase axle motion. These modes involve a weakly coupled motion between the front and the rear part of the vehicle. The higher eigenfrequencies correspond to the axle hop modes (figure 2.2b) and involve a motion of the rear or the front axle, accompanied by a small out-of-phase body motion.

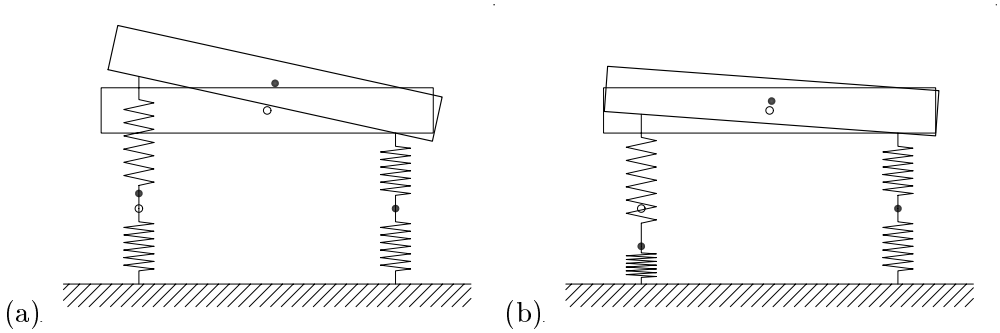


Figure 2.2: Eigenmodes of the 2D 4-DOF model for a passenger car: (a) pitch and bounce motion mode; (b) axle hop mode.

The same groups of eigenmodes are found for other 2D vehicle models. The pitch and bounce frequencies are generally situated in a frequency range between 0.8 Hz and 3 Hz, while the axle hop frequencies occur between 8 Hz and 15 Hz. The eigenfrequencies of the vehicle model can also be roughly estimated from the following equations for the pitch and bounce and the axle hop frequencies, respectively [65]:

$$\begin{aligned} f_{pb} &= \frac{1}{2\pi}\sqrt{\frac{k_{pk} + k_{tk}}{m_{bk}}} \\ f_{ah} &= \frac{1}{2\pi}\sqrt{\frac{k_{tk}}{m_{ak}}} \end{aligned} \tag{2.4}$$

where $m_{bk}$ is the part of the vehicle weight that is carried by the axle $k$. These equations indicate that the pitch and bounce frequencies are determined by the weight of the vehicle body and the stiffness of the suspension and the tyre, while the axle hop frequencies are determined primarily by the weight of the axle and the tyre stiffness.

### 2.2.4 The vehicle-road interaction problem

The general equilibrium equations (2.2) can also be written as a function of the interaction forces $\mathbf{F}^{\text{int}}_{w/r}$ between the vehicle and the road:

$$\begin{bmatrix} \mathbf{M}_{bb} & 0 \\ 0 & \mathbf{M}_{aa} \end{bmatrix} \begin{Bmatrix} \ddot{\mathbf{u}}_b \\ \ddot{\mathbf{u}}_a \end{Bmatrix} + \begin{bmatrix} \mathbf{C}^p_{bb} & \mathbf{C}^p_{ba} \\ \mathbf{C}^{p\ T}_{ba} & \mathbf{C}^p_{aa} \end{bmatrix} \begin{Bmatrix} \dot{\mathbf{u}}_b \\ \dot{\mathbf{u}}_a \end{Bmatrix} + \begin{bmatrix} \mathbf{K}^p_{bb} & \mathbf{K}^p_{ba} \\ \mathbf{K}^{p\ T}_{ba} & \mathbf{K}^p_{aa} \end{bmatrix} \begin{Bmatrix} \mathbf{u}_b \\ \mathbf{u}_a \end{Bmatrix} = \begin{Bmatrix} \mathbf{F}^{\text{ext}}_b \\ \mathbf{F}^{\text{ext}}_a \end{Bmatrix} + \begin{Bmatrix} 0 \\ -\mathbf{F}^{\text{int}}_{w/r} \end{Bmatrix} \tag{2.5}$$

The interaction forces $\mathbf{F}^{\text{int}}_{w/r}$ depend on the difference between the axle displacements $\mathbf{u}_a$ and the sum of the irregularities $\mathbf{u}_{w/r}$ of the road surface and the road displacements $\mathbf{u}_r$:

$$\mathbf{F}^{\text{int}}_{w/r} = \mathbf{K}^t_{aa} \left[\mathbf{u}_a - (\mathbf{u}_r + \mathbf{u}_{w/r})\right] + \mathbf{C}^t_{aa} \left[\dot{\mathbf{u}}_a - (\dot{\mathbf{u}}_r + \dot{\mathbf{u}}_{w/r})\right] \tag{2.6}$$

These equations illustrate that the interaction between the vehicle and the road is a coupled problem. As a result, the equations of motion of the vehicle and the road should be solved simultaneously. The motion of the contact point between the vehicle and the road presents an extra difficulty. In the literature on vehicle-bridge interaction, various solution procedures are presented [69, 70, 71].

For the study of vehicle-bridge interaction or train-track interaction, the influence of the displacements of the substructure $\mathbf{u}_r$ on the dynamic axle loads is taken into account. For the study of the vehicle-road interaction problem, the influence of the road's response on the vehicle's response is generally not taken into account due to the high stiffness of the substructure with respect to the vehicle's suspension and tyres [27, 28, 31, 32]. A preliminary study, based on the model of a beam on a Winkler foundation for the road has confirmed this assumption [30]. This allows for the use of a two-stage solution procedure, where the calculation of the vehicle's response is decoupled from the substructure's response. First, the dynamic axle loads are calculated from the equations of motion (2.2), where the influence of the road response $\mathbf{u}_r$ is neglected. Next, these axle loads are applied to the road. The transfer functions between the road and the soil are used to calculate the free field response by means of the dynamic reciprocity theorem. In the following, the equations of motion of the vehicle (2.2) are used to derive frequency response functions for the calculation of the dynamic axle loads.

### 2.2.5 The vehicle frequency response functions

The distribution of $n$ axle loads on the road is written as the summation of the product of a Dirac function that determines the position of the force and a time-dependent function $g_k(t)$:

$$\rho b_j(\mathbf{x}, t) = \sum_{k=1}^{n} \delta(x - x_S)\delta(y - y_k - vt)\delta(z) g_k(t) \delta_{3j} \tag{2.7}$$

$y_k$ is the initial position of the $k$-th axle load that moves with the vehicle speed $v$ along the $y$-axis.

The uncoupling of the equations of motion of the vehicle and the road and the use of a linear vehicle model allow to calculate the time history $g_k(t)$ of a single axle load from the contribution of all $n$ vehicle axles and the road surface profile:

$$g_k(t) = \sum_{l=1}^{n} \int_{-\infty}^{t} h_{f_k u_l}(t-\tau) u^l_{w/r}(\tau)\, d\tau \tag{2.8}$$

The contribution of axle $l$ is calculated as the convolution integral of an impulse response function $h_{f_k u_l}(t)$, representing the time-history of the $k$th axle load when a unit impulse excitation is applied to axle $l$, and the road unevenness $u^l_{w/r}(t)$ experienced by axle $l$. The latter is calculated from the road surface profile $u_{w/r}(y)$:

$$u^l_{w/r}(t) = u_{w/r}(y_l + vt) \tag{2.9}$$

The representation of the interaction force $\hat{g}_k(\omega)$ in the frequency domain results from the Fourier transform of equation (2.8):

$$\hat{g}_k(\omega) = \sum_{l=1}^{n} \hat{h}_{f_k u_l}(\omega) \hat{u}^l_{w/r}(\omega) \tag{2.10}$$

$\hat{h}_{f_k u_l}(\omega)$ is the frequency response function (FRF) of the axle $k$ due to an imposed displacement at axle $l$ [27, 37, 33]. The FRF's are obtained by solving the equations of motion of the vehicle (2.2) in the frequency domain, where the external forces are set to zero and $\hat{\mathbf{u}}_{w/r}(\omega)$ represents a vector with a unit harmonic displacement applied to axle $l$. The FRF's are calculated by means of equation (2.6) in the frequency domain, where the road's deformations $\mathbf{u}_r$ are neglected:

$$\hat{h}_{f_k u_l}(\omega) = (k_{tk} + i\omega c_{tk})(\hat{u}_{ak}(\omega) - \delta_{kl}) \tag{2.11}$$

with $\delta_{kl}$ the Kronecker delta. The frequency content $\hat{u}^l_{w/r}(\omega)$ in equation (2.10) follows from the forward Fourier transform $\hat{u}_{w/r}(\omega)$ of the road unevenness experienced by an axle at a zero initial position:

$$\hat{u}^l_{w/r}(\omega) \;=\; \hat{u}_{w/r}(\omega)\, \exp\left(i\omega \frac{y_l}{v}\right) \tag{2.12}$$

$\hat{u}_{w/r}(\omega)$ can also be calculated from the wavenumber domain representation $\tilde{u}_{w/r}(k_y)$ of $u_{w/r}(y)$:

$$\hat{u}_{w/r}(\omega) \;=\; \frac{1}{v} \tilde{u}_{w/r}\left(-\frac{\omega}{v}\right) \tag{2.13}$$

This expression shows how the vehicle speed $v$ couples the wavenumber content $\tilde{u}_{w/r}(k_y)$ of the unevenness profile to the frequency content $\hat{u}_{w/r}(\omega)$ of the signal that is applied to each axle of the vehicle. An unevenness component with a wavelength $\lambda_y$ corresponds to a harmonic excitation of the vehicle at a frequency $v/\lambda_y$. For regular vehicle speeds between 8 m/s and 20 m/s, the range of wavenumbers that corresponds to an excitation in the range of axle hop frequencies between 8 Hz and 15 Hz is roughly situated between 2.5 rad/m and 12 rad/m. This corresponds to the range of wavelengths between 0.5 m and 2.5 m.

Equation (2.13) illustrates that the quasi-static value of the frequency content of the signal that is applied to the vehicle decreases as the vehicle speed increases, while the frequency content shifts to higher frequencies.

Using equations (2.10) and (2.12), the contribution of all axles to a single axle load is collected in a single FRF $\hat{h}_{f_k u}(\omega)$:

$$\hat{g}_k(\omega) \;=\; \hat{u}_{w/r}(\omega) \sum_{l=1}^{n} \hat{h}_{f_k u_l}(\omega)\, \exp\left(i\omega \frac{y_l}{v}\right) \;=\; \hat{u}_{w/r}(\omega) \hat{h}_{f_k u}(\omega) \tag{2.14}$$

$\hat{h}_{f_k u}(\omega)$ represents the axle load at an axle $k$ for a harmonic excitation of the entire vehicle by an unevenness profile with a wavelength $\lambda_y = v/f$. The vehicle FRF $\hat{h}_{f_k u}(\omega)$ account for the time delay between the input at the vehicle's axles and depend on the vehicle speed $v$.

## 2.3 The road-soil interaction problem

### 2.3.1 Introduction

In the past, the presence of the road has often been disregarded for the calculation of the free field road traffic induced vibrations. In this case, the dynamic axle loads are directly applied to the soil. This assumption is only valid if the wavelength in the soil is large with respect to the area of the road-soil interface that accounts for the transmission of the forces to the soil. The distribution of the contact forces is determined by the dynamic interaction between the road and the soil.

In the following, it is shown how a substructure approach is applied to study the interaction between the road and the soil. First, the equations of motion of the road are considered. These equations account for bending as well as torsional deformations of the road. A transformation of the horizontal coordinate $y$ along the road to a horizontal wavenumber $k_y$ allows for an efficient solution procedure in the frequency-wavenumber domain. The computation of the soil's impedance for the bending and torsional modes requires the calculation of the modal soil tractions. The latter are calculated with a boundary element method, that is based on the formulation of the integral equations.

### 2.3.2 The equations of motion of the road

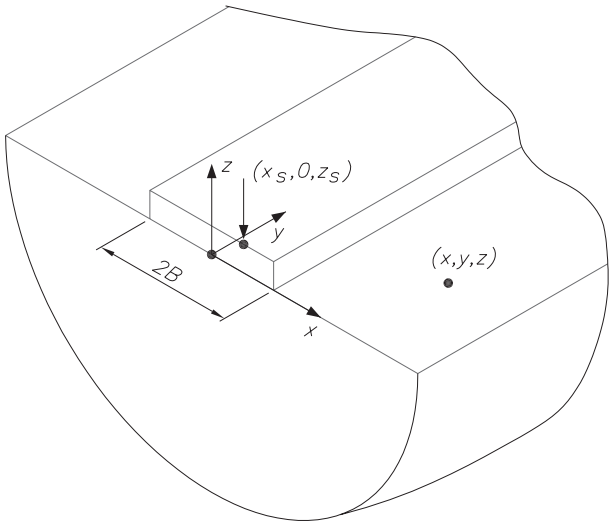


Figure 2.3: The road-soil interaction problem.

The road is assumed to be located at the soil's surface and to be invariant with respect to the longitudinal direction $y$ (figure 2.3). The width of the road is equal to 2B. Furthermore, it is assumed that the road's cross section is rigid. The vertical road displacements $u_{rz}(x, y, t)$ are therefore independent of the vertical coordinate $z$ and can be written as a function of the vertical translation $u_{cz}(y, t)$ of the cross section's centre of gravity and the rotation $\beta_{cy}(y, t)$ about this centre:

$$u_{rz}(x, y, t) \;=\; u_{cz}(y, t) + x\beta_{cy}(y, t) \;=\; \boldsymbol{\phi}_r(x)\boldsymbol{\alpha}_r(y, t) \tag{2.15}$$

The displacement modes of the rigid cross section are collected in a vector $\boldsymbol{\phi}_r = \{1,\, x\}^T$, while the vector $\boldsymbol{\alpha}_r$ collects the displacement $u_{cz}$ and the rotation $\beta_{cy}$. The latter can be interpreted as unknown modal coordinates of the deformation modes of the rigid cross section.

For the calculation of the road-soil transfer function, the case is considered where a concentrated pulse $\delta(x - x_S)\delta(y)\delta(z - z_S)\delta(t)$ is applied at a point $\{x_S, 0, z_S\}^T$ of the road's surface. The kinematical assumptions result in the following equilibrium equations for the road, which govern the longitudinal bending and torsional deformations, respectively:

$$+EI_x\frac{\partial^4 u_{cz}}{\partial y^4} + \rho A\frac{\partial^2 u_{cz}}{\partial t^2} \;=\; \delta(y)\delta(t) + f^e_{cz} \tag{2.16}$$

$$-GC\frac{\partial^2 \beta_{cy}}{\partial y^2} + \rho I_p\frac{\partial^2 \beta_{cy}}{\partial t^2} \;=\; x_S\delta(y)\delta(t) + m^e_{cy} \tag{2.17}$$

In these equations, $A$ is the road's cross section, $I_x$ the moment of inertia with respect to $x$, $C$ the torsional moment of inertia and $I_p$ the polar moment of inertia; $E$ is the Young's modulus, $G$ the shear modulus and $\rho$ the density of the road. The first terms at the right hand side of equations (2.16) and (2.17) represent the contribution from the concentrated pulse. The vertical force per unit length $f^e_{cz}$ and the torsional moment per unit length $m^e_{cy}$ are exerted by the soil on the road along the interface $\Sigma_{rs}$. These terms follow from the equilibrium at the interface $\Sigma_{rs}$ between the road and the soil:

$$\begin{aligned} f^e_{cz} &= -\int_{-B}^{+B} t_{sz}(\mathbf{u}_s)(x, y, z = 0, t)\, dx \\ m^e_{cy} &= -\int_{-B}^{+B} x t_{sz}(\mathbf{u}_s)(x, y, z = 0, t)\, dx \end{aligned} \tag{2.18}$$

where $t_{sz}(\mathbf{u}_s)(x, y, z, t)$ represents the vertical component of the soil tractions $\mathbf{t}_s = \boldsymbol{\sigma}_s\mathbf{n}$ on a boundary with a unit outward normal $\mathbf{n}$ for a displacement field $\mathbf{u}_s$.

In equations (2.16) and (2.17), the road's bending and torsional stiffness and inertia are represented by a single term. For a uniform rectangular cross section with a width $b$ and a height $h$, $EI_x = Ebh^3/12$ and $\rho A = \rho bh$. If the height $h$ is relatively small with respect to the width $b$, the torsional stiffness $GC$ can be approximated as $Gbh^3/3$. The torsional inertia $\rho I_p = \rho(bh^3/12 + b^3h/12)$. In practice, however, the road section is a horizontally layered structure, where a top asphalt or concrete layer is supported by a foundation. In this case, the material properties $E_i$, $\rho_i$ and the height $h_i$ of each layer are used to calculate equivalent bending and torsional properties for the layered road structure.

A double forward Fourier transformation is performed to transform the time $t$ to the circular frequency $\omega$ and the longitudinal coordinate $y$ to the horizontal wavenumber $k_y$. The latter is allowed as the road and the soil are invariant in the $y$-direction. The displacement decomposition (2.15) for the vertical road displacements becomes:

$$\tilde{u}_{rz}(x, k_y, \omega) \;=\; \tilde{u}_{cz}(k_y, \omega) + x\tilde{\beta}_{cy}(k_y, \omega) \;=\; \boldsymbol{\phi}_r(x)\tilde{\boldsymbol{\alpha}}_r(k_y, \omega) \tag{2.19}$$

The road's deformations $\boldsymbol{\phi}_r(x)\tilde{\boldsymbol{\alpha}}_r(k_y,\omega)$ correspond to a bending or a torsional wave with a phase velocity $C_y = \omega/k_y$. The equilibrium equations (2.16) and (2.17) are formulated in the frequency-wavenumber domain:

$$\left(\begin{bmatrix} EI_x k_y^4 & 0 \\ 0 & GCk_y^2 \end{bmatrix} - \omega^2 \begin{bmatrix} \rho A & 0 \\ 0 & \rho I_p \end{bmatrix}\right) \begin{Bmatrix} \tilde{u}_{cz} \\ \tilde{\beta}_{cy} \end{Bmatrix} = \begin{Bmatrix} 1 \\ x_S \end{Bmatrix} + \begin{Bmatrix} \tilde{f}^e_{cz} \\ \tilde{m}^e_{cy} \end{Bmatrix} \tag{2.20}$$

These equations can alternatively be written in matrix-vector notation:

$$\left(\tilde{\mathbf{K}}_r - \omega^2 \tilde{\mathbf{M}}_r\right) \tilde{\boldsymbol{\alpha}}_r = \tilde{\mathbf{f}}^\delta_c + \tilde{\mathbf{f}}^e_c \tag{2.21}$$

with $\tilde{\mathbf{K}}_r$ the stiffness matrix and $\tilde{\mathbf{M}}_r$ the mass matrix of the road. The road's impedance $\tilde{\mathbf{K}}_r - \omega^2\mathbf{M}_r$ is singular for free bending waves with a wave velocity $C_b = \sqrt[4]{EI_x\omega^2/\rho A}$ and free torsional waves with a wave velocity $C_t = \sqrt{GC/\rho I_p}$. It is assumed that no damping is present in the road and as a result, the road's impedance is real. $\tilde{\mathbf{f}}^\delta_c$ is the force vector related to the Dirac load. The vector $\tilde{\mathbf{f}}^e_c$ follows from equation (2.18), that expresses the equilibrium at the road-soil interface $\Sigma_{rs}$:

$$\tilde{\mathbf{f}}^e_c = -\int_{-B}^{+B} \boldsymbol{\phi}_r(x)\tilde{t}_{sz}(\tilde{\mathbf{u}}_s)(x,k_y,z=0,\omega)\,dx \tag{2.22}$$

$\tilde{t}_{sz}(\tilde{\mathbf{u}}_s)$ is the representation of $t_{sz}(\mathbf{u}_s)$ in the frequency-wavenumber domain. The displacements $\tilde{\mathbf{u}}_s$ in the horizontally layered soil are decomposed on the basis of the scattered elastodynamic wave fields, radiated by the bending and torsional modes of the road:

$$\tilde{\mathbf{u}}_s(x,k_y,z,\omega) = \tilde{\boldsymbol{\phi}}_s(x,k_y,z,\omega)\tilde{\boldsymbol{\alpha}}_s(k_y,\omega) \tag{2.23}$$

The vector $\tilde{\boldsymbol{\phi}}_s(x,k_y,z,\omega)$ collects the scattered wave fields in the soil, while the vector $\tilde{\boldsymbol{\alpha}}_s(k_{y,\omega})$ collects the modal coordinates. The following displacement continuity conditions are imposed on the interface $\Sigma_{rs}$:

$$\tilde{\mathbf{u}}_r(x,k_y,\omega) = \tilde{\mathbf{u}}_s(x,k_y,z=0,\omega) \tag{2.24}$$

The vertical pulse on the road generates horizontal and vertical tractions at the road-soil interface. However, only the vertical tractions have a non-zero resultant. When the loaded area is small compared to the wavelength in the soil, the horizontal tractions have a small influence on the free field displacements. Under these conditions, a frictionless contact between the road and the soil can be assumed and no restrictions are imposed on the displacements in the $x$- and $y$-direction. This approach corresponds to the application of relaxed boundary conditions, whereas the continuity conditions in equation (2.24) are referred to as welded boundary conditions.

The following continuity condition prevails for the vertical displacement component:

$$\tilde{u}_{rz}(x,k_y,\omega) = \tilde{u}_{sz}(x,k_y,z=0,\omega) \tag{2.25}$$

Equation (2.25) can be further elaborated if the displacement decompositions (2.19) and (2.23) are introduced:

$$\boldsymbol{\phi}_r(x)\tilde{\boldsymbol{\alpha}}_r(k_y,\omega) = \tilde{\boldsymbol{\phi}}_{sz}(x,k_y,z=0,\omega)\tilde{\boldsymbol{\alpha}}_s(k_y,\omega) \tag{2.26}$$

At the road-soil interface $\Sigma_{rs}$, the vertical components of the scattered wave fields $\tilde{\boldsymbol{\phi}}_{sz}(x, k_y, z = 0, \omega)$ are equal to the displacement modes $\boldsymbol{\phi}_r(x)$ of the road for each frequency $\omega$ and wavenumber $k_y$, so that:

$$\tilde{\boldsymbol{\alpha}}_r(k_y, \omega) \;=\; \tilde{\boldsymbol{\alpha}}_s(k_y, \omega) \tag{2.27}$$

As a result, the subscript $r$ or $s$ in the modal coordinates $\tilde{\boldsymbol{\alpha}}$ can be omitted. Using the displacement decomposition in equation (2.23) together with the result of equation (2.27), the force vector in equation (2.22) can be elaborated as:

$$\tilde{\mathbf{f}}_c^e \;=\; -\int_{-B}^{+B} \boldsymbol{\phi}_r(x) \tilde{t}_{sz}(\tilde{\boldsymbol{\phi}}_s)(x, k_y, z = 0, \omega) \tilde{\boldsymbol{\alpha}}(k_y, \omega)\, dx \tag{2.28}$$

The equilibrium equation (2.21) becomes:

$$\left[\tilde{\mathbf{K}}_r - \omega^2 \tilde{\mathbf{M}}_r + \tilde{\mathbf{K}}_s\right] \tilde{\boldsymbol{\alpha}} \;=\; \tilde{\mathbf{f}}_c^{\delta} \tag{2.29}$$

where $\tilde{\mathbf{K}}_s$ represents the soil's impedance:

$$\tilde{\mathbf{K}}_s \;=\; \int_{-B}^{+B} \boldsymbol{\phi}_r(x) \tilde{t}_{sz}(\boldsymbol{\phi}_s)(x, k_y, z = 0, \omega)\, dx \tag{2.30}$$

This equation shows that the calculation of the soil's impedance $\tilde{\mathbf{K}}_s$ requires the computation of the soil tractions $\tilde{t}_{sz}(\boldsymbol{\phi}_s)(x, k_y, z = 0, \omega)$ for the road's bending and torsional modes $\boldsymbol{\phi}_r(x)$. The off-diagonal elements of $\tilde{\mathbf{K}}_s$ represent the coupling that occurs between the bending and torsional modes. $\tilde{\mathbf{K}}_s(1, 2)$ is the vertical force that follows from the tractions due to a unit rotation of the interface, while $\tilde{\mathbf{K}}_s(2, 1)$ represents the torsional moment that results from the tractions due to a uniform vertical displacement. As both elements are zero, the soil's impedance $\tilde{\mathbf{K}}_s$ is a diagonal matrix and the deformation modes are uncoupled. The imaginary part of the impedance corresponds to the loss of energy that takes place through material and radiation damping in the soil [72, 73, 74].

The solution of the system of equations (2.29) gives the complex modal coordinates $\tilde{\boldsymbol{\alpha}}(k_y, \omega)$. The soil tractions $\tilde{t}_{sz}(\tilde{\mathbf{u}}_s)(x, k_y, z = 0, \omega)$ at the road-soil interface are calculated from the modal coordinates:

$$\tilde{t}_{sz}(x, k_y, z = 0, \omega) \;=\; \tilde{t}_{sz}(\tilde{\boldsymbol{\phi}}_s)(x, k_y, z = 0, \omega) \tilde{\boldsymbol{\alpha}}(k_y, \omega) \tag{2.31}$$

These soil tractions are used to calculate the free field displacements for a concentrated unit pulse on the road, representing to the transfer function between the road and a point in the free field. The unknown soil tractions $\tilde{t}_{sz}(\boldsymbol{\phi}_s)(x, k_y, z = 0, \omega)$ for the road's deformation modes $\boldsymbol{\phi}_r(x)$ are calculated by means of a boundary element method [64], that is based on a discretization of the road-soil interface and an interpolation of the field variables by means of global shape functions.

### 2.3.3 The road-soil transfer function

The road-soil transfer function represents the soil displacements due to a concentrated unit pulse applied at the road. In this subsection, the free field soil displacements are calculated from the vertical soil tractions at the road-soil interface.

Accounting for the invariance of the soil in the horizontal direction and the invariance of the road in its longitudinal direction, it can be shown, by means of the Betti-Rayleigh reciprocal theorem, that

the following expression holds in the frequency-wavenumber domain:

$$\tilde{h}_{zi}(\xi_1, k_y, \xi_3, \omega) = \int_{-B}^{+B} \tilde{t}_{sj}(x, k_y, 0, \omega)\tilde{u}^G_{ji}(\xi_1 - x, k_y, \xi_3, \omega)\, dx \tag{2.32}$$

In this equation, $\tilde{u}^G_{ji}(\mathbf{x}, \omega)$ is the Green's function of a linear elastic layered halfspace that represents the free field displacements in a point $\mathbf{x}$ in a direction $\mathbf{e}_i$ due to a unit pulse in a direction $\mathbf{e}_j$ in the origin. The Green's functions are elements of a 3 by 3 tensor. The evaluation of equation (2.32) requires the computation of the full 3 by 3 Green's displacement tensor. If a relaxed contact is assumed in the horizontal direction, the horizontal soil tractions are zero and:

$$\tilde{h}_{zi}(\xi_1, k_y, \xi_3, \omega) = \int_{-B}^{+B} \tilde{t}_{sz}(x, k_y, 0, \omega)\tilde{u}^G_{zi}(\xi_1 - x, k_y, \xi_3, \omega)\, dx \tag{2.33}$$

In this case, the calculation of the transfer function from the tractions at the interface only requires the computation of the third row $\tilde{u}^G_{zi}(x, k_y, z, \omega)$ of the Green's tensor.

## 2.4 The response to moving loads

In the following, the dynamic Betti-Rayleigh reciprocal theorem [75] is used for the calculation of the response for a deterministic moving load. The use of this theorem allows to compute the free field response from the transfer function between the road and a point in the free field and the time history of the dynamic axle loads.

Based on the invariance of the road-soil system in the longitudinal $y$-direction, the following expression is derived for the displacement $u_{si}(\xi_1, \xi_2, \xi_3, t)$ at a point $\{\xi_1, \xi_2, \xi_3\}^T$ in a direction $\mathbf{e}_i$ by means of the Betti-Rayleigh reciprocal theorem:

$$u_{si}(\xi_1, \xi_2, \xi_3, t) = \int_{-\infty}^{t} g_k(\tau) h_{zi}(\xi_1, \xi_2 - y_k - v\tau, \xi_3, t - \tau)\, d\tau \tag{2.34}$$

The response is calculated as a convolution integral where the integrand represents the contribution of the elementary impulse $g_k(\tau)d\tau$ at a time $\tau$. The contribution is calculated as the product of the elementary impulse and the transfer function $h_{zi}(\xi_1, \xi_2 - y_k - v\tau, \xi_3, t - \tau)$, evaluated at the position of a receiver that moves in the opposite direction of the load.

The transfer function for a concentrated pulse that is applied at a time $t = 0$ is zero for $t - \tau < 0$. As a result, the upper limit of the integral in equation (2.34) can be extended from $t$ to $+\infty$. The frequency content of the response is calculated as the forward Fourier transform from the time $t$ to the circular frequency $\omega$:

$$\hat{u}_{si}(\xi_1, \xi_2, \xi_3, \omega) = \int_{-\infty}^{+\infty} \int_{-\infty}^{+\infty} g_k(\tau) h_{zi}(\xi_1, \xi_2 - y_k - v\tau, \xi_3, t - \tau)\, d\tau \exp(-i\omega t)\, dt \tag{2.35}$$

In the right hand side of this equation, the exponential term $\exp(-i\omega t)$ is replaced by the equivalent term $\exp[-i\omega(t - \tau)] \exp(-i\omega\tau)$, while the order of integration is changed:

$$\hat{u}_{si}(\xi_1, \xi_2, \xi_3, \omega) = \int_{-\infty}^{+\infty} g_k(\tau) \left[ \int_{-\infty}^{+\infty} h_{zi}(\xi_1, \xi_2 - y_k - v\tau, \xi_3, t - \tau) \exp[-i\omega(t - \tau)]\, dt \right] \exp(-i\omega\tau)\, d\tau \tag{2.36}$$

The bracketed term represents the Fourier transform of the transfer function, so that:

$$\hat{u}_{si}(\xi_1,\xi_2,\xi_3,\omega) = \int_{-\infty}^{+\infty} g_k(\tau)\hat{h}_{zi}(\xi_1,\xi_2-y_k-v\tau,\xi_3,\omega)\exp(-i\omega\tau)\,d\tau \tag{2.37}$$

The response in the wavenumber-frequency domain is obtained as the forward Fourier transform of the horizontal coordinate $\xi_2$ to the wavenumber $k_y$:

$$\tilde{u}_{si}(\xi_1,k_y,\xi_3,\omega) = \int_{-\infty}^{+\infty}\int_{-\infty}^{+\infty} g_k(\tau)\hat{h}_{zi}(\xi_1,\xi_2-y_k-v\tau,\xi_3,\omega)\exp(-i\omega\tau)\,d\tau\exp(+ik_y\xi_2)\,d\xi_2 \tag{2.38}$$

After a change of the order of integration and a change of variables according to $\xi_2=\zeta+y_k+v\tau$, the following expression is found:

$$\tilde{u}_{si}(\xi_1,k_y,\xi_3,\omega) = \int_{-\infty}^{+\infty} g_k(\tau)\left[\int_{-\infty}^{+\infty}\hat{h}_{zi}(\xi_1,\zeta,\xi_3,\omega)\exp(+ik_y\zeta)\,d\zeta\right]\exp[+ik_y(y_k+v\tau)]\exp(-i\omega\tau)\,d\tau \tag{2.39}$$

The bracketed term is the wavenumber domain representation of the transfer function:

$$\tilde{u}_{si}(\xi_1,k_y,\xi_3,\omega) = \int_{-\infty}^{+\infty} g_k(\tau)\tilde{h}_{zi}(\xi_1,k_y,\xi_3,\omega)\exp[+ik_y(y_k+v\tau)]\exp(-i\omega\tau)\,d\tau \tag{2.40}$$

The exponential functions that depend on the variable $\tau$ are collected as follows:

$$\tilde{u}_{si}(\xi_1,k_y,\xi_3,\omega) = \left[\int_{-\infty}^{+\infty} g_k(\tau)\exp[-i(\omega-k_yv)\tau)]\,d\tau\right]\tilde{h}_{zi}(\xi_1,k_y,\xi_3,\omega)\exp(+ik_yy_k) \tag{2.41}$$

The bracketed term represents the frequency-shifted Fourier transform of the time-dependent amplitude of the moving load:

$$\tilde{u}_{si}(\xi_1,k_y,\xi_3,\omega) = \hat{g}_k(\omega-k_yv)\tilde{h}_{zi}(\xi_1,k_y,\xi_3,\omega)\exp(+ik_yy_k) \tag{2.42}$$

This equation shows that the response in the frequency-wavenumber domain is the product of the transfer function and the frequency content of the source, provided that the latter is shifted by $k_yv$. For a limiting small velocity $v$, the shift $k_yv$ tends to zero and the solution for the case of a load at a fixed position is recovered.

The representation $\hat{u}_{si}(\xi_1,\xi_2,\xi_3,\omega)$ of the response in the frequency domain is found from the inverse wavenumber domain transform:

$$\hat{u}_{si}(\xi_1,\xi_2,\xi_3,\omega) = \frac{1}{2\pi}\int_{-\infty}^{+\infty}\hat{g}_k(\omega-k_yv)\tilde{h}_{zi}(\xi_1,k_y,\xi_3,\omega)\exp[-ik_y(\xi_2-y_k]\,dk_y \tag{2.43}$$

The frequency content $\hat{g}_k(\omega-k_yv)$ can alternatively be written as $\hat{g}_k[\omega(1-v/C_y)]$, where $C_y$ is the phase velocity in the $y$-direction. The frequency content of the response at a circular frequency $\omega$ is emitted by the source at a frequency $\tilde{\omega}=\omega(1-v/C_y)$. For a positive phase velocity $C_y$, an increasing speed $v$ reduces the emitting $\tilde{\omega}$. For a negative phase velocity $C_y$, the emitting circular frequency

$\tilde{\omega}$ increases with the source speed. It is more convenient, however, to apply a change of variables according to $k_y = (\omega - \tilde{\omega})/v$. This change of variables moves the frequency shift from the frequency content of the moving loads, to the wavenumber content of the transfer function:

$$\hat{u}_{si}(\xi_1, \xi_2, \xi_3, \omega) = \frac{1}{2\pi v} \int_{-\infty}^{+\infty} \hat{g}_k(\tilde{\omega}) \tilde{h}_{zi}(\xi_1, \frac{\omega - \tilde{\omega}}{v}, \xi_3, \omega) \exp\left[-i\left(\frac{\omega - \tilde{\omega}}{v}\right)(\xi_2 - y_k)\right] d\tilde{\omega} \tag{2.44}$$

The frequency content $\hat{g}_k(\tilde{\omega})$ of the source and the displacement $\hat{u}_{si}(\xi_1, \xi_2, \xi_3, \omega)$ at the receiver are coupled through the wavenumber at which the transfer function is evaluated. For a limiting large velocity $v$, the wavenumber $(\omega - \tilde{\omega})/v$ tends to zero and the solution for the 2D case of a line load along the path of the moving source is obtained.

If the distance between the source and the receiver in the $y$-direction is much larger than the distance in the $x$-direction, the response is dominated by waves in the positive $y$-direction. In this case, the phase velocity $C_y$ is close to the dominant wave velocity $C$ in the soil. A circular frequency $\tilde{\omega}$ emitted at the source results in a higher frequency $\omega = \tilde{\omega}/(1 - v/C)$ at the receiver. When the source approaches the receiver, the waves propagate in the $x$-direction as well and the phase velocity $C_y$ tends to infinity. Under these conditions, $\omega$ tends to $\tilde{\omega}$. When the source has passed the receiver, the phase velocity $C_y$ tends to $-C$ and the frequency $\tilde{\omega}$ emitted by the source results in a lower frequency $\omega = \tilde{\omega}/(1 + v/C)$ at the receiver. This phenomenon is known as the Doppler effect.

The response in the time domain is finally obtained as the inverse Fourier transform of the previous expression:

$$u_{si}(\xi_1, \xi_2, \xi_3, t) = \frac{1}{2\pi} \int_{-\infty}^{+\infty} \hat{u}_{si}(\xi_1, \xi_2, \xi_3, \omega) \exp(+i\omega t)\, d\omega \tag{2.45}$$

In the case where the global road unevenness is described by a power spectral density as a function of the wavenumber $k_y$ as in the ISO8608 standard [38, 39], the vehicle transfer functions can be used to calculate the PSD of the axle loads [64]. In this case, the deterministic solution procedure is not applicable and a stochastic solution procedure is required to calculate the statistical properties of the response. Due to the motion of the random load, however, the response is non-stationary and the statistical properties of the response are time-dependent. The calculation therefore requires the use of non-stationary solution methods. A neglection of the motion of the random loads enables the use of simple stationary methods, as they are frequently used for the calculation of the PSD of the free field vibrations [40, 56]. Within the frame of the DWTC project, however, a stochastic method has been developed to calculate the response for a set of moving random loads [76, 64]. The Wigner-Ville method [77, 78, 79, 80] is applied to calculate the time-dependent statistical properties of the response at each time $t$ during the passage of the random source.

# Chapter 3

# Parametric study

## 3.1 Introduction

In the previous chapter, a numerical prediction model for road traffic induced vibrations has been presented. The free field vibrations are calculated in two stages. First, the dynamic axle loads are calculated from the longitudinal road unevenness and the vehicle frequency response functions. Next, the dynamic Betti-Rayleigh reciprocal theorem is used to compute the free field vibrations from the axle loads and the transfer functions between the road and a point in the free field.

Within the frame of the present project, a preliminary parametric study has been performed by Dom [81]. In this chapter, the results of a more elaborate parametric study are discussed. First, the wavenumber content of the longitudinal profile of various traffic bumps and a joint in a road surface is discussed. Next, the influence of the vehicle characteristics on the vehicle frequency response functions is studied for a Volvo FE7 truck. The dynamic axle loads are calculated for the passage of the truck on a plateau with sine-shaped ramps and a joint in a road surface, respectively. In both cases, the free field response is computed for a road supported by a homogeneous halfspace. Furthermore, the influence of the thickness of the road section and the soil's material damping on the free field vibrations is discussed. Finally, the results of an elaborate study of the influence of the soil's stratification on the free field vibratons are recapitulated. The influence of the vehicle speed is extensively demonstrated in the next chapter, where the experimental validation of the numerical model is discussed.

## 3.2 The longitudinal road unevenness

In Belgium, profiles for traffic bumps and plateaus are prescribed in the Royal Decree of 9 October 1998 [82], which is in force since 28 October 1998.

For a sine-shaped traffic bump with a height $H$ and a length $L$, the longitudinal road unevenness profile $u_{w/r}(y)$ is:

$$u_{w/r}(y) = \frac{H}{2}\left[1 + \cos\left(\frac{2\pi y}{L}\right)\right] \qquad -\frac{L}{2} < y < \frac{L}{2} \tag{3.1}$$

The Royal Decree prescribes a height $H = 0.12$ m and a length $L = 4.80$ m. Figure 3.1a shows the longitudinal unevenness profile.

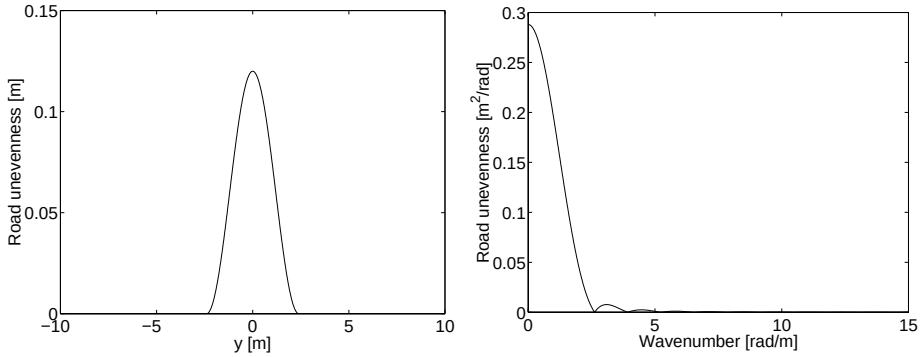


a. $u_{w/r}(y)$ b. $\tilde{u}_{w/r}(k_y)$

Figure 3.1: The longitudinal road profile of a sine-shaped traffic bump (a) as a function of the coordinate $y$ along the road and (b) in the wavenumber domain.

The wavenumber content of the profile is calculated analytically as:

$$\tilde{u}_{w/r}(k_y) = \frac{HL}{2}\text{sinc}\left(\frac{k_y L}{2}\right)\left[\frac{1}{1-\left(\frac{k_y L}{2\pi}\right)^2}\right] \tag{3.2}$$

The quasi-static value at $k_y = 0$ is equal to $HL/2$ or the area under the surface of the profile (figure 3.1b). As the profile $u_{w/r}(y)$ is real and symmetric with respect to $y = 0$, the wavenumber content is real and symmetric with respect to $k_y = 0$ as well. The wavenumber content $\tilde{u}_{w/r}(k_y)$ is inversely proportional to $k_y^3$ for a limiting large wavenumber $k_y$, or a limiting small wavelength $\lambda_y$. The presence of the sinc function results in lobes with zeros at wavenumbers $k_{yn}^0 = 2\pi n/L$. The first zero at $k_{y1}^0 = 2\pi/L$ cancels the pole of the bracketed term and is not visible. The wavenumber content is mainly situated in the range below 2.5 rad/m that, at mean vehicle speeds, does not contribute to the frequency content of the signal experienced by the axles in the range of the axle hop frequencies.

At a crossing for pedestrians, a traffic plateau with two ramps and a flat mid section can be installed. Depending on the shape of the ramp, a distinction is made between two types of plateaus. The first type has a trapezoidal form and is described by the following function:

$$u_{w/r}(y) = \begin{cases} H & |y| < \frac{L}{2} \\ H\left[1 - \frac{|y|-L/2}{l}\right] & \frac{L}{2} < |y| < \frac{L}{2} + l \\ 0 & |y| > \frac{L}{2} + l \end{cases} \tag{3.3}$$

where $L$ is the length of the flat mid section, $l$ is the length of both ramps and $H$ is the height. The Royal Decree prescribes a length $L$ that is larger than 5 m, a length $l$ of the ramps that varies between 0.7 m and 5.0 m and a height $H$ that ranges from 0.10 m to 0.15 m. The recommended values depend on the type of traffic. Figure 3.2a shows the longitudinal unevenness profile of a plateau with a height $H = 0.12$ m, a length $L = 10$ m and ramps with a length $l = 1.20$ m.

The wavenumber content of the profile equals:

$$\tilde{u}_{w/r}(k_y) = H(L+l)\text{sinc}\left[\frac{k_y(L+l)}{2}\right]\text{sinc}\left(\frac{k_y l}{2}\right) \tag{3.4}$$

The quasi-static value at $k_y = 0$ is equal to $H(L+l)$ (figure 3.2b). The wavenumber content $\tilde{u}_{w/r}(k_y)$ shows small lobes that are related to the mean length $L+l$ of the profile with zeros at $k_{yn}^0 = 2\pi n/(L+l)$.

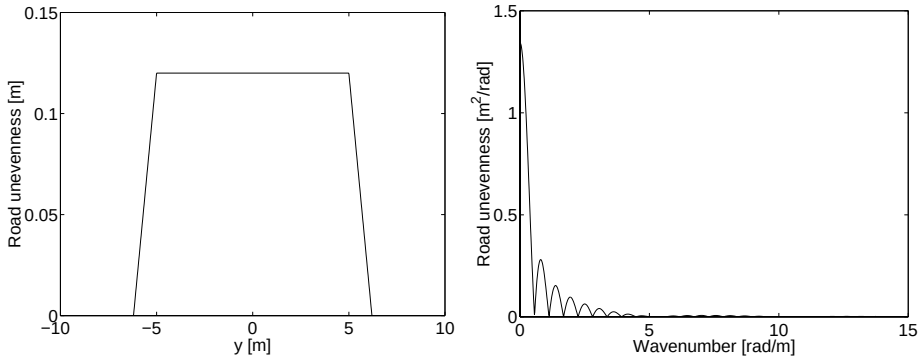


a. $u_{w/r}(y)$ b. $\tilde{u}_{w/r}(k_y)$

Figure 3.2: The longitudinal road profile of a traffic plateau with a trapezoidal form (a) as a function of the coordinate $y$ along the road and (b) in the wavenumber domain.

The large lobes that depend on the length $l$ of the ramps with zeros at $k_{yn}^0 = 2\pi n/l$ are not visible on figure 3.2b. For a limiting large wavenumber $k_y$, $\tilde{u}_{w/r}(k_y)$ tends to zero inversely proportional to $k_y^2$. Compared to the wavenumber content of the sine-shaped bump (figure 3.1b), the contribution at wavenumbers $k_y$ larger than 2.5 rad/m is much larger due to the steeper slopes of the ramps of the plateau.

For a traffic plateau with sine-shaped ramps, the road surface profile $u_{w/r}(y)$ is represented by the following function:

$$u_{w/r}(y) = \begin{cases} H & |y| < \frac{L}{2} \\ \frac{H}{2}\left[1 - \cos\left(\frac{2\pi(|y|-L/2+l)}{2l}\right)\right] & \frac{L}{2} < |y| < \frac{L}{2} + l \\ 0 & |y| > \frac{L}{2} + l \end{cases} \tag{3.5}$$

The length $L$ of the flat mid section is larger than 5 m, while the length $l$ of the ramps varies between 0.85 m and 3.8 m and the height $H$ ranges from 0.10 m to 0.15 m. Compared to the trapezoidal plateau, the recommended length $l$ of the ramps is smaller for a plateau with sine-shaped ramps. Figure 3.3a shows the longitudinal unevenness profile of a sine-shaped plateau with a height $H = 0.12$ m, a length $L = 10$ m and ramps with a length $l = 1.20$ m.

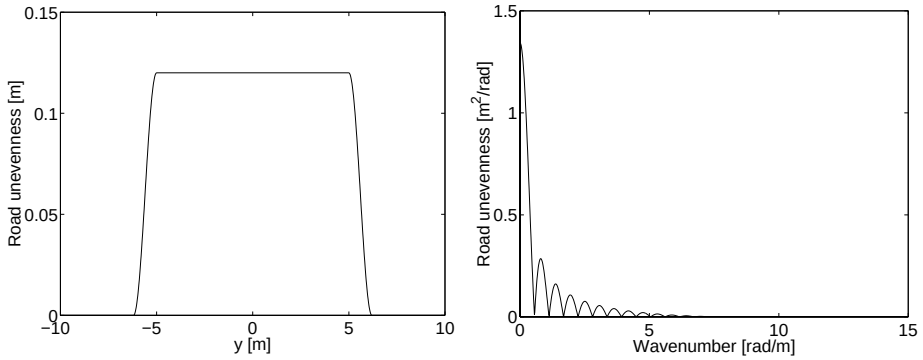


a. $u_{w/r}(y)$ b. $\tilde{u}_{w/r}(k_y)$

Figure 3.3: The longitudinal road profile of a traffic plateau with sine-shaped ramps (a) as a function of the coordinate $y$ along the road and (b) in the wavenumber domain.

The wavenumber content of the profile is:

$$\tilde{u}_{w/r}(k_y) = H(L+l)\text{sinc}\left[\frac{k_y(L+l)}{2}\right]\left[\frac{1}{1-\left[\frac{k_y l}{\pi}\right]^2}\right]\cos\left(\frac{k_y l}{2}\right) \tag{3.6}$$

As the area under the surface of the trapezoidal and the plateau with sine-shaped ramps are equal, the quasi-static value $H(L+l)$ at $k_y = 0$ is the same (figure 3.3b). The wavenumber content decreases and has small lobes with zeros at $k^0_{yn} = 2\pi n/(L+l)$ and large lobes at $k^0_{yn} = (2n-1)\pi/l$ that are not visible on figure 3.3b. The first zero $k^0_{y1}$ of the large lobes cancels the pole at $k_y = \pi/l$.

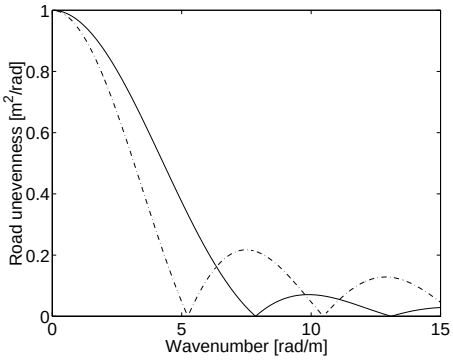


Figure 3.4: A comparison of the factor that distinguishes the wavenumber content of a plateau with a trapezoidal form (dash-dotted line) from a plateau with sine-shaped ramps (solid line) for ramps with a length $l = 1.20$ m.

The wavenumber content of both versions of the traffic plateau has a common part that is related to its height $H$ and mean length $L + l$. The factor that distinguishes between both shapes of the ramps only depends on the length $l$ of the ramps. Figure 3.4 shows this factor for ramps with a length $l = 1.20$ m. At limiting large wavenumbers, the factor tends to zero, inversely proportional to $k_y$ for the straight ramps and inversely proportional to $k_y^2$ for the sine-shaped ramps. For ramps with a smoother shape, the wavenumber content is therefore situated at lower wavenumbers or at larger wavelengths. For wavenumbers $k_y$ larger than a value of $5\pi/2l$ that is situated between the first zero of the plateau with straight ramps and the first zero of the plateau with sine-shaped ramps, the wavenumber content $\tilde{u}_{w/r}(k_y)$ of the trapezoidal plateau is generally larger. If the length $l$ is smaller than 0.5 m, the corresponding wavelength $\lambda_y = 4l/5$ is smaller than the relevant range of wavelengths.

The TRRL has performed practical tests to determine the free field vibration levels due to the passage of heavy vehicles on road humps and speed control cushions [7]. These tests have shown that for a plateau with a flat mid section $L = 6$ m and ramps with a length $l = 1$ m, the vibration levels that are generated by the passage on a plateau with sine-shaped ramps are slightly less than for a profile with straight ramps [8, 9]. The profiles with the steepest slopes cause the highest vibration levels in the free field. It can therefore be concluded that, more than the shape of the ramps, the slope of the ramps is the predominant factor for the generation of traffic induced vibrations. The wavenumber content of the sine-shaped bump (figure 3.1b) shows that, for standard heights, ramps with a length $l$ larger than 2.40 m are advantageous to avoid problems related to traffic induced vibrations.

Joints in a rigid concrete road surfacing are modelled in an approximating way as a step function with a height $H$:

$$u_{w/r}(y) = \begin{cases} -H/2 & y < 0 \\ +H/2 & y > 0 \end{cases} \tag{3.7}$$

Figure 3.5 shows the longitudinal profile for a joint with a height $H = 0.02$ m. Compared to equation (3.7), a vertical shift of $H/2$ has been applied to the unevenness $u_{w/r}(y)$.

The wavenumber content is equal to:

$$\tilde{u}_{w/r}(k_y) = \frac{iH}{k_y} \tag{3.8}$$

The wavenumber content $\tilde{u}_{w/r}(k_y)$ has an infinite value for $k_y$ tending to zero. Due to the fact that the profile is real and uneven with respect to $y = 0$, the wavenumber content is purely imaginary.

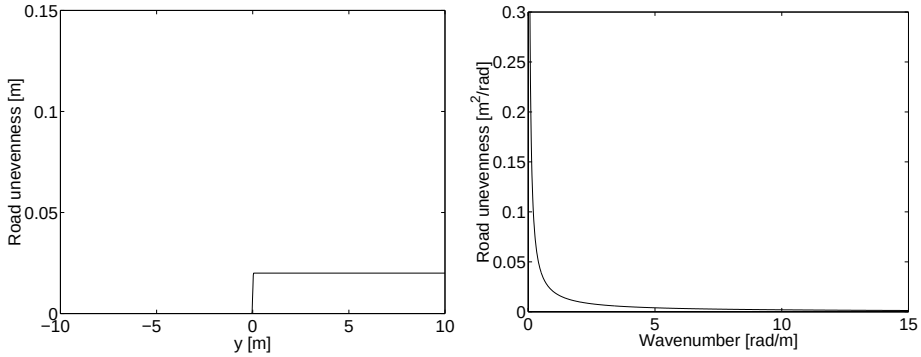


a. $u_{w/r}(y)$ b. $\tilde{u}_{w/r}(k_y)$

Figure 3.5: The longitudinal road profile of a joint with a height $H = 0.02$ m (a) as a function of the coordinate $y$ along the road and (b) in the wavenumber domain.

Figure 3.5 shows the longitudinal unevenness profile of the joint in the wavenumber domain. Compared to the wavenumber content (figure 3.1b) for a sine-shaped bump with a much larger height $H = 0.12$ m, the values in figure 3.5b are relatively large for wavenumbers $k_y \geq 2.5$ rad/m or wavelengths $\lambda_y \leq 2.5$ m. This is due to the fact that, for a limiting large wavenumber $k_y$, $\tilde{u}_{w/r}(k_y)$ tends to zero inversely proportional to $k_y$ in the case of the joint and $k_y^2$ in the case of the bump. For wavelengths $\lambda_y$ smaller than the footprint $p$ of the tyre or at wavenumbers $k_y \geq 2\pi/p$, the assumption of a point contact between the road and the vehicle is no longer valid [27, 68]. In this case, a filter can be applied to the wavenumber content to suppress the spurious components at small wavelengths or large wavenumbers [66, 67].

If the wavenumber content $\tilde{u}_{w/r}(k_y) = iH/k_y$ of a step with a height $H$ is introduced in equation (2.13), it follows that the frequency content $\hat{u}_{w/r}(\omega) = iH/v(-v/\omega) = -iH/\omega$ is not influenced by the vehicle speed $v$. For a linear vehicle model, the vehicle speed has no influence on the free field vibrations that are generated by the passage of each axle of the vehicle on a joint in the road surface. The total response is affected, however, by the fact that the time between the passage of each axle depends on the vehicle speed. This is confirmed by test results of Sutherland, who measured the vibrations in a timber frame house during the passage of two types of buses on articial profiles with a height $H$ from 0.03 m to 0.08 m and a total length of 0.33 m [15]. The profiles are only sloped at the ends and it can be assumed that the length of the ramps is small enough to approximate the slopes as a step function. For one type of bus, the vibration levels do not vary at all with the vehicle speed, while for the other type, the vibration levels increase with a factor of 1.5 for an increase of the vehicle speed $v$ from 16 km/h to 64 km/h. The increase is attributed to the fact that, at higher vehicle speeds, the effect of the loss of contact between the vehicle and the road becomes more important [15].

## 3.3 The vehicle FRF

### 3.3.1 The vehicle FRF's for a Volvo FE7 truck model

In the previous chapter, the eigenfrequencies and mode shapes of a 2D 17DOF Volvo FE7 truck model have been calculated. In the following, the vehicle FRF's of the same vehicle model are discussed. Furthermore, it is shown how the characteristics of the suspension system and the tyres and the vehicle body and axle mass influence the FRF's.

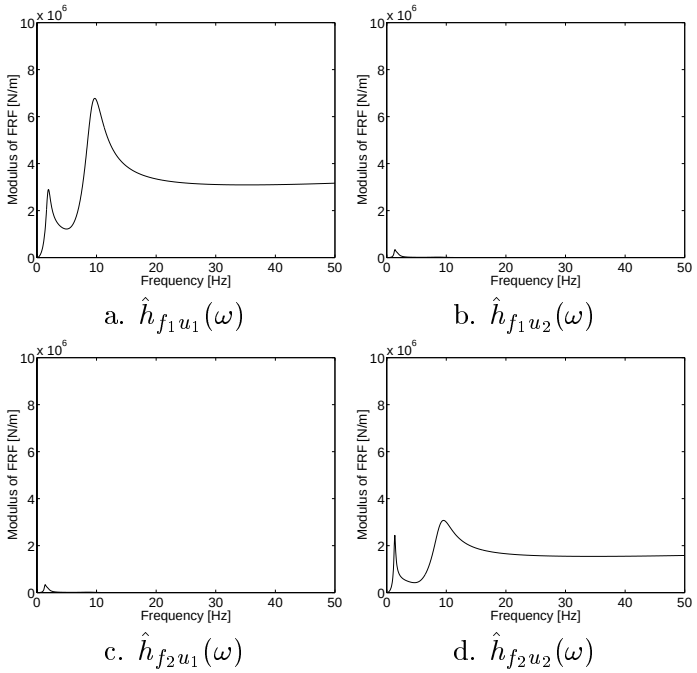


Figure 3.6: The vehicle FRF's $\hat{h}_{f_k u_l}(\omega)$ of the 4 DOF Volvo FE7 truck model.

Figure 3.6 shows the FRF's $\hat{h}_{f_k u_l}(\omega)$ of the 4 DOF Volvo FE7 truck model. The functions $\hat{h}_{f_k u_k}(\omega)$ represent the frequency content of the axle load at axle $k$ for an impulse excitation at the same axle and exhibit a peak value at the axle hop frequency. Compared to the FRF $\hat{h}_{f_k u_k}(\omega)$, the FRF $\hat{h}_{f_k u_l}(\omega)$ for an excitation at an axle $l \neq k$ are much smaller due to the weak coupling of the suspension systems at different axles. A peak value is obtained at the pitch and bounce frequency. Due to reciprocity, the FRF $\hat{h}_{f_k u_l} = \hat{h}_{f_l u_k}$. At limiting high frequencies, the FRF $\hat{h}_{f_k u_k}(\omega)$ tend to $k_t + i\omega c_t$, where $k_t$ and $c_t$ are the tyre stiffness and damping coefficient respectively, while the FRF $\hat{h}_{f_k u_l}(\omega)$ tend to zero.

### 3.3.2 The influence of the suspension characteristics

Figure 3.7 compares the vehicle FRF's of the original 4DOF Volvo FE7 truck model and the same model with the stiffness coefficient $k_{p2}$ of the front suspension multiplied by a factor of 1.5. As the FRF's $\hat{h}_{f_1 u_2}(\omega)$ and $\hat{h}_{f_2 u_1}(\omega)$ are identical, only the first one is shown. Figure 3.7a shows that the FRF $\hat{h}_{f_1 u_1}(\omega)$ of the rear axle is unaffected . The modulus of the small FRF $\hat{h}_{f_1 u_2}(\omega)$ is considerably larger, but remains relatively small. Figure 3.7c shows that an increase of the suspension stiffness shifts both the pitch and bounce and the axle hop frequency to a higher value. This is confirmed by the approximating equation (2.4) for the pitch and bounce and the axle hop frequencies. At the pitch and bounce frequency the modulus of $\hat{h}_{f_2 u_2}(\omega)$ increases, while at the axle hop frequency it decreases.

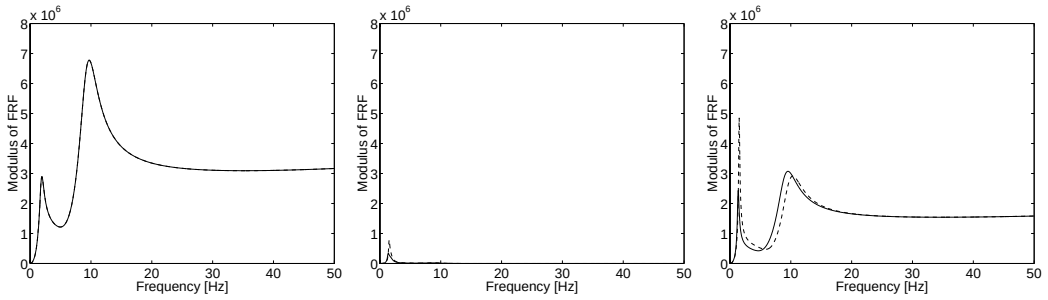


a. $\hat{h}_{f_1u_1}(\omega)$ b. $\hat{h}_{f_1u_2}(\omega)$ c. $\hat{h}_{f_2u_2}(\omega)$

Figure 3.7: The vehicle FRF's of the original 4DOF Volvo FE7 truck model (solid line) and the same model whith the stiffness coefficient $k_{p2}$ of the front suspension multiplied by a factor of 1.5 (dash-dotted line).

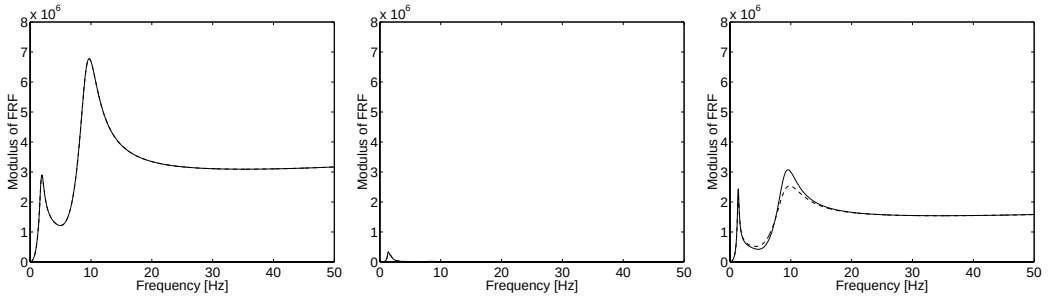


a. $\hat{h}_{f_1u_1}(\omega)$ b. $\hat{h}_{f_1u_2}(\omega)$ c. $\hat{h}_{f_2u_2}(\omega)$

Figure 3.8: The vehicle FRF's of the original 4DOF Volvo FE7 truck model (solid line) and the same model with the damping coefficient $c_{p2}$ of the front suspension multiplied by a factor of 1.5 (dashed line).

Figure 3.8 shows similar results for the case where the damping coefficient $c_{p2}$ of the front suspension is multiplied by a factor of 1.5. The FRF's $\hat{h}_{f_1u_1}(\omega)$ and $\hat{h}_{f_1u_2}(\omega)$ are unaffected. An increase of the damping coefficient $c_{p2}$ of the front suspension, however, has a considerable influence on $\hat{h}_{f_2u_2}(\omega)$. The modulus of the FRF increases at relatively low frequencies, while it decreases in the range of the axle hop frequency.

It can be concluded that a change of the characteristics of the suspension system of a particular axle of the vehicle only affects the FRF of the same axle.

### 3.3.3 The influence of the tyre characteristics

Figure 3.9 compares the vehicle FRF's of the original 4DOF Volvo FE7 truck model and the same model with the stiffness coefficient $k_{t2}$ of the front tyre multiplied by a factor of 1.5. The FRF's $\hat{h}_{f_1u_1}(\omega)$ (figure 3.9a) and $\hat{h}_{f_1u_2}(\omega)$ (figure 3.9b) remain unaffected. An increase of the tyre stifness $k_{t2}$ only shifts the axle hop frequency of the front axle to a higher value (equation 2.4), as illustrated in figure 3.9c. The modulus of $\hat{h}_{f_2u_2}(\omega)$ increases strongly at frequencies higher than the axle hop frequency.

Figure 3.10 shows similar results for the case where the damping coefficient $c_{t2}$ of the front tyre is multiplied by a factor of 1.5. The increase has no influence on the FRF's $\hat{h}_{f_1u_1}(\omega)$ (figure 3.10a) and

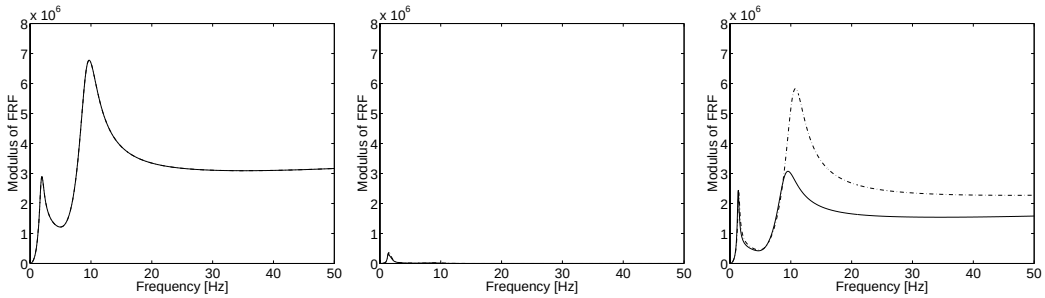


a. $\hat{h}_{f_1u_1}(\omega)$ b. $\hat{h}_{f_1u_2}(\omega)$ c. $\hat{h}_{f_2u_2}(\omega)$

Figure 3.9: The vehicle FRF's of the original 4DOF Volvo FE7 truck model (solid line) and the same model with the stiffness coefficient $k_{t2}$ of the front tyre multiplied by a factor of 1.5 (dashed line).

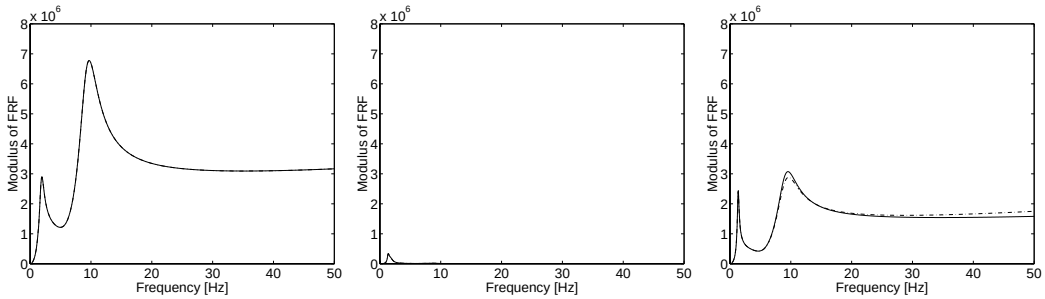


a. $\hat{h}_{f_1u_1}(\omega)$ b. $\hat{h}_{f_1u_2}(\omega)$ c. $\hat{h}_{f_2u_2}(\omega)$

Figure 3.10: The vehicle FRF's of the original 4DOF Volvo FE7 truck model (solid line) and the same model with the damping coefficient $c_{t2}$ of the front tyre multiplied by a factor of 1.5 (dashed line).

$\hat{h}_{f_1u_2}(\omega)$ (figure 3.10b). The influence on $\hat{h}_{f_2u_2}(\omega)$ (3.10c) is small as well, which is due to the low value of the damping coefficient of the tyre with respect to the damping coefficient of the suspension system. The FRF has a smaller modulus at the axle hop frequency and a larger modulus at higher frequencies.

### 3.3.4 The influence of the mass of the vehicle body and the axles

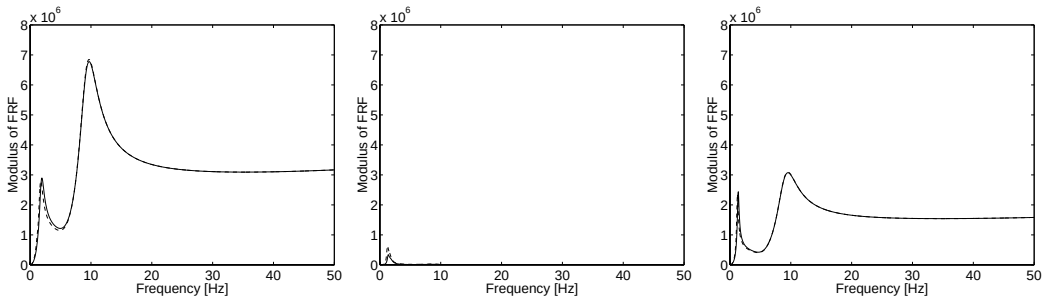


a. $\hat{h}_{f_1u_1}(\omega)$ b. $\hat{h}_{f_1u_2}(\omega)$ c. $\hat{h}_{f_2u_2}(\omega)$

Figure 3.11: The vehicle FRF's of the original 4DOF Volvo FE7 truck model (solid line) and the same model with the mass $m_b$ of the vehicle body multiplied by a factor of 1.5 (dashed line).

Figure 3.11 compares the vehicle FRF's of the original 4DOF Volvo FE7 truck model and the same model with the mass $m_b$ of the vehicle body multiplied by a factor of 1.5. An increase of the mass $m_b$ of the vehicle body lowers the pitch and bounce frequencies of both the front and the rear axle. The modulus of $\hat{h}_{f_1u_2}(\omega)$ increases, but remains relatively small, while the peak values of the moduli of $\hat{h}_{f_1u_1}(\omega)$ and $\hat{h}_{f_2u_2}(\omega)$ are almost unaffected.

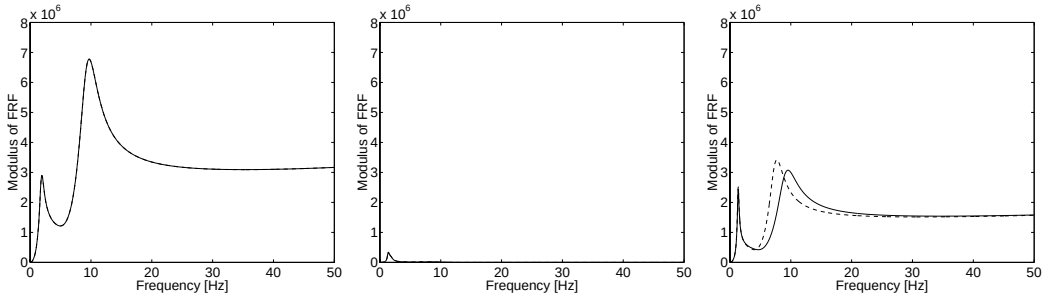


a. $\hat{h}_{f_1u_1}(\omega)$ b. $\hat{h}_{f_1u_2}(\omega)$ c. $\hat{h}_{f_2u_2}(\omega)$

Figure 3.12: The vehicle FRF's of the original 4DOF Volvo FE7 truck model (solid line) and the same model with the mass $m_{a2}$ of the front axle multiplied by a factor of 1.5 (dashed line).

Figure 3.12 shows similar results for the case where the mass $m_{a2}$ of the front tyre is multiplied by a factor of 1.5. The FRF's $\hat{h}_{f_1u_1}(\omega)$ (figure 3.12a) and $\hat{h}_{f_1u_2}(\omega)$ (figure 3.12b) remain unaffected. The increase of $m_{a2}$, however, shifts the axle hop frequency of the front axle to a higher value and increases slightly the modulus at the axle hop frequency.

The results suggest that the gross vehicle weight (GVW) does not play a large role in the generation of traffic induced vibrations. These observations are confirmed by experiments by the Transport and Road Research Laboratory (TRRL), where a comparison between the vibrations generated by an empty and a laden truck with an air suspension system did not show a significant difference [8]. The same experiment with a truck with a steel leaf suspension, however, showed that the unladen vehicle generates larger vibrations than the laden vehicle. This is due to the loss of contact between the road and the vehicle [8], a non-linear effect that is not taken into account in the present study. Although the difference between the vibrations generated by unladen and laden vehicles is not always clear, the heavier vehicle types are still responsible for the generation of the highest vibration levels.

## 3.4 The dynamic axle loads

In the following, the vehicle FRF of the 4DOF Volvo FE7 truck model (figure 3.6) are used in two examples for the prediction of the dynamic vehicle loads during the passage on a traffic plateau and the passage on a joint in a road surface, respectively.

### 3.4.1 A sine-shaped plateau

Figure 3.13 illustrates the calculation of the rear axle load during the passage of the Volvo FE7 truck on a traffic plateau with sine-shaped ramps at a vehicle speed $v = 14$ m/s. The plateau has a height $H = 0.12$ m, a flat mid section with a length $L = 10.0$ m and sine-shaped ramps with a length $l = 1.20$ m. At a time $t = 0$, the front axle of the vehicle is located at the centre of the plateau ($y_2 = 0$). The frequency content of the signal that is applied to the vehicle (figure 3.13a) is calculated with equation (2.13) from the wavenumber content in equation (3.6) (figure 3.3). It is calculated upto 50 Hz, with a

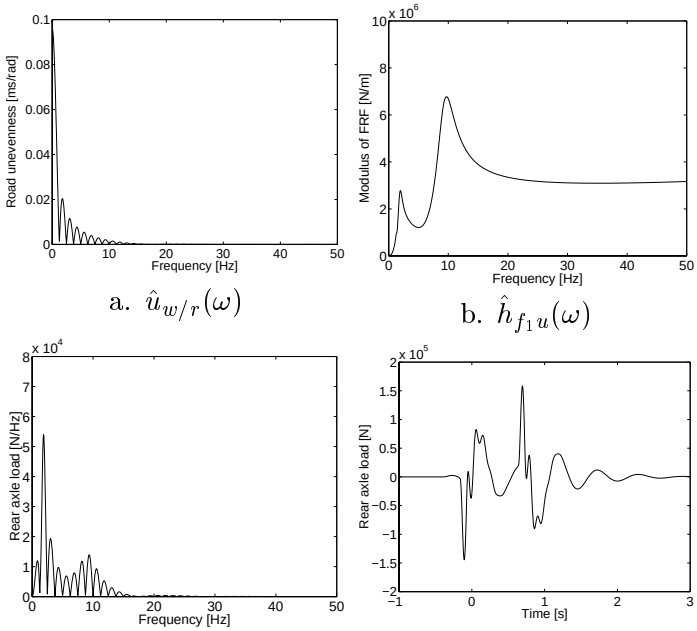


a. $\hat{u}_{w/r}(\omega)$ b. $\hat{h}_{f_1u}(\omega)$

c. $\hat{g}_1(\omega)$ d. $g_1(t)$

Figure 3.13: (a) Frequency content $\hat{u}_{w/r}(\omega)$ of the unevenness, (b) FRF $\hat{h}_{f_1u}(\omega)$, (c) frequency content $\hat{g}_1(\omega)$ and (d) time history $g_1(t)$ of the predicted rear axle load for the passage of the Volvo FE7 truck on a traffic plateau.

step $\Delta f = 0.0488$ Hz ($N = 2048$), corresponding to a period $T = 20.48$ s and a time step $\Delta t = 0.01$ s. As the circular frequency $\tilde{\omega} = -vk_y$, the separation between the lobes is proportional to the ratio of the vehicle speed $v$ and the mean length $L + l$.

The vehicle FRF $\hat{h}_{f_1u}(\omega)$ is composed of the FRF's $\hat{h}_{f_1u_1}(\omega)$ and $\hat{h}_{f_1u_2}(\omega)$, according to equation (2.14). The contribution of the FRF $\hat{h}_{f_1u_2}(\omega)$ is small.

The frequency content $\hat{g}_1(\omega)$ of the rear axle load in figure 3.13c is the product of the frequency content $\hat{u}_{w/r}(\omega)$ of the unevenness signal (figure 3.13a) and the FRF $\hat{h}_{f_1u}(\omega)$ (figure 3.13b). The frequency content is mainly situated below 15 Hz and is dominated by both the pitch and bounce mode and the axle hop mode of the rear axle.

An inverse Fast Fourier Transform (FFT) algorithm is used for the calculation of the time history $g_1(t)$ of the rear axle load (figure 3.13d). The time at which the axles mount and descend the traffic plateau can be estimated from the dimensions of the profile, the vehicle speed $v$, the wheel base $w$ of the vehicle and the initial position $y_2 = 0$ of the front axle. The mounting of the front axle at $t = -0.44$ s, does not generate a large impact. The peaks at $t = -0.16$ s and $t = 0.64$ s correspond to the mounting and descending of the rear axle on the plateau, respectively. The descending is followed by a free vibration that is dominated by the pitch and bounce mode.

### 3.4.2 A joint in the road surface

Compared to the case of the traffic plateau, the wavenumber content $\tilde{u}_{w/r}(k_y)$ for a joint in a road surface (figure 3.5b), decreases slowly with the wavenumber $k_y$. As a result, the wavenumber content $\tilde{u}_{w/r}(k_y)$ is relatively large at wavelengths $\lambda_y$ smaller than the footprint $p$ of the tyre or at wavenumbers $k_y \geq 2\pi/p$. At these small wavelengths, however, the assumption of a point contact between the road

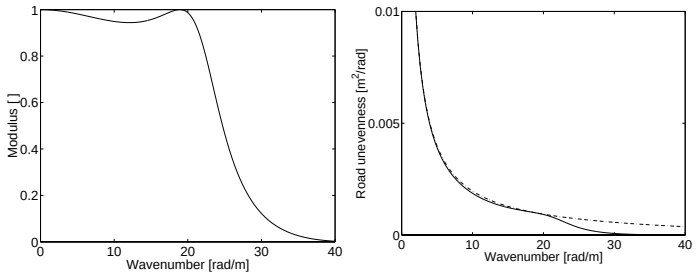


a. Chebyshev low-pass filter b. $\tilde{u}_{w/r}(k_y)$

Figure 3.14: (a) Second order Chebyshev low-pass filter with a cut-off wavenumber $k_y = 2\pi/0.3$ rad/m and (b) comparison of the original (dash-dotted line) and filtered (solid line) wavenumber content $\tilde{u}_{w/r}(k_y)$ of the unevenness profile of a joint in a road surface.

and the vehicle is no longer valid [27, 68]. In the case of railway traffic, Knothe and Grassie [66] apply a filter on the roughness profile of the rails and wheels to suppress the spurious components at small wavelengths or large wavenumbers. Following the same approach, the wavenumber content $\tilde{u}_{w/r}(k_y)$ of the unevenness profile is filtered with a second order Chebyshev low-pass filter with a cut-off wavenumber $k_y = 2\pi/p$, which is equal to 20.9 rad/m for a footprint $p$ with an estimated length of 0.3 m (figure 3.14a). Similar as the filter described by Müller and Knothe [67] for the rail unevenness, the modulus of the filter has a value of nearly one for wavenumbers that are much smaller than $k_y = 2\pi/p$, decreases for higher wavenumbers and almost vanishes at $k_y = 4\pi/p$. Figure 3.14b shows how the filter preserves the contribution at small wavenumbers, while for wavenumbers larger than $k_y = 2\pi/p$, the wavenumber content decreases fast with increasing $k_y$.

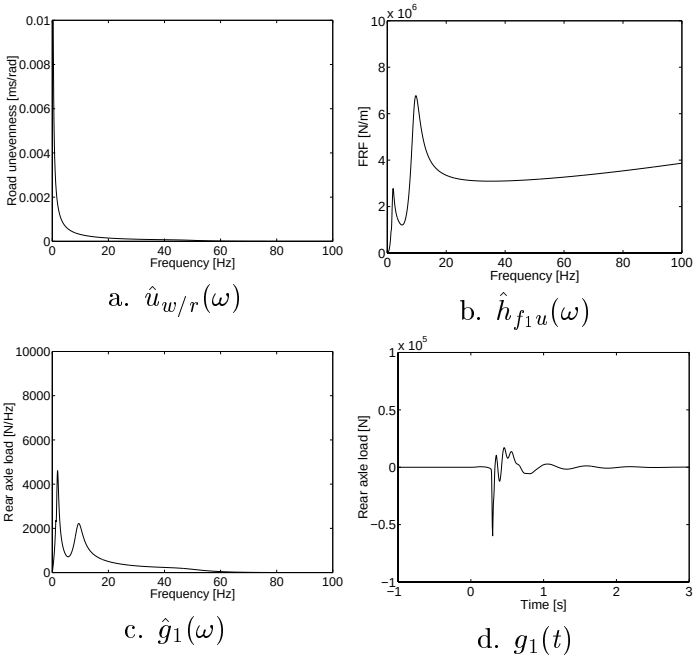


a. $\hat{u}_{w/r}(\omega)$ b. $\hat{h}_{f_1 u}(\omega)$

c. $\hat{g}_1(\omega)$ d. $g_1(t)$

Figure 3.15: (a) Frequency content $\hat{u}_{w/r}(\omega)$ of the unevenness, (b) FRF $\hat{h}_{f_1 u}(\omega)$, (c) frequency content $\hat{g}_1(\omega)$ and (d) time history $g_1(t)$ of the predicted rear axle load for the passage of the Volvo FE7 truck on a joint in a road surface.

Figure 3.15 illustrates the calculation of the rear axle load during the passage of the Volvo FE7 truck on a joint in a road surface with a height $H = 0.02$ m at a vehicle speed $v = 14$ m/s. At a time $t = 0$, the front axle is located at the joint in the surface ($y_2 = 0$). The filtered wavenumber content $\tilde{u}_{w/r}(k_y)$ in figure 3.14b is used for the calculation of the frequency content $\hat{u}_{w/r}(\omega)$ of the signal that is applied to the vehicle (figure 3.15a). The frequency content is calculated upto 100 Hz, with a step $\Delta f = 0.0488$ Hz ($N = 4096$), corresponding to a period $T = 20.48$ s and a time step $\Delta t = 0.005$ s. Equation (2.13) shows that the cut-off wavenumber $k_y = 2\pi/0.3$ rad/m corresponds to a cut-off frequency $\omega = -vk_y$ or $f = 46.7$ Hz. The suppressed frequency range above 50 Hz is generally irrelevant for road traffic induced vibrations. Compared to the frequency content of the plateau in figure 3.13a, the relative importance of the contribution at higher frequencies is still larger. The same conclusion holds for the frequency content of the rear axle load in figure 3.15c. The time history in figure 3.15 shows a sharp peak at the passage of the rear axle on the joint. Although the height of the joint is much smaller than the height of the plateau, the peak value of the axle load in figure 3.15d has the same order of magnitude as the axle load in figure 3.13d. The free vibration is dominated by both the axle hop and the pitch and bounce mode of the rear axle.

## 3.5 The free field vibrations

### 3.5.1 Introduction

In the following, the dynamic axle loads that have been calculated in figures 3.13 and 3.15 are used to predict the free field vibrations for the passage of a Volvo FE7 truck on a traffic plateau with sine-shaped ramps and a joint in a road surface, respectively.

| layer | type | $d$ [m] | $\nu$ [-] | $\rho$ [kg/m$^3$] | $E$ [$\times 10^6$ N/m$^2$] |
|---|---|---|---|---|---|
| 1 | asphalt | 0.14 | 1/3 | 2100 | 15000 |
| 2 | lean concrete | 0.20 | 1/3 | 1750 | 15000 |
| 3 | granular subbase | 0.25 | 1/2 | 1800 | 200 |

Table 3.1: Road section.

The road has a width $2B$=3 m and is supported by a homogeneous halfspace. The road is composed of an asphalt top layer with a thickness of 0.14 m, a lean concrete layer of 0.20 m and a granular subbase of 0.25 m (table 3.1). The following equivalent characteristics are used for the calculation of the road's impedance (2.20): $EI = 1.611 \times 10^8$ Nm$^2$, $\rho A = 3.282 \times 10^3$ kg/m, $\rho I_p = 2.605 \times 10^3$ kgm and $GC = 2.032 \times 10^8$ Nm$^2$.

The soil is modelled as a homogenous halfspace with a density $\rho = 1800\,\mathrm{kg/m^3}$, a shear wave velocity $C_s = 150\,\mathrm{m/s}$, a dilatational wave velocity $C_p = 300\,\mathrm{m/s}$ and a hysteretic material damping ratio $\beta = 0.025$ in shear and volumetric deformation. The ratio $s$ of the body wave velocities $C_s$ and $C_p$ is equal to $\sqrt{(1-2\nu)/(2-2\nu)}$ and only depends on the Poisson's ratio $\nu$; $s$ is equal to 0.5 if $\nu = 1/3$.

### 3.5.2 A sine-shaped plateau

The free field velocities are calculated by means of equation (2.44) for three receivers, located at the soil's surface ($z = 0$ m) at a distance of 8 m, 24 m and 40 m from the road's axis. For the case of the plateau with sine-shaped ramps, the frequency content $\hat{v}_{si}(x, y = 0, z = 0, \omega)$ of the free field velocity is calculated upto a frequency $f = 50$ Hz, with $\Delta f = 0.0488$ Hz ($N = 2048$), corresponding to a period

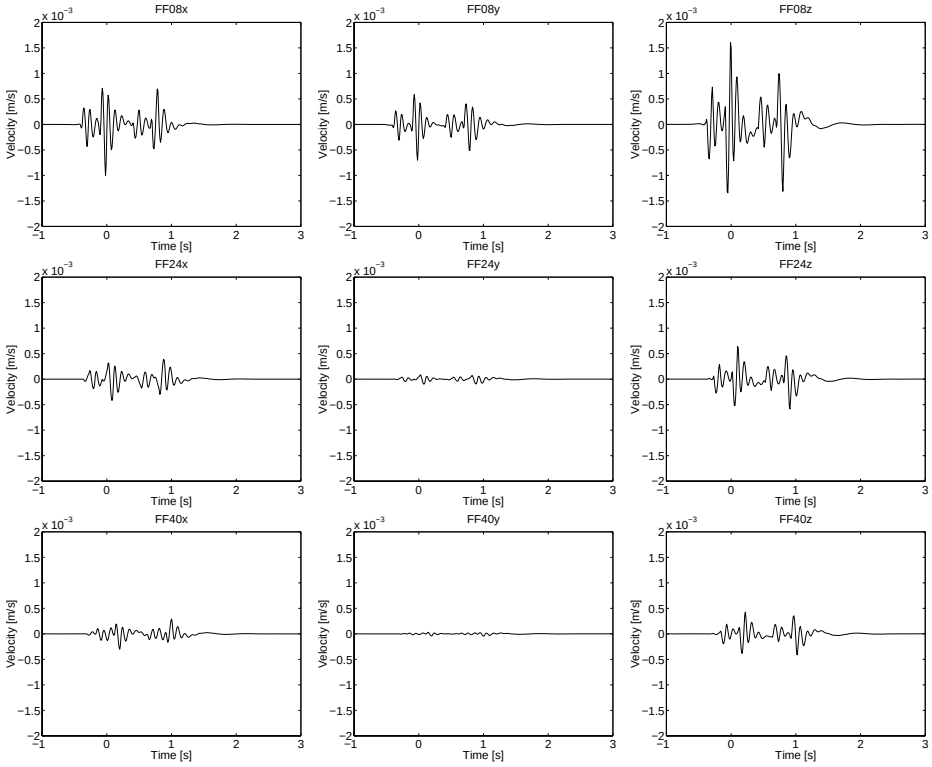


Figure 3.16: Time history of the free field velocity $v_{si}(x, y = 0, z = 0, t)$ at a distance $x$, equal to 8, 24 and 40 m due to the passage of a Volvo FE7 truck on a traffic plateau with sine-shaped ramps.

$T = 20.48$ s and a time step $\Delta t = 0.01$ s. The time history of the free field velocity is calculated by means of an inverse FFT algorithm.

Figure 3.16 shows the free field velocity $v_{si}(x, y = 0, z = 0, t)$ during the passage of the Volvo FE7 truck on the plateau with sine-shaped ramps. Each signal is denoted by a label `FFij`, where `FF` denotes the free field, `i` the distance $x$ from the source and `j` the displacement component. The time at which the front axle mounts is estimated as $t = -0.44$ s, while at $t = 0.64$ s, the front axle descends the profile. The separation in time between both impacts is more pronounced at a small distance $x$ from the road centre. When the time of arrival and the amplitude of the free field vibrations with increasing distance $x$ are compared, it is observed that wave propagation in the soil delays and attenuates the response. The free field velocity components $v_{sx}$ and $v_{sz}$ have the same order of magnitude. At a large distance $x$ with respect to the dimensions of the plateau, $v_{sy}$ approximates the zero out-of-plane component of the generated waves.

The vertical peak particle velocity (PPV) equals 1.6 mm/s, 0.6 mm/s and 0.4 mm/s at a distance $x$ equal to 8 m, 24 m and 40 m, respectively. At 8 m from the centre of the road, the ascending generates slightly higher vibration levels than the descending. At larger distances from the road, the difference between the vibration levels at both impacts becomes smaller. This is due to the fact that the distance travelled by the contact point between the road and the vehicle is small compared to the distance $x$ between the contact point and the receivers. From the time history of the rear axle load (figure 3.13), the duration $t_d$ of the impact load at the mounting is estimated as 0.4 s. This corresponds to a distance $vt_d = 5.6$ m that is travelled by the rear axle. For a receiver at a large distance compared to $vt_d$, the moving impact load seems applied at a fixed position. In this case, both impacts generate similar vibration levels and the horizontal components of the free field response can be decomposed into an in-plane and a zero out-of-plane component.

The empirical formula of the Transport and Road Research Laborotory in equation (1.1) is used to estimate the vertical PPV. In this case, the height $H = 120$ mm, the speed $v = 50.4$ km/h, $p = 1$ (the unevenness is present in both wheel paths) and the distance $r = \sqrt{(x - 0.75)^2 + 6.20^2}$. For a sandy soil with a medium value of the stiffness, the ground scaling factor $s = 0.94$ and the power coefficient $n = -0.74$. The empirically predicted peak particle velocities equal 2.4 mm/s, 1.2 mm/s and 0.8 mm/s, respectively, and agree reasonably well with the previously computed values. In order to check the predictive qualities of the empirical model, both methods are compared once again in the next subsection for the passage of the vehicle on the joint.

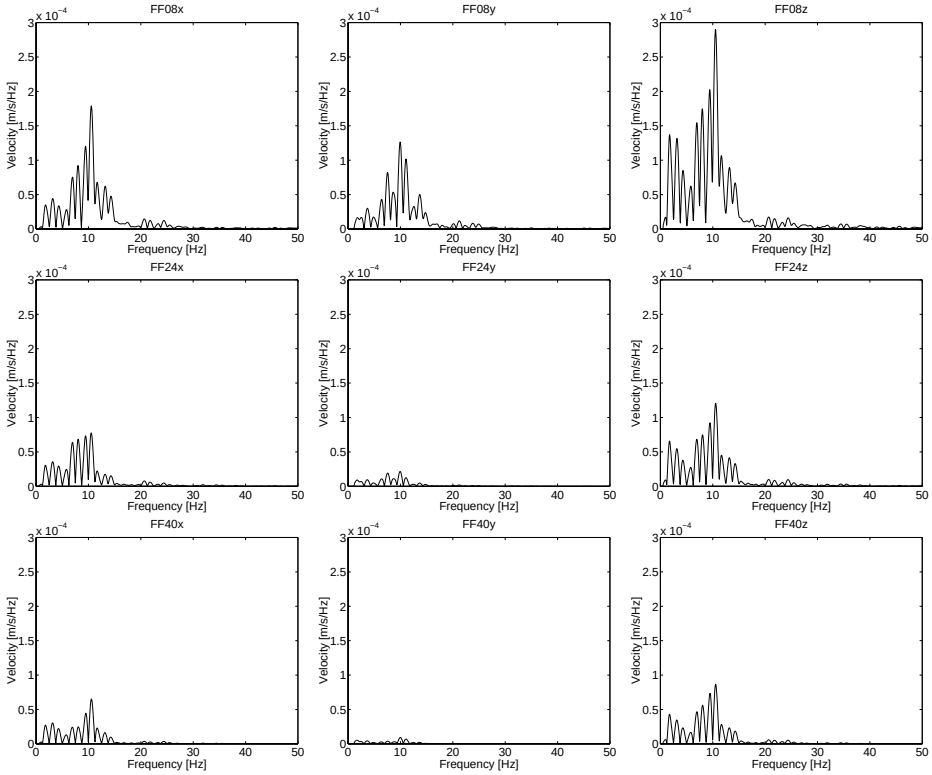


Figure 3.17: Frequency content of the free field velocity $\hat{v}_{si}(x, y = 0, z = 0, \omega)$ at a distance $x$, equal to 8, 24 and 40 m due to the passage of a Volvo FE7 truck on a traffic plateau with sine-shaped ramps.

Figure 3.17 shows the frequency content $\hat{v}_{si}(x, y = 0, z = 0, \omega)$ of the free field velocity. The lobed behaviour is related to the mean length $L + l$ of the profile and the vehicle speed $v$. Whereas the pitch and bounce mode dominate the frequency content of the axle loads (figure 3.13), the axle hop modes dominate the free field response. The contribution at higher frequencies is damped out more severely with an increasing distance from the source.

### 3.5.3 A joint in the road surface

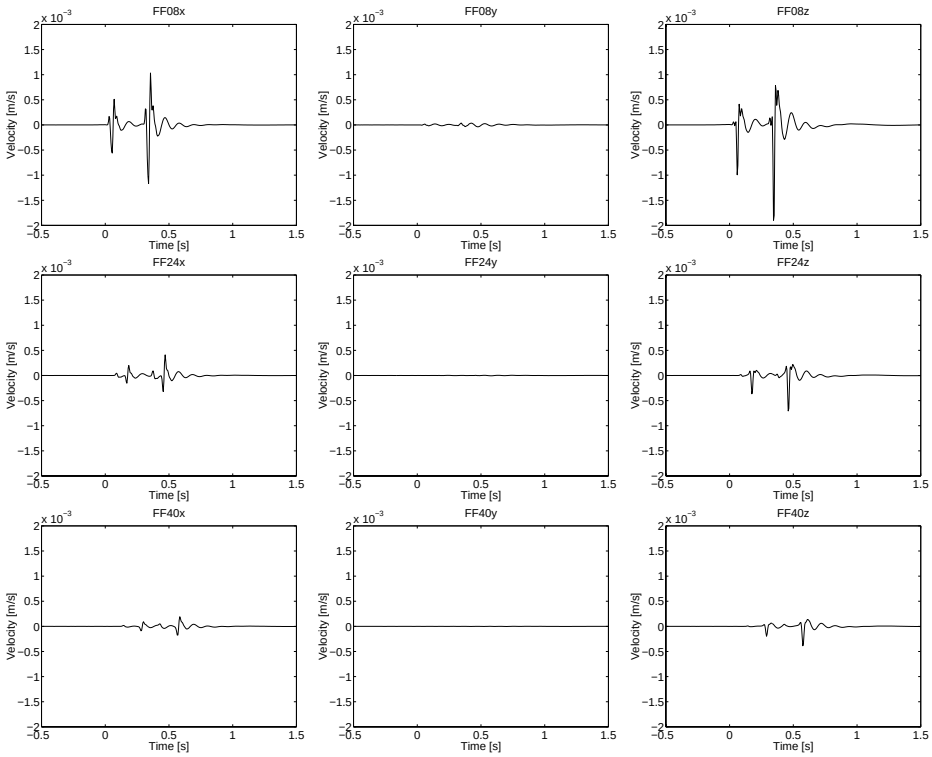


Figure 3.18: Time history of the free field velocity $v_{si}(x, y = 0, z = 0, t)$ at a distance $x$, equal to 8, 24 and 40 m due to the passage of a Volvo FE7 truck on a joint in the road surface.

For the case of a joint in the road surface, the frequency content $\hat{v}_{si}(\omega)$ of the free field velocity is calculated upto a frequency $f = 100$ Hz, with $\Delta f = 0.0488$ Hz ($N = 4096$), corresponding to a period $T = 20.48$ s and a time step $\Delta t = 0.005$ s. Figure 3.16 shows the time history $v_{si}(x, y = 0, z = 0, t)$ of the free field velocity during the passage of the Volvo FE7 truck on the joint. The impacts during the passage of the front and the rear axle of the vehicle result in sharp peaks that are well separated in time. The vertical PPV equals 2.3 mm/s, 0.8 mm/s and 0.4 mm/s at a distance $x$ equal to 8 m, 24 m and 40 m, respectively. As in the case of the traffic plateau, the distance that is travelled by the vehicle during the impact is relatively small and the source appears to be applied at a fixed position for the receivers at a large distance $x$ from the road. As a result, $v_{sy}(t)$ approximates the zero out-of-plane horizontal component. Although the ramps of the traffic plateau are at a larger distance from the receiver than the joint, it can still be expected that the peak particle velocity in both cases has the same order of magnitude. This is due to the fact that in the relevant range of wavenumbers $k_y$ between 2.5 rad/m and 2.5 rad/m, both types of unevenness have a wavenumber content of the same order of magnitude.

The empirical formula of the Transport and Road Research Laborotory in equation (1.1) is used once again to estimate the vertical PPV. Only the height $H = 20$ mm and the distance $r = x - 0.75$ between the source and the receiver are different from the values in the first case. The predicted vertical PPV's are 0.5 mm/s, 0.2 mm/s and 0.1 mm/s, respectively, and are significantly lower than the previously computed values. Whereas in the first case, the empirical formula overestimates the PPV, the PPV's are seriously underestimated in this case. This is due to the fact that the formula does not account for the shape of the longitudinal unevenness.

Figure 3.19 shows the frequency content $\hat{v}_{si}(x, y = 0, z = 0, \omega)$ of the free field velocity. The frequency

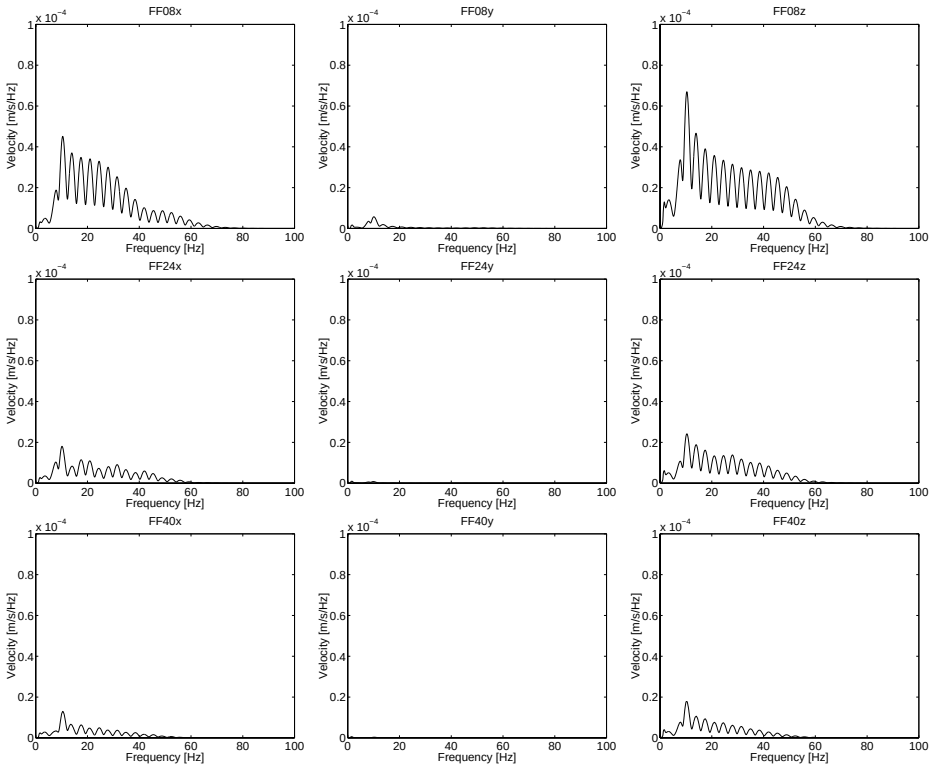


Figure 3.19: Frequency content of the free field velocity $\hat{v}_{si}(x, y = 0, z = 0, t)$ at a distance $x$, equal to 8, 24 and 40 m due to the passage of a Volvo FE7 truck on a joint in the road surface.

content is modulated at a wheel base frequency $f_w = v/w = 3.5$ Hz, where $w$ is the wheel base of the truck. As in the case of the traffic plateau, the axle hop modes dominate the frequency content of the free field response. The fast decrease of the frequency content at $x = 8$ m for frequencies $f \geq 50$ Hz, is due to the use of the Chebyshev filter for the wavenumber content of the unevenness profile. At $x = 40$ m, however, the influence of the latter is negligible, as the response at relatively high frequencies is attenuated considerably with increasing distance $x$.

### 3.5.4 An alternative sine-shaped plateau

The wavenumber content of a sine-shaped bump (figure 3.1b) with a length $L = 4.80$ m is much lower for wavenumbers $k_y \geq 2.5$ rad/m than in the case of a plateau with sine-shaped ramps with a length $l = 1.20$ m (figure 3.3b). This is due to the fact that the slopes of the bump are less steep than the ramps of the plateau. It is therefore interesting to calculate the free field vibrations for the passage of a Volvo FE7 truck on a plateau with the same mean length $L + l$ and height $H$, but with longer ramps with a length $l = 2.40$ m. This results in a flat mid section with a length $L = 8.80$ m.

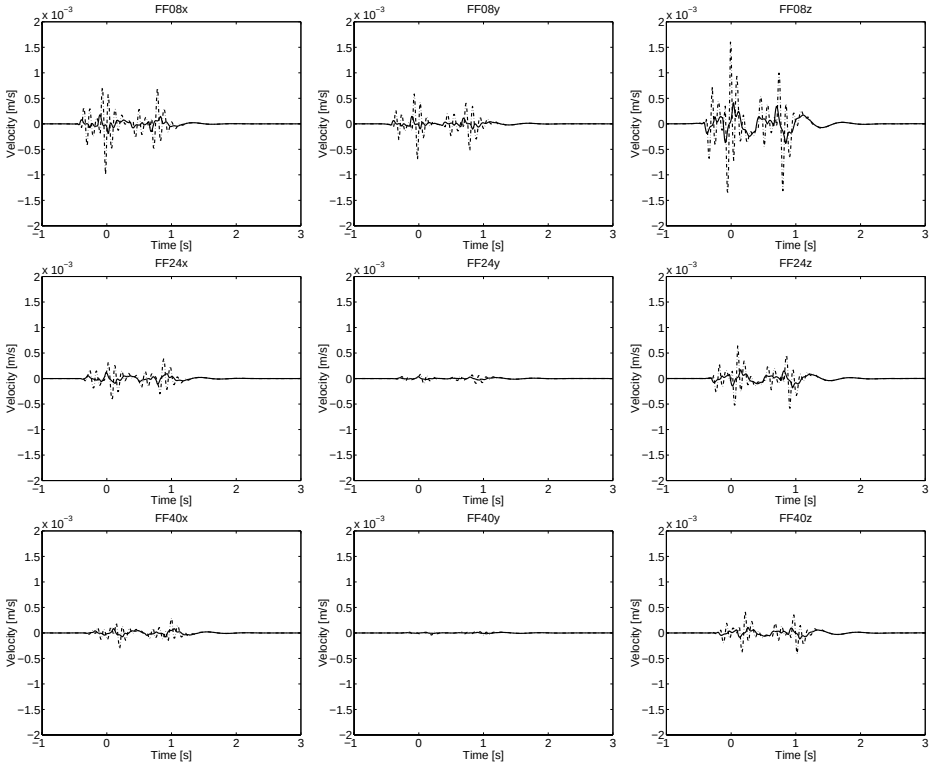


Figure 3.20: Time history of the free field velocity $v_{si}(x, y = 0, z = 0, t)$ at a distance $x$, equal to 8, 24 and 40 m due to the passage of a Volvo FE7 truck on a plateau with sine-shaped ramps with a length $l = 1.20$ m (dash-dotted line) and $l = 2.40$ m (solid line).

| Location | 8 m | 16 m | 24 m | 32 m | 40 m |
|---|---|---|---|---|---|
| $l = 1.20$ m | 1.6 | 0.9 | 0.6 | 0.5 | 0.4 |
| $l = 2.40$ m | 0.4 | 0.3 | 0.2 | 0.1 | 0.1 |

Table 3.2: Vertical peak particle velocity (mm/s) for the passage of a Volvo FE7 truck on a sine-shaped plateau with ramps with a length $l = 1.20$ m and $l = 2.40$ m.

Figure 3.20 compares the time history of the free field vibrations generated by the passage of a Volvo FE7 truck on a sine-shaped plateau with ramps with a length $l = 1.20$ m and $l = 2.40$ m. In the first case, the mean slope of the ramp is 10 %, whereas in the second case it is 5 %. Table 3.2 compares the vertical peak particle velocity as a function of the distance from the road's centre. These results show a very significant reduction of the free field vibrations that are generated by the passage of the truck. The transient signals in the free field do not show sharp peaks and the peak particle velocity

is reduced by a factor of 3 to 4.

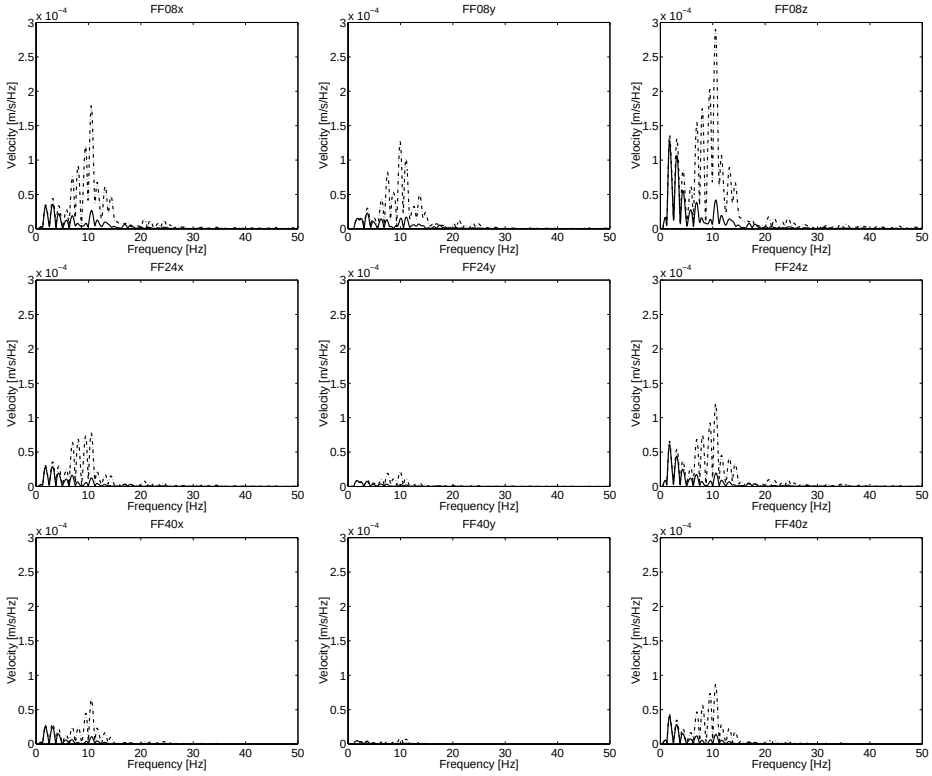


Figure 3.21: Frequency content of the free field velocity $\hat{v}_{si}(x, y = 0, z = 0, \omega)$ at a distance $x$, equal to 8, 24 and 40 m due to the passage of a Volvo FE7 truck on a plateau with sine-shaped ramps with a length $l = 1.20$ m (dash-dotted line) and $l = 2.40$ m (solid line).

Figure 3.21 compares the frequency content of the free field velocity in both cases. At low frequencies, the frequency content coincides. This is due to the fact that, at low wavenumbers, the wavenumber content of the profile is mainly determined by the height $H$ and the mean length $L + l$ of the profile. As a result, the same parameters determine the frequency content of the unevenness, the axle loads and the free field vibrations at low frequencies. At higher wavenumbers the influence of the length $l$ of the ramps becomes more important. For a fixed mean length $L + l$, the wavenumber content shifts to lower wavenumbers for a larger length $l$. A larger length $l$ will therefore also reduce the frequency content of the free field vibrations at higher frequencies. As a result, the frequency content of the free field vibrations at 10 Hz is reduced by a factor of 6 for a length $l = 2.40$ m, compared to the case where $l = 1.20$ m.

It is concluded that for situations where hindrance due to traffic induced vibrations is expected, a mean slope of 5 % is advisable. This corresponds to the regulations in the Belgian Royal Decree of 9 October 1998, where a slope of 5 % is imposed for roads that are frequently used by buses and heavy traffic. Equations (2.13) and (3.6) indicate that, for a fixed mean length $L + l$, the ratio $v/l$ determines the frequency content of the unevenness. If the length $l$ of the ramps doubles, the same vibration levels are generated for a passage of the vehicle at a double vehicle speed $v$.

### 3.5.5 The influence of the road's structure

In order to investigate the influence of the road's structure, the previous computation of the free field vibrations is recapitulated for a road with a different cross section. As experiments that have been carried out in the past [15, 22] indicate that the influence of the road's structure on the free field vibrations is small, a rather unrealistic case is considered, where the thickness of the layers of the road section in table 3.1 is multiplied by a factor of 3. The alternative road section is composed of an asphalt top layer with a thickness of 0.42 m, a lean concrete layer of 0.60 m and a granular subbase of 0.75 m (table 3.3). The following equivalent characteristics are computed: $EI = 43.50 \times 10^8\,\mathrm{Nm}^2$, $\rho A = 9.846 \times 10^3\,\mathrm{kg/m}$, $\rho I_p = 11.26 \times 10^3\,\mathrm{kgm}$ and $GC = 49.43 \times 10^8\,\mathrm{Nm}^2$. The section in table 3.1 is referred to as section 1, whereas the section in table 3.3 is referred to as section 2.

| layer | type | $d$ [m] | $\nu$ [-] | $\rho$ [kg/m$^3$] | $E$ [$\times 10^6$ N/m$^2$] |
|---|---|---|---|---|---|
| 1 | asphalt | 0.42 | 1/3 | 2100 | 15000 |
| 2 | lean concrete | 0.60 | 1/3 | 1750 | 15000 |
| 3 | granular subbase | 0.75 | 1/2 | 1800 | 200 |

Table 3.3: Road section 2.

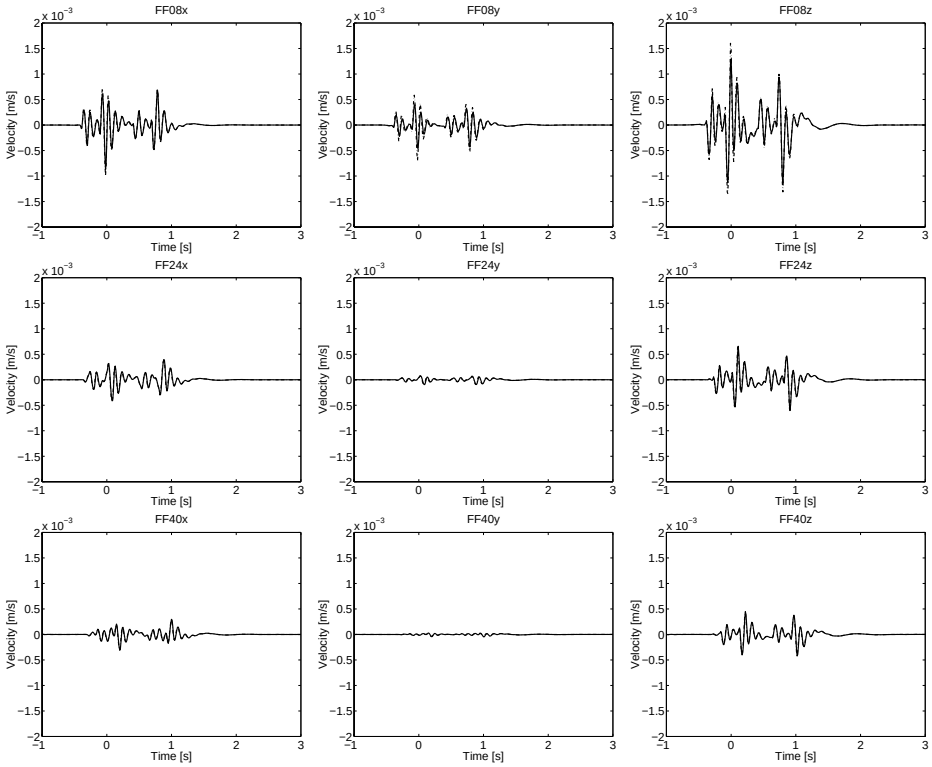


Figure 3.22: Time history of the free field velocity $v_{si}(x, y = 0, z = 0, t)$ at a distance $x$, equal to 8, 24 and 40 m due to the passage of a Volvo FE7 truck on a traffic plateau with sine-shaped ramps for road section 1 (dash-dotted line) and road section 2 (solid line) where the thickness of the layers of section 1 is multiplied by a factor of 3.

Figure 3.22 compares the time history of the free field vibrations generated by the passage of a Volvo FE7 truck on a traffic plateau with sine-shaped ramps for the case where the road is composed of

| Location | 8 m | 16 m | 24 m | 32 m | 40 m |
|---|---|---|---|---|---|
| Section 1 | 1.6 | 0.9 | 0.6 | 0.5 | 0.4 |
| Section 2 | 1.3 | 0.9 | 0.7 | 0.5 | 0.4 |

Table 3.4: Vertical peak particle velocity (mm/s) for the passage of a Volvo FE7 truck on a traffic plateau for road section 1 and road section 2 where the thickness of the layers of section 1 is multiplied by a factor of 3.

the section in table 3.1 and for the alternative section presented in table 3.3. Table 3.4 compares the vertical peak particle velocity as a function of the distance from the road's centre. Although the thickness of the layers of the alternative road section has an unrealistic high value and the stiffness and inertial terms are much larger, the vibration levels do not differ a lot. Only at 8 m from the centre of the road, the free field velocities differ significantly.

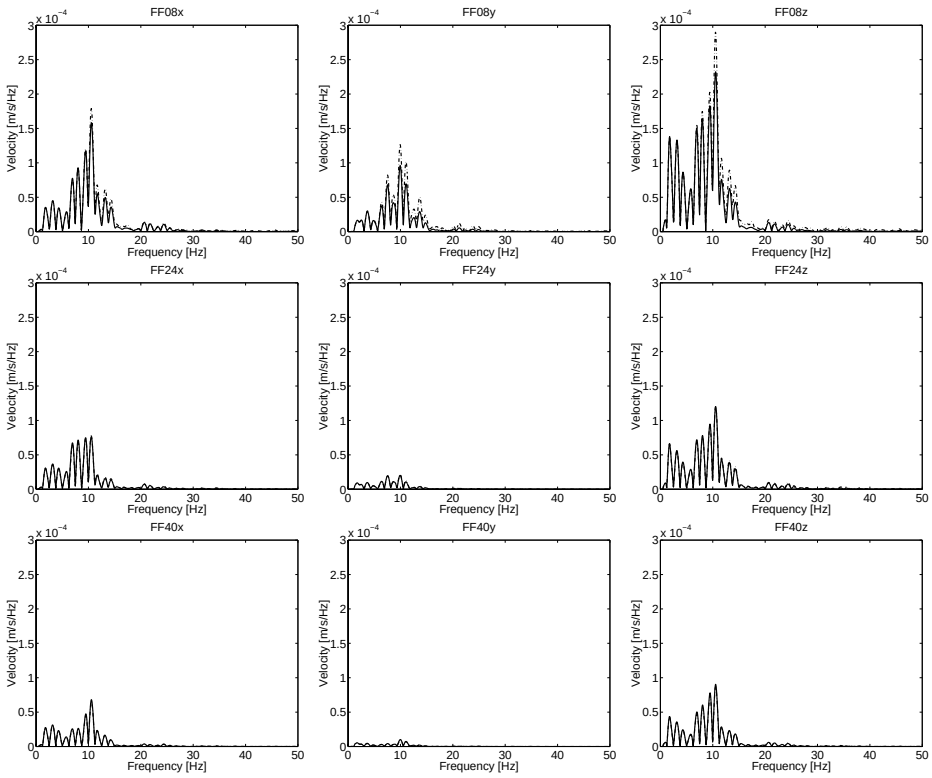


Figure 3.23: Frequency content of the free field velocity $\hat{v}_{si}(x, y = 0, z = 0, \omega)$ at a distance $x$, equal to 8, 24 and 40 m due to the passage of a Volvo FE7 truck on a traffic plateau with sine-shaped ramps for road section 1 (dash-dotted line) and road section 2 (solid line) where the thickness of the layers of section 1 is multiplied by a factor of 3.

Figure 3.23 compares the frequency content. Only at 8 m from the road's centre, the frequency content differs significantly. At low frequencies, where the wavelength in the soil is large compared to the dimensions of the road, the results coincide. At higher frequencies, the frequency content of the vibrations that are generated by the passage on section 2 becomes smaller than for the section 1. The difference between the results diminishes for an increasing distance from the road, as the contribution at higher frequencies is attenuated more rapidly.

The foregoing observations are confirmed by test results of Sutherland, who investigated the vibrations

induced by the passage of two types of buses on articial profiles with a height $H$ ranging from 0.03 m to 0.08 m and a total length of 0.33 m [15]. At the same site, the profiles have been installed on two neighbouring driving lanes of the same road. At the first and outer driving lane, the road has a thickness of 0.27 m, while at the second, centre driving lane, the thickness of the road is 0.66 m. The vibration levels in a nearby timber frame house do not differ significantly in both cases. At the Transport and Road Research Laboratory, a lot of measurement campaigns have been performed to measure the transfer function between the road and a point in the free field. A comparison between the value of the transfer function at a distance of 6 m and at a frequency of 12 Hz for a rigid road with an upper concrete layer of 0.26 m and a road with an asphalt top layer of 0.21 m, located at the same site, showed no significant differences [22].

### 3.5.6 The influence of the soil's material damping

The soil's stratification and its dynamic stiffness properties can be experimentally determined by means of a spectral analyses of surface waves (SASW) test or a seismic cone penetration test (SCPT). The soil's material damping, however, is a parameter that is much harder to determine. It has a large influence on the response at a large dimensionless distance from the source and at high frequencies. In order to illustrate its influence, the free field vibrations during the passage of the Volvo FE7 truck on the plateau with sine-shaped ramps have been recalculated for the case where the soil's hysteretic material damping ratio $\beta$ equals 0.050 in shear and volumetric deformation.

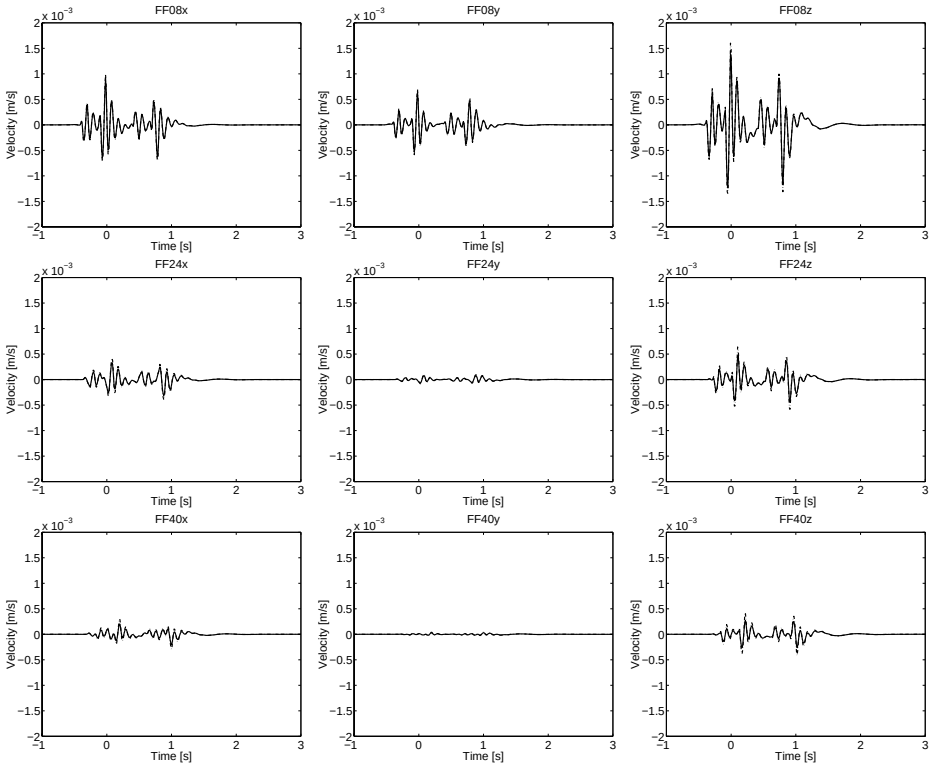


Figure 3.24: Time history of the free field velocity $v_{si}(x, y = 0, z = 0, t)$ at a distance $x$, equal to 8, 24 and 40 m due to the passage of a Volvo FE7 truck on the traffic plateau with sine-shaped ramps for the case where the soil's hysteretic damping ratio $\beta$ equals 0.025 (dash-dotted line) and 0.050 (solid line).

Figure 3.24 compares the time history of the free field vibrations generated by the passage of the Volvo

| Location | 8 m | 16 m | 24 m | 32 m | 40 m |
|---|---|---|---|---|---|
| $\beta = 0.025$ | 1.6 | 0.9 | 0.6 | 0.5 | 0.4 |
| $\beta = 0.050$ | 1.4 | 0.8 | 0.5 | 0.4 | 0.3 |

Table 3.5: Vertical peak particle velocity (mm/s) for the passage of a Volvo FE7 truck on a traffic plateau for the case where the soil's hysteretic damping ratio $\beta$ equals 0.025 and 0.050.

FE7 truck on the traffic plateau for the case where the soil has a material damping ratio $\beta$ equal to 0.025 and 0.050, respectively. Table 3.5 compares the vertical peak particle velocity as a function of the distance from the road's centre. Figure 3.24 and table 3.5 illustrate that the influence of the soil's material damping increases with the distance from the source.

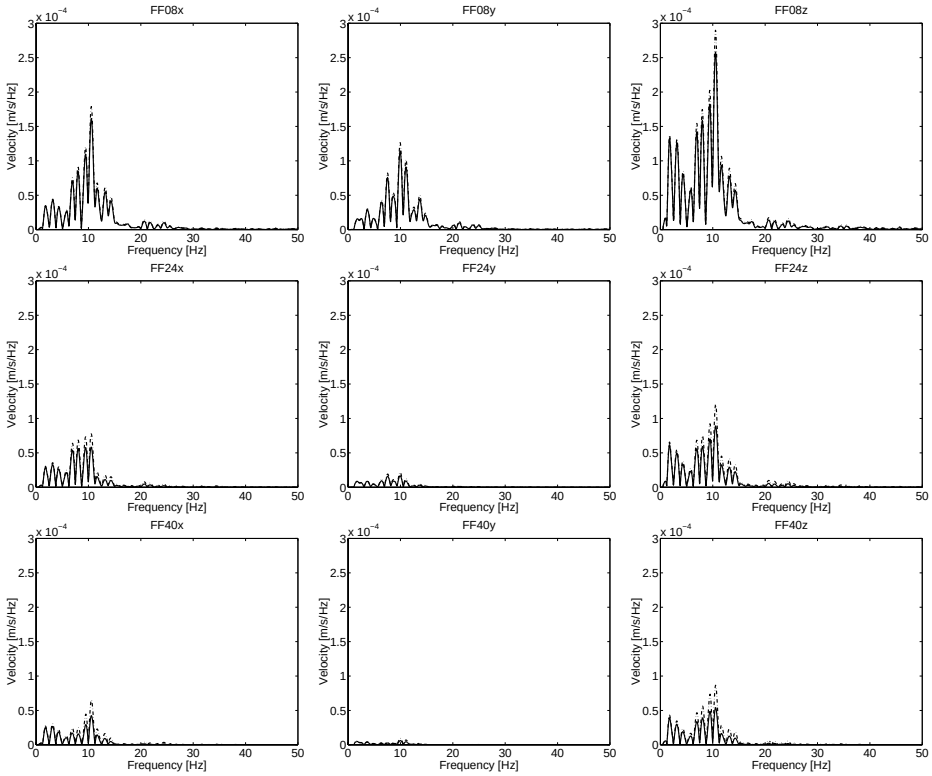


Figure 3.25: Frequency content of the free field velocity $\hat{v}_{si}(x, y = 0, z = 0, \omega)$ at a distance $x$, equal to 8, 24 and 40 m due to the passage of a Volvo FE7 truck on the traffic plateau with sine-shaped ramps for the case where the soil's hysteretic damping ratio $\beta$ equals 0.025 (dash-dotted line) and 0.050 (solid line).

Figure 3.25 shows that the contributions at high frequencies are relatively more affected by an increase of $\beta$. These results demonstrate that the soil's material damping has a large influence at large dimensionless distances, or distances that are large compared to the dominant wavelength in the soil.

### 3.5.7 The influence of the soil's stratification

In the following, the results of an extensive study [83] of the influence of the soil's stratification are briefly recapitulated. The free field vibrations generated by the passage of the Volvo FE7 truck on

the plateau with sine-shaped ramps, as in the previous examples, are calculated for three cases of the soil's stratification:

Case (a): a homogeneous halfspace with a density $\rho = 1800\,\mathrm{kg/m^3}$, a shear wave velocity $C_s = 150\,\mathrm{m/s}$, a dilatational wave velocity $C_p = 300\,\mathrm{m/s}$ and a hysteretic material damping ratio $\beta = 0.025$ in shear and volumetric deformation.

Case (b): a layer built in at its base with the material properties of the halfspace in case (a) and a thickness $d = 5\,\mathrm{m}$.

Case (c): a layer with the same material properties as the halfspace in case (a) and a thickness $d = 5\,\mathrm{m}$, supported by a halfspace with a density $\rho = 1800\,\mathrm{kg/m^3}$, a shear wave velocity $C_s = 300\,\mathrm{m/s}$ and a dilatational wave velocity $C_p = 600\,\mathrm{m/s}$.

The road has a width $2B = 3\,\mathrm{m}$; it is composed of a bituminous top layer, a granular subbase and a foundation (table 3.6). As the load is applied at the centre of the road ($x_S = 0$), only the road's bending deformations are accounted for. The following equivalent characteristics are used for the calculation of the road's impedance from equation (2.20): $EI = 1.63 \times 10^7\,\mathrm{Nm^2}$ and $\rho A = 2.44 \times 10^3\,\mathrm{kg/m}$.

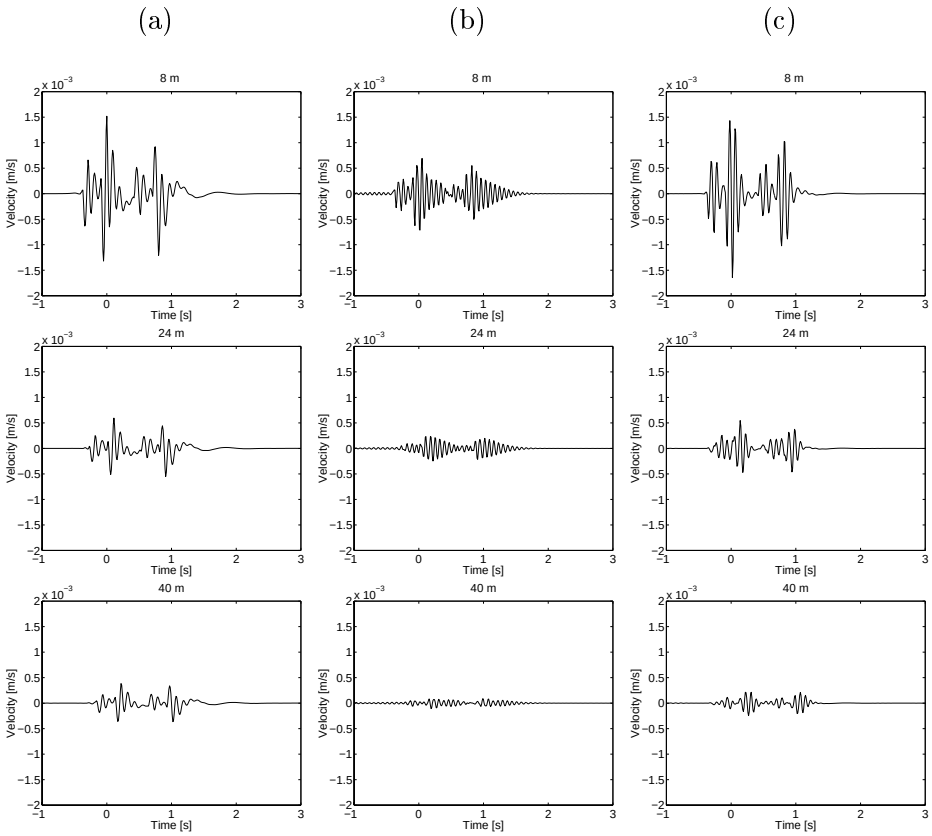


Figure 3.26: Time history of the vertical free field velocity $v_{sz}(x, y = 0, z = 0, t)$ at a distance $x$, equal to 8, 24 and 40 m due to the passage of a Volvo FE7 truck on a traffic plateau with sine-shaped ramps for a road supported by (a) a homogeneous halfspace, (b) a layer built in at its base and (c) a single layer on a halfspace.

Figures 3.26a and 3.27a show the time history and the frequency content of the vertical free field velocity at a distance of 8 m, 24 m and 40 m to the centre of the road for the case of the homogeneous

| layer | $d$ [m] | $E$ [$\times 10^6$ N/m$^2$] | $\nu$ [-] | $\rho$ [kg/m$^3$] |
|---|---|---|---|---|
| asphalt | 0.08 | 25000 | 0.3 | 2100 |
| granular | 0.17 | 500 | 0.5 | 2000 |
| foundation | 0.17 | 200 | 0.5 | 1800 |

Table 3.6: Road profile.

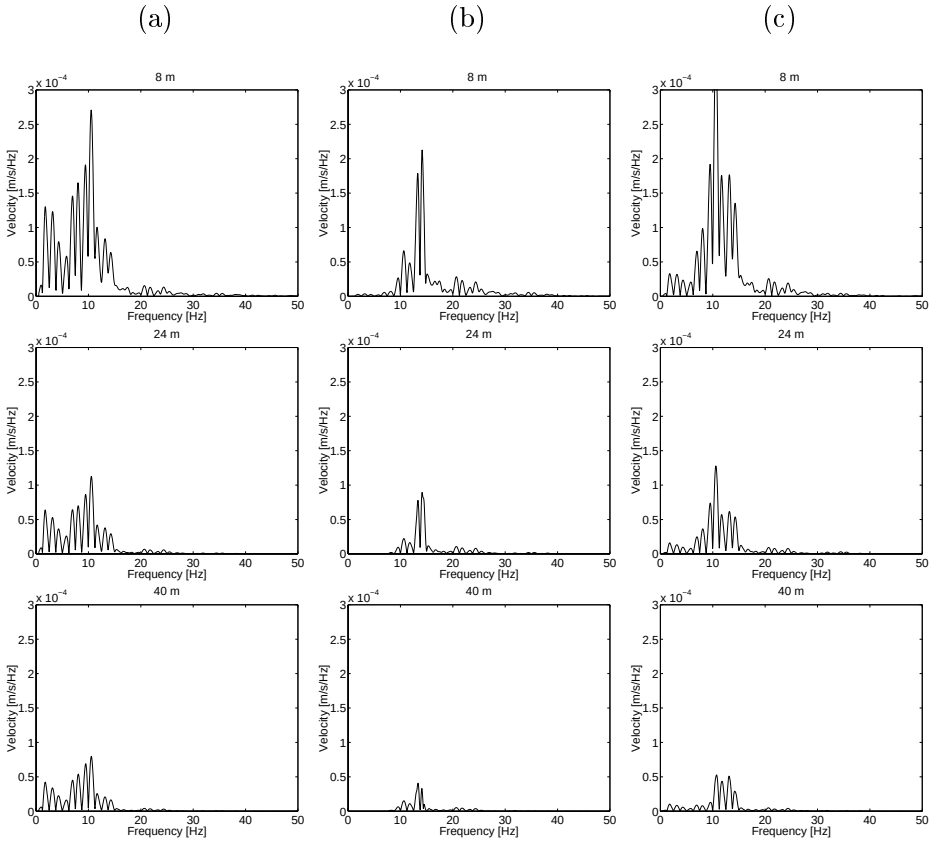


Figure 3.27: Frequency content of the vertical free field velocity $\hat{v}_{sz}(x, y = 0, z = 0, \omega)$ at a distance $x$, equal to 8, 24 and 40 m due to the passage of a Volvo FE7 truck on a traffic plateau with sine-shaped ramps for a road supported by (a) a homogeneous halfspace, (b) a layer built in at its base and (c) a single layer on a halfspace.

halfspace. When the time of arrival and the amplitude of the ground vibrations are compared, it can be observed that wave propagation in the soil delays and attenuates the signals for increasing distance to the source. The arrival time increases linearly for larger distances to the road. The frequency content of the ground vibrations is mainly situated below 20 Hz and is dominated by the pitch and bounce modes (at approximately 2 Hz) and the axle hop modes (between 9 Hz and 10 Hz) of the vehicle.

Figures 3.26b and 3.27b show the vertical free field velocity for the layer built in at its base. Compared to the case of the homogeneous halfspace, the PPV is smaller, while the resonance of the beam on top of the layer dominates the time history. The noise that appears in the time history before the vehicle mounts the traffic plateau at $t = -0.44$ s is due to an insufficiently small frequency resolution

$\Delta f$ for the calculation of the transfer function. A cut-off frequency appears near the first vertical eigenfrequency $C_p/4d = 15$ Hz of the layer built in at its base and dominates the frequency content. The soil exhibits the characteristics of a high-pass filter and the eigenfrequencies of the vehicle, which are situated below 10 Hz, are no longer observable. This phenomenon has also been observed by Al-Hunaidi and Rainer who suggested to shift the axle hop frequency of the buses in Montréal to a frequency that is below the cut-off frequency of the site in order to reduce the level of vibration nuisance [10].

Figures 3.26c and 3.27c show the vertical free field velocity for the case of the layer on a halfspace. The dispersive nature of the wave propagation in the layered halfspace is noticed when the arrival time is compared for the receivers at different distances from the source. At low frequencies, the wavelength is large and the frequency content of the response is lower than in the case of a homogeneous halfspace with the same material properties as the top layer. At frequencies higher than the first vertical eigenfrequency of the layer built in at its base, the frequency content of the free field velocity in cases (a) and (c) is very similar.

These results confirm that the predominant frequencies of traffic induced vibrations are determined by the vehicle characteristics, the unevenness profile and the soil stratification, as has been observed experimentally [10].

## 3.6 Conclusion

The presented parametric study allows to identify the key factors for the generation of free field traffic induced vibrations. Two groups of parameters are studied. The first group is related to the source mechanism of the vibrations and contains parameters that determine the road unevenness and the vehicle dynamics. A second group of parameters is related to the transmission of the vibrations and characterize the road and the soil. The results are compared to the vibration levels that are predicted by means of an empirical formula [1, 14].

The following conclusions can be drawn:

- A study of the longitudinal unevenness profile in the wavenumber domain reveals the relevant content within the range of wavenumbers $k_y$ between 2.5 rad/m and 12 rad/m or the range of wavelengths $\lambda_y = 2\pi/k_y$ between 0.5 m and 2.5 m that is of primary importance for the generation of traffic induced vibrations. In this range, the wavenumber content of a joint in the road surface with a limited height has the same order of magnitude as the profile of a traffic bump with a much larger height. The parameter study further shows that the height and the slope of the ramps are the predominant factors. The wavenumber content increases linearly with the height, while steep ramps result in a disadvantageous high wavenumber content. The shape of the ramps is only of secundary importance.

- An excitation of the axle hop modes is responsible for the generation of the free field vibrations in a frequency range between 8 Hz and 15 Hz. A study of the vehicle FRF shows that, more than the gross vehicle weight, the masses of the individual axles are important. Heavy vehicles will therefore generate, both in laden and unladen state, the largest vibrations. The stiffness of the tyres and the damping of the suspension system are the parameters that affect the FRF's in an equally important way.

- The free field vibrations generated by the passage of a vehicle on a traffic plateau and a joint in the road surface, respectively, have the same order of magnitude. The slope of the ramps of a traffic plateau has a dominant influence on the vibrations that are generated in the free field.

- Previous simulations show that, for the passage of a vehicle on a traffic plateau, the free field vibration levels can increase with a factor of 3 when the vehicle speed increases from 8 m/s to 20 m/s [64]. The vehicle speed has no large influence, however, on the vibrations that are generated during the passage on a joint in the road surface.
- The parameters that are related to the road section do not play an important role.
- For the receivers that are at a large dimensionless distance from the source, the soil's material damping is very important. For a homogeneous halfspace, the vibration levels are inversely proportional to the soil's stiffness. In the case where the soil is stratified, however, the nature of the stratification determines at which frequencies the response is attenuated or amplified. The dynamic soil properties have to be determined upto a sufficiently large depth in order to predict accurately the low frequency content of the response.
- Compared to the use of simple empirical models, an elaborated numerical model, that is based on the physical nature of the problem, has the advantage that it provides insight and allows to make predictions in the case where parameters as the shape of the unevenness, the soil's material damping and the soil's stratificiation are different.

# Chapter 4

# Experimental validation

## 4.1 Introduction

In the past ten years, a considerable effort has been made to develop numerical models for the prediction of traffic induced vibrations. Relatively few models, however, have been experimentally validated. The validation is complex due to the large number of parameters that are related to the source and the transmission path of the vibrations.

Within the frame of the present research project, an artificial unevenness has been developed for the experimental validation. The unevenness has been used for experiments at two sites. During these measurements both the vehicle and the free field response have been measured simultaneously. The measurement of the vehicle's response facilitates the interpretation of the field data, can be used to determine the dynamic vehicle characteristics and allows to check the accuracy of the vehicle's response predictions.

Figure 4.1: The passage of a DAF FT85 truck and trailer on the artificial unevenness at the DAF test circuit in Sint-Oedenrode (The Netherlands).

A first measurement campaign has been performed at the test circuit of the truck manufacturer DAF in Sint-Oedenrode (the Netherlands) [84]. With the cooperation of DAF, the truck and the free field

response have been measured simultaneously during the passage of a DAF FT 85 truck with trailer on the artificial profile (figure 4.1). A limited number of channels have been used for the measurement of the free field response. The experimental validation has demonstrated that the vehicle's speed and the dynamic soil characteristics have an important influence on the prediction of the free field vibrations and the experimental validation [85].

A more elaborate measurement campaign has been performed at the 'de Hemptinne site' of the Belgian Army in Heverlee (Belgium) within the frame of the 'OROS European University Millennium Award' project: "Vehicle response measurements as a validation tool for a prediction model for free field traffic induced vibrations" [86, 87]. The truck's response and the free field response have been measured during the passage of a Volvo FL6 truck on the artificial unevenness. Extensive tests have been performed to determine the parameters of the vehicle, the road and the soil.

In the following, only the results of the second measurement campaign are discussed. First, it is shown how the artificial unevenness has been designed. The experimental set-up is briefly recapitulated [88, 86]. Next, it is shown how the parameters that are used in the numerical model are determined. Finally, these parameters are used to validate the numerical model. Both the prediction of the vehicle's response and the free field vibrations are discussed.

## 4.2 Design of the experiment: the artificial unevenness

For the validation of the numerical model, measured and predicted free field vibrations are compared. In this case, it is advantageous to make use of a local, artificial unevenness for the generation of the free field vibrations. The passage of a vehicle on a local road unevenness generates a transient signal in the field that can be easily recognized and compared with the predicted signal. Furthermore, an artificial road unevenness with limited dimensions can be easily installed on a private road, avoiding problems related to the use of public roads for the experiments. Finally, the shape and the dimensions can be chosen freely [89]. For a particular site, vehicle and unevenness, the vehicle speed is the only parameter that can be varied within the experiments. The design is therefore based on the variation of the frequency content of the unevenness with the vehicle speed [89].

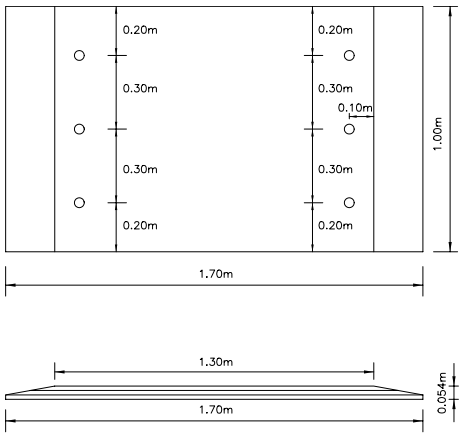


Figure 4.2: Top and side view of the artificial profile.

The artificial unevenness has the shape of a traffic plateau with straight ramps and is composed of two three-ply boards. Each board has a total height $H$ of 0.054 m, a flat top part with a length $L = 1.30$ m, slopes with a length $l = 0.20$ m and a width of 1 m (figure 4.2).

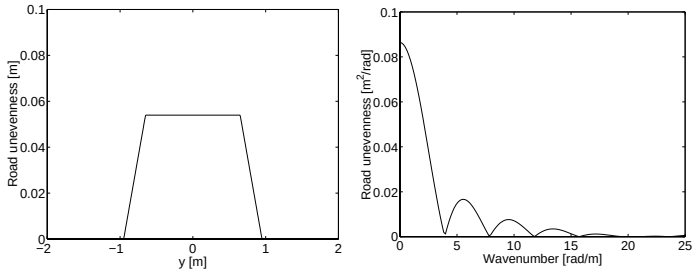


a. $u_{w/r}(y)$. b. $\tilde{u}_{w/r}(k_y)$.

Figure 4.3: The longitudinal profile of the artificial unevenness (a) as a function of the coordinate $y$ along the road and (b) in the wavenumber domain.

For the calculation of the vehicle's response, the bottom plate of the profile is assumed to have sloping ends, resulting in a length $l$ of 0.30 m for the slopes. The base length $L+2l$ now equals 1.90 m, while the mean length $L+l=1.60$ m. Figure 4.3a shows the longitudinal unevenness profile $u_{w/r}(y)$ as a function of the coordinate $y$ along the road. For the prediction of the free field response, the global road unevenness is neglected. Equation (3.4) is used to calculate the wavenumber content $\tilde{u}_{w/r}(k_y)$ of the artificial unevenness (figure 4.3b). The wavenumber content is mainly situated at wavenumbers $k_y$ below 20 rad/m or wavelengths $\lambda_y = 2\pi/k_y$ larger than 0.30 m. The separation between the lobes is inversely proportional to the mean length $L+l$ of the profile. The zero values correspond to $k_{yn}^0 = 2\pi n/(L+l)$, while local maxima occur at approximately $k_{yn}^{\max} = 3\pi n/(L+l)$

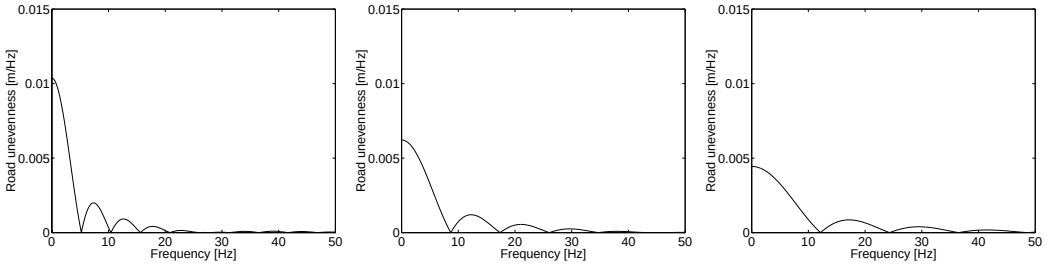


a. $v$= 30 km/h. b. $v$= 50 km/h. b. $v$= 70 km/h.

Figure 4.4: The unevenness experienced by the vehicle at a speed (a) $v = 30$ km/h, (b) $v = 50$ km/h and (c) $v = 70$ km/h.

The frequency content $\hat{u}_{w/r}(\omega)$ of the signal that is applied to the vehicle's axles is calculated from the representation in the wavenumber domain as $\tilde{u}_{w/r}(-\omega/v)/v$. For a fixed vehicle speed $v$, the contribution is zero at frequencies $f_n^0 = nv/(L+l)$. Local maximuma occur at $f_n^{\max} = 3nv/2(L+l)$. Figure 4.4 illustrates that, for increasing vehicle speeds, the quasi-static value of the signal decreases and the frequency content shifts to higher frequencies. In the frequency range where the axle hop frequencies are situated, there is a large variation of the signal, which will subsequently affect the frequency content of the axle loads.

## 4.3 The experimental configuration and data acquisition

The artificial unevenness has been installed on a road with a smooth asphalt surface at the 'de Hemptinne' site (figure 4.5) of the Belgian Army in Heverlee, using one three-ply board for each wheel path. The profile is fixed to the road with bolts and plugs. The response of the truck and the soil are


Figure 4.5: The profile installed at the test site.

measured during 26 passages of a Volvo FL6 truck on the artificial unevenness. The vehicle speed is varied with steps of 5 km/h from 25 km/h upto 60 km/h, with an average of 3 passages per vehicle speed. The data acquisition has been discussed in detail elsewhere [86]. In the following, only the elements that are essential for the validation are recapitulated.

### 4.3.1 The truck's response

The truck is a two-axle Volvo FL6 truck with a wheel base $w = 5.20$ m (figure 4.5). The truck has a leaf-spring suspension system at the front and the rear axle. The experimental configuration for the measurements of the vehicle response consists of 4 accelerometers and a mobile OROS OR25 PcPackII Model 304 data acquisition system, connected to a portable PC.

The accelerations of the truck are measured on the right hand side of the vehicle, at both the front and the rear part of the vehicle frame and on the vehicle's axles, using PCB accelerometers with a sensitivity of 0.1 V/g.

Figure 4.6 shows the accelerometers at the front part of the vehicle. The accelerometers are mounted on small steel plates, which are glued to the frame and the axles of the truck.

The A/D conversion is performed at a sampling rate $f_s = 512\,\text{Hz}$; the corresponding Nyquist frequency thus equals $f_{\text{Nyq}} = 256\,\text{Hz}$. An anti-aliasing filter with a low-pass frequency at 200 Hz is applied. 4 consecutive blocks of 1024 data points, corresponding to a period $T = 8\,\text{s}$, have been recorded for each vehicle passage. The resolution in the frequency domain equals $\Delta f = 0.125\,\text{Hz}$.

Preliminary test runs have shown a severe loss of contact between the rear axle and the road during the passage on the artifical unevenness. It was therefore decided to load the truck for the experiments. Although it was not observed on the site, the measurements still show a loss of contact between the rear axle of the loaded truck and the road. Furthermore, it was also observed that the quality of the data of the frame response was low [86]. As the dynamics of vehicle's axles, rather than the vehicle body, play a crucial role in the generation of ground vibrations, this was not considered to be problematic. The validation of the vehicle's response is therefore restricted to a comparison between the predicted and the measured axle response.

During the experiments, a GATSO 24 radar has been used by the Department of Environment and

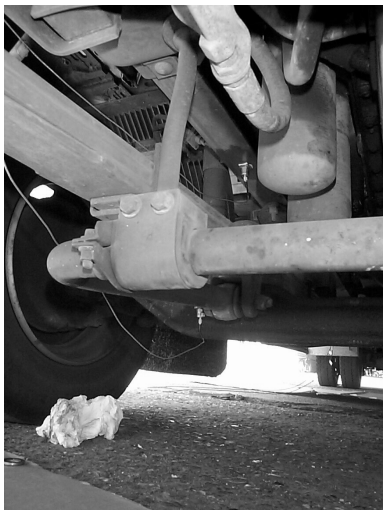

Figure 4.6: The accelerometers on the front part of the vehicle body and the front axle.

Infrastructure of the Ministry of the Flemish Community for the measurement of the vehicle speed. A comparison between the intended and the measured vehicle speed shows differences upto 3 km/h, which confirms the need for an independent measurement of the vehicle speed.

### 4.3.2 The soil's response

The experimental configuration for the measurement of the free field vibrations consists of 14 PCB seismic accelerometers, a KEMO VBF 35 unit and a 16 bit Daqbook 216 data-acquisition system, coupled to a portable PC.

The measurement line is situated perpendicular to the road (figure 4.7). For the definition of the measurement directions, a right-handed Cartesian frame of reference is chosen. The origin of the reference frame is located in the middle of the road, the $x$-axis is perpendicular to the road, the $y$-axis is parallel to the road and the $z$-axis is pointing upwards.

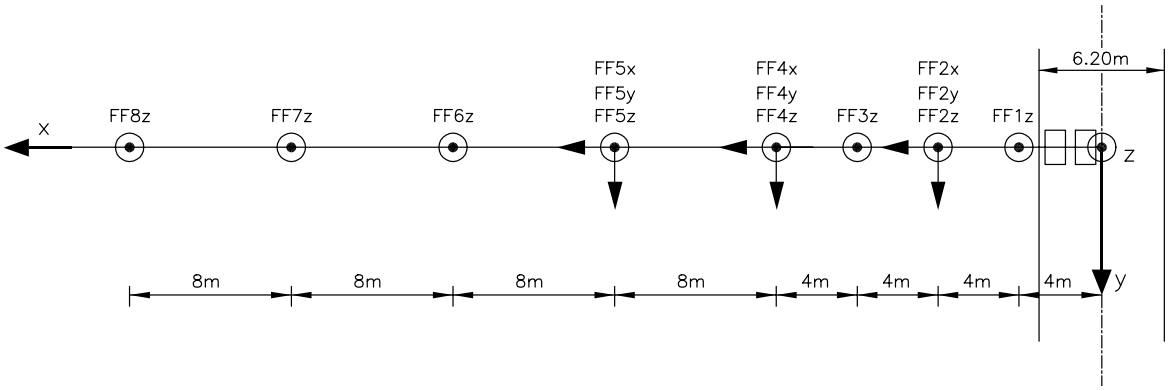


Figure 4.7: Position of the measurement line and the accelerometers.

The measurement points are located along the measurement line at a distance of 4 m, 8 m, 12 m, 16 m, 24 m, 32 m, 40 m and 48 m from the centre of the road. The vertical acceleration is measured in all

Figure 4.8: View from the end of the measurement line towards the road.

these points; at 8 m, 16 m and at 24 m, the horizontal accelerations in both directions are measured as well. Each accelerometer is mounted on a separate aluminium stake (figure 4.9) with a cruciform cross section to minimize dynamic soil-structure interaction.

Figure 4.9: The accelerometers FF2y, FF2z and FF2x (from left to right) mounted on aluminium stakes with a cruciform cross section.

The A/D conversion is performed within an amplitude range of $\pm 1.25$ V at a sampling rate $f_s = 500\,\mathrm{Hz}$; the corresponding Nyquist frequency thus equals $f_{\mathrm{Nyq}} = 250\,\mathrm{Hz}$. An anti-aliasing filter with a low-pass frequency at 125 Hz is applied. 4096 data points, corresponding to a period $T = 8.192\,\mathrm{s}$, have been

recorded for each vehicle passage. The resolution in the frequency domain equals $\Delta f = 0.122\,\text{Hz}$.

For each channel, the velocity is computed by an integration of the acceleration. A fourth order Chebyshev band-pass filter with a high-pass frequency $f_h = 2$ Hz and a low-pass frequency $f_l = 125$ Hz is employed. The high-pass frequency is used to remove the DC-component and to avoid drifting of the signal. The resulting signals are decimated by a factor of 2, reducing the sampling frequency from 500 Hz to 250 Hz and the Nyquist frequency from 250 Hz to 125 Hz.

## 4.4 The numerical prediction model

### 4.4.1 The vehicle model

The Volvo FL6 truck (figure 4.5) has been weighed in both empty and full loading state (table 4.1). The sum of the rear axle mass and the front axle mass is not equal to the total mass of the vehicle due to measurement errors.

| Truck loading state | Front axle mass [kg] | Rear axle mass [kg] | Total mass [kg] |
|---|---|---|---|
| Empty | 2880 | 3360 | 6220 |
| Laden | 2960 | 7000 | 10040 |

Table 4.1: Front axle mass, rear axle mass and total mass in empty and full loading state.

An unevenness that is present in both wheel paths mainly excites two sets of eigenmodes of the vehicle. The pitch and bounce modes have an eigenfrequency between 1 Hz and 3 Hz and involve an important motion of either the front or the rear part of the vehicle body. At higher frequencies between 8 Hz and 15 Hz, the axle hop modes dominate the vertical response of either the front or the rear axle. A peak-picking method is applied to estimate the pitch and bounce and the axle hop frequencies from the measured truck's response (table 4.2) [86].

Next, a stochastic subspace identification (SSI) method is applied to the measured data [90, 91]. This method fits an experimental model of a dynamic system through measured data. Figure 4.10 shows the stablization diagram, which contains the identified poles as a function of the experimental system order. The error criteria for stabilization are 1 % for frequencies, 2 % for damping ratios and 1 % for the participation vector correlations. This figure shows that, in the low frequency range, no stable poles are found; the pitch and bounce modes are not detected with the SSI method. In the frequency range between 10 Hz and 15 Hz, the axle hop modes are detected, although there is a large scatter on these data. For the passages at speeds higher than 35 km/h, the quality of the identification is even worse. The mean values for vehicle speeds between 25 km/h and 35 km/h are listed in table 4.2. The results from both methods correspond fairly well for the axle hop frequencies.

| | Peak-picking | SSI | 4DOF model |
|---|---|---|---|
| Axle hop front axle | 11.3 | 10.9 | 10.8 |
| Axle hop rear axle | 12.6 | 10.9 | 12.4 |
| Pitch and Bounce front | 1.8 | - | 1.9 |
| Pitch and Bounce rear | 1.6 | - | 1.4 |

Table 4.2: Estimated and predicted eigenfrequencies of the Volvo FL6 truck.

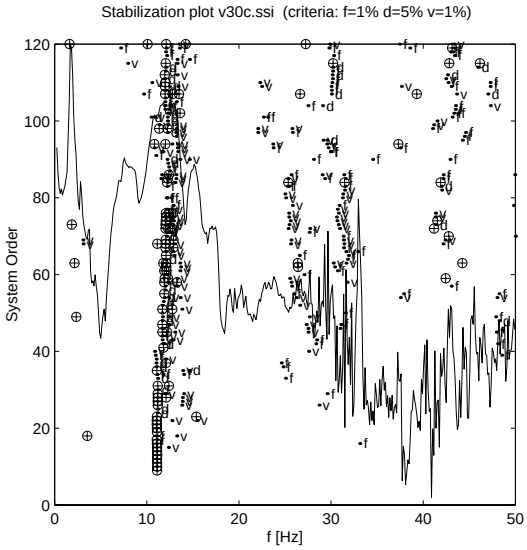


Figure 4.10: Stabilization diagram with the SSI method. The symbols in this diagram represent respectively: '⊕' a stable pole; '.v' a pole with a stable frequency and vector; '.d' a pole with a stable frequency and damping; '.f' a pole with a stable frequency and '.' a new pole.

In the following, a 2D 4DOF linear vehicle model (figure 2.1) is used to predict the dynamic axle loads. The vehicle body and the vehicle's axles are modelled as rigid inertial elements. The suspension system and the tyres are represented by linear spring damper connections. Non-linear effects as the loss of contact between the vehicle and the road and non-linear suspension characteristics are not incorporated. The parameters of the vehicle model are determined by means of the truck weighings (table 4.1), data provided by the truck manufacturer and a fit of the measured and calculated response.

| Vehicle characteristics | |
|---|---|
| $m_{a1}$ | 600 kg |
| $m_{a2}$ | 400 kg |
| $k_{p1}$ | $0.34 - 0.61 \times 10^6$ N/m |
| $k_{p2}$ | $0.32 \times 10^6$ N/m |
| $k_{t1}$ | $2.68 - 3.00 \times 10^6$ N/m |
| $k_{t2}$ | $1.34 - 1.50 \times 10^6$ N/m |

Table 4.3: Vehicle data provided by the truck manufacturer for the Volvo FL6 truck.

The truck manufacturer has provided data for the rear axle mass $m_{a1}$ and the front axle mass $m_{a2}$, as well as a range of values for the spring constants $k_{p1}$ and $k_{p2}$ of the suspension system and the spring constants $k_{t1}$ and $k_{t2}$ of the tyres (table 4.3). The mass $m_b$ and the position of the centre of gravity of the vehicle are calculated from the total mass (table 4.1) and the axle's masses.

The rotational inertia $I_b$ and the values for $k_{p1}$, $k_{t1}$ and $k_{t2}$ are used to tune the eigenfrequencies of the 4DOF model to the identified values. The stiffness coefficients are equal to the maximum values within the range specified in table 4.3. The measured and the calculated eigenfrequencies agree well (table 4.2).

The damping coefficients $c_{t1}$ and $c_{t2}$ of the rear and the front tyre are assumed to be zero. The

damping coefficients $c_{p1}$ and $c_{p2}$ of the front and rear suspension system are estimated through a fit of the predicted and measured frequency content of the response at the axle hop frequencies for a vehicle speed $v = 30\,\mathrm{km/h}$. This relatively low vehicle speed has been chosen as the influence of the loss of contact on the response increases for higher vehicle speeds.

The following values are found for the parameters of the 4DOF Volvo FL6 vehicle model: $m_b = 9000\,\mathrm{kg}$, $I_b = 35000\,\mathrm{kgm^2}$, $m_{a1} = 600\,\mathrm{kg}$, $m_{a2} = 400\,\mathrm{kg}$, $l_1 = -1.49\,\mathrm{m}$, $l_2 = 3.72\,\mathrm{m}$, $k_{p1} = 0.61 \times 10^6\,\mathrm{N/m}$, $k_{p2} = 0.32 \times 10^6\,\mathrm{N/m}$, $k_{t1} = 3.00 \times 10^6\,\mathrm{N/m}$, $k_{t2} = 1.50 \times 10^6\,\mathrm{N/m}$, $c_{p1} = 16000\,\mathrm{Ns/m}$, $c_{p2} = 10050\,\mathrm{Ns/m}$, $c_{t1} = 0\,\mathrm{Ns/m}$ and $c_{t2} = 0\,\mathrm{Ns/m}$.

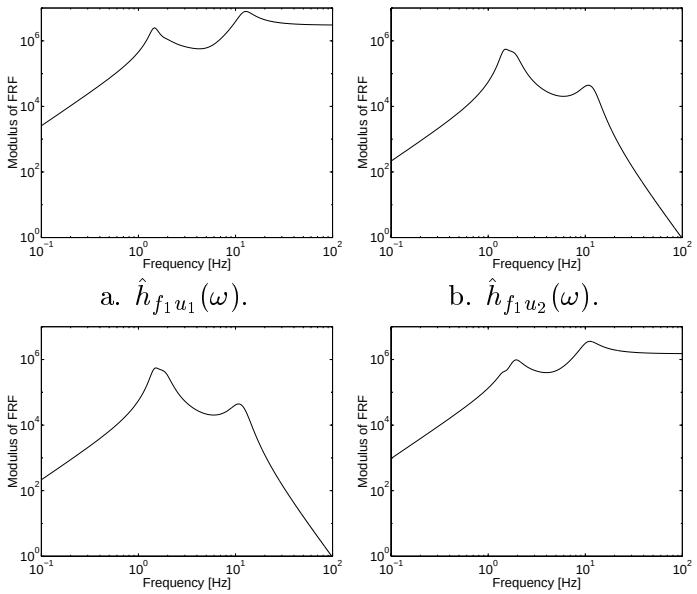


a. $\hat{h}_{f_1 u_1}(\omega)$. b. $\hat{h}_{f_1 u_2}(\omega)$.

d. $\hat{h}_{f_2 u_1}(\omega)$. e. $\hat{h}_{f_2 u_2}(\omega)$.

Figure 4.11: Modulus of the FRF $\hat{h}_{f_k u_l}(\omega)$ for the 2D 4 DOF vehicle model of the Volvo FL6 truck.

Figure 4.11 shows the modulus of the frequency response functions (FRF) $\hat{h}_{f_k u_l}(\omega)$ of the vehicle model. The functions $\hat{h}_{f_k u_k}(\omega)$ represent the frequency content of the axle load at axle $k$ for an impulse excitation at the same axle. A maximum is obtained at the axle hop frequency. The FRF $\hat{h}_{f_k u_k}(\omega)$ have a larger amplitude than the FRF $\hat{h}_{f_k u_l}(\omega)$ for an excitation at a different axle $l$. The latter have a maximum at the pitch and bounce mode.

### 4.4.2 The road model

The road has a total width $2B = 6.20\,\mathrm{m}$ and is composed of two asphalt top layers and a foundation that is composed of a crushed stone layer and a crushed concrete layer. Table 4.4 presents the road profile as it has been designed. The asphalt layers have a total thickness of 0.11 m, while the road foundation has a total thickness of 0.44 m.

In December 2000, the Laboratory of Soil Mechanics of Ghent University has applied a spectral analysis of surface waves (SASW) test to determine the road's stratification and the dynamic road characteristics [92]. A hammer impact is used to generate surface waves in the road. The response is measured with two geophones in a common mid-point configuration (figure 4.12). The distance between both geophones is equal to the distance between the first geophone and the source. In four different set-ups, the response is measured with the first geophone at a distance of 0.10 m, 0.20 m, 0.40

| layer | type | $d$ [m] |
|---|---|---|
| 1 | asphalt Ia | 0.05 |
| 2 | asphalt IIIa | 0.06 |
| 3 | crushed stone | 0.19 |
| 4 | crushed concrete | 0.25 |

Table 4.4: Road section.

m and 0.80 m from the source. Nazarian's method is applied to determine the experimental dispersion points.

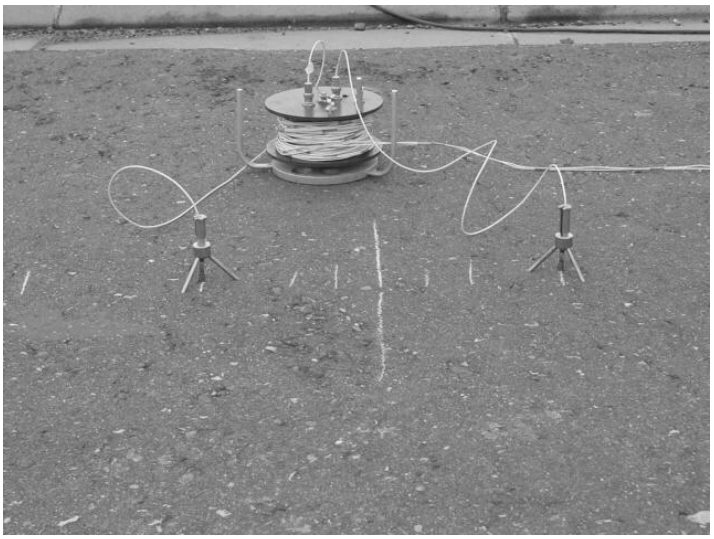

Figure 4.12: Experimental configuration with two geophones in a common mid-point configuration with a distance of 0.80 m between the geophones.

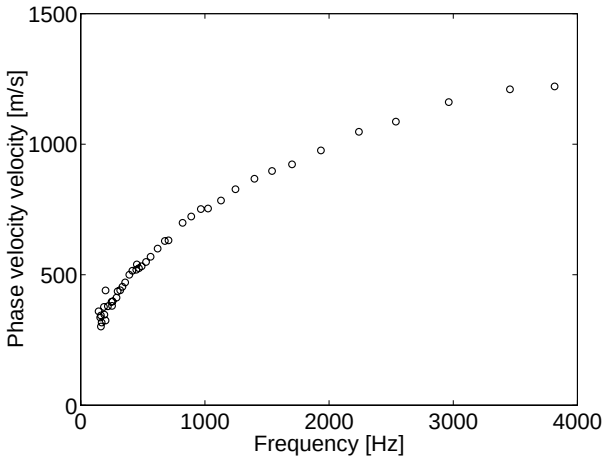


Figure 4.13: The experimental dispersion points as obtained by the SASW test on the road.

Figure 4.13 shows the mean values of the experimental dispersion points. In an inversion procedure, the difference between the experimental and theoretical dispersion curve of the first surface wave is

minimized. For the calculation of the theoretical dispersion curve, the road is modelled as a horizontally layered, linear elastic halfspace. Each layer is characterized by its thickness $d$, the modulus of Young $E$, the Poisson's ratio $\nu$ and the density $\rho$. As the inversion procedure is relatively insensitive to the values of the density $\rho$ and the Poisson's ratio $\nu$, these values are not changed in the inversion procedure.

An inversion procedure with the profile of a single layer on a halfspace reveals the presence of a stiff layer with a thickness of 0.15 m and a shear wave velocity $C_s = 1600$ m/s on top of a halfspace with a shear wave velocity $C_s = 250$ m/s [92]. An inversion procedure with more layers on top of a halfspace does not result in a refinement of this profile. The characteristics of the halfspace are therefore also influenced by the presence of the road's foundation under the asphalt top layer. The results indicate that the thickness of the asphalt layer is approximately 0.15 m instead of 0.11 m. For an estimated asphalt density $\rho = 2100\,\mathrm{kg/m^3}$ and a Poisson's ratio $\nu = 1/3$, the Young's modulus equals $E = 14340 \times 10^6\ \mathrm{N/m^2}$. The Young's modulus of asphalt is very sensitive to the temperature however. During the free field vibration measurements in June, the temparature was about 20 °C, while during the SASW test in December, the temparature was 5 °C. An approximating relation $E = 10^{(a+bT)}$ [93], with $b = -0.013$, is used, resulting in an estimate $E = 9150 \times 10^6\ \mathrm{N/m^2}$ at a temparature of 20 °C. This corresponds well with values that are reported in literature for the modulus of Young of asphalt during spring and summer [94]. The dynamic characteristics of the road's foundation are estimated [94]. These values are insensitive for the temperature.

| layer | type | $d$ [m] | $\nu$ [-] | $\rho$ [kg/m$^3$] | $E$ [$\times 10^6$ N/m$^2$] |
|---|---|---|---|---|---|
| 1 | asphalt | 0.15 | 1/3 | 2100 | 9150 |
| 2 | crushed stone | 0.19 | 1/2 | 2000 | 500 |
| 3 | crushed concrete | 0.25 | 1/2 | 1800 | 200 |

Table 4.5: The theoretical road profile.

Table 4.5 summarizes the layer thickness $d$, the Poisson's ratio $\nu$, the density $\rho$ and the Young's modulus $E$. The value of the Poisson's ratio for the crushed stone and concrete layer corresponds to the value of an incompressible material. This choice is relatively unimportant, however, as in the numerical model, the road is not modelled as a continuum, but as a beam with a rigid cross section. The equivalent characteristics are calculated as in appendix A: $EI = 7.83 \times 10^7\ \mathrm{Nm^2}$, $\rho A = 7099\,\mathrm{kg/m}$, $\rho I_p = 2.33 \times 10^4\,\mathrm{kgm}$ and $GC = 3.08 \times 10^7\ \mathrm{Nm^2}$.

### 4.4.3 The soil model

The soil at the 'de Hemptinne' test site is mainly composed of loam. An artificially filled up top layer with a thickness of 0.30 m is present. Both a spectral analysis of surface waves (SASW) test and a seismic cone penetration test (SCPT) have been performed to determine the soil's stratification and the dynamic soil characteristics. The results of the SASW test reveal the dynamic characteristics of the upper soil layers, whereas the results of the SCPT provide information at larger depths.

In June 2000, a SASW test has been performed [88]. A transient excitation is generated with a falling weight device (FWD), where a mass of 110 kg is dropped from a height of 0.9 m on a square ($0.7\,\mathrm{m} \times 0.7\,\mathrm{m}$) steel foundation with a mass of 600 kg. A dashpot is used to control the frequency content of the loading and to prevent rebound of the mass. The vertical response is measured in 10 points at the surface at a distance from 2 m to 48 m from the source. Next, Nazarian's method [95, 96] is used to determine the experimental dispersion curve, through which a fifth order polynomial is fitted (figure 4.14).

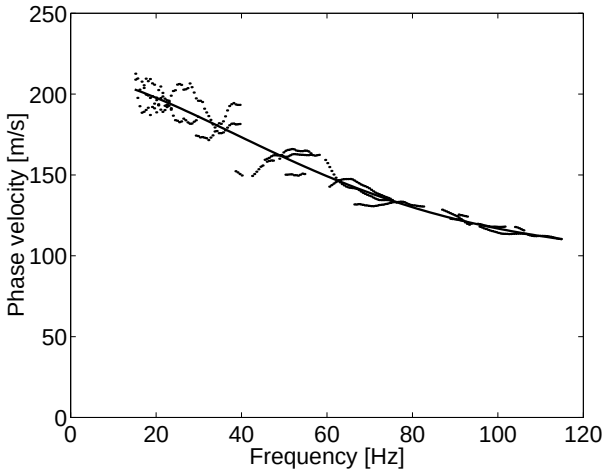


Figure 4.14: The experimental dispersion points and the experimental dispersion curve.

The inversion procedure minimizes the difference between the experimental and theoretical dispersion curve of the first surface wave. For the calculation of the theoretical dispersion curve [97] the soil is modelled as a horizontally layered, linear elastic halfspace. Each layer is characterized by its thickness $d$, the modulus of Young $E$, the Poisson's ratio $\nu$, the density $\rho$ and the material damping ratios $\beta_s$ and $\beta_p$ for the shear and the longitudinal waves, respectively. As the inversion procedure is relatively insensitive to the values of the density $\rho$, the Poisson's ratio $\nu$ and the material damping ratios $\beta_s$ and $\beta_p$, these values are estimated from experience as: $\rho = 1650\,\mathrm{kg/m^3}$, $\nu = 0.33$ and $\beta_s = \beta_p = 0.005$ and remain constant in the inversion procedure. The inversion procedure is performed with an increasing number of layers on top of a halfspace. For the case of two or more layers, the deviation between the experimental and the theoretical dispersion curve is no longer observable.

| layer | $d$ [m] | $C_s$ [m/s] |
|---|---|---|
| 1 | 0.46 | 106 |
| 2 | 0.67 | 162 |
| 3 | 1.35 | 210 |
| 4 | $\infty$ | 234 |

Table 4.6: Final profile after an inversion procedure with 3 layers on a halfspace.

Table 4.6 shows the results of the inversion procedure for the case where 3 layers on a halfspace are used to represent the soil profile. The soil's stiffness or the shear wave velocity $C_s$ increases with the depth $z$. For a larger number of layers in the inversion procedure, the increase with the depth $z$ is more detailed [88].

In December 2000, a SCPT has been performed by the Laboratory of Soil Mechanics of Ghent University at this site to determine the dynamic soil characteristics [92]. An electrical cone is equipped with a seismic module that includes two triaxial geophones at a distance of 1 m (figure 4.15). Each time the cone is driven 0.5 m deeper into the soil, both a horizontal and a vertical impact are generated at the soil's surface. The shear wave velocity is estimated from the time delay between the response at the geophones for the horizontal impact, while the longitudinal wave velocity is estimated from the response for the vertical impact. The SCPT has been performed on the measurement line, at a distance of 12 m and 36 m from the road's axis. Due to technical problems, only the results of the

Figure 4.15: The cone and the hydraulic press.

first SCPT are reliable. At both locations, a stiff layer at a depth of 8.20 m could not be penetrated.

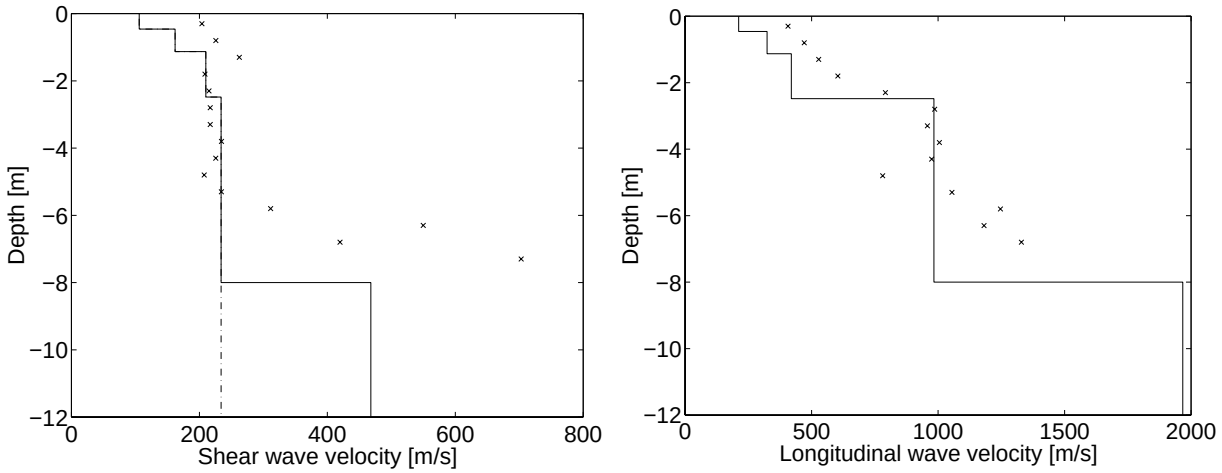


a. Shear wave velocity.

b. Longitudinal wave velocity.

Figure 4.16: (a) The shear wave velocity profile as determined by means of the SASW method (dash-dotted line), the SCPT method (crosses) and the theoretical profile (solid line) and (b) the longitudinal wave velocity profile as determined by means of the SCPT method (crosses) and the theoretical profile (solid line). On figure (a), the results of the SASW test and the theoretical profile coincide upto a depth of 8.20 m.

Figure 4.16a shows, on the same graph, the shear wave velocity profile as obtained with the SASW test and the SCPT. At intermediate depths, the results correspond well. The results of the SASW test are more detailed at the soil's surface, while the results of the SCPT indicate the presence of a stiff

layer at a depth of 8.20 m. The higher shear wave velocities at smaller depths are probably due to wave refraction. Figure 4.16b shows the longitudinal wave velocity profile as obtained with the SCPT. The relation between the shear wave velocity and the longitudinal wave velocity allows to estimate the Poisson's ratio. For the top layers, a Poisson's ratio of 1/3 is found, while at a depth larger than 2.3 m, it is equal to 0.47. This high value reveals the presence of ground water.

The theoretical shear wave velocity follows the results of the SASW test for the top layers (figure 4.16a). At a depth of 8.20 m, a layer with a stiffness that is arbitrarily taken as four times the stiffness of the fourth layer is introduced. The SCPT results are followed for the determination of the Poisson's ratio of the theoretical soil profile (figure 4.16b). The soil's density $\rho$ is estimated as $1900\,\mathrm{kg/m^3}$ for dry loam and $2000\,\mathrm{kg/m^3}$ for the saturated loam layers.

| layer | $d$ | $\nu$ | $\rho$ | $E$ | $C_s$ | $C_p$ | $\beta$ |
|---|---|---|---|---|---|---|---|
| | [m] | [-] | [kg/m$^3$] | [$\times 10^6$ N/m$^2$] | [m/s] | [m/s] | [-] |
| 1 | 0.46 | 1/3 | 1900 | 57 | 106 | 212 | 0.0500 |
| 2 | 0.67 | 1/3 | 1900 | 133 | 162 | 324 | 0.0375 |
| 3 | 1.35 | 1/3 | 1900 | 223 | 210 | 420 | 0.0250 |
| 4 | 5.72 | 0.47 | 2000 | 322 | 234 | 984 | 0.0250 |
| 5 | $\infty$ | 0.47 | 2000 | 1288 | 468 | 1968 | 0.0250 |

Table 4.7: The theoretical soil profile.

Table 4.7 summarizes the layer thickness $d$, the Poisson's ratio $\nu$, the density $\rho$ and the Young's modulus $E$. The hysteretic material damping ratio $\beta$ has a large influence on the response at distances from the source that are large with respect to the dominant wavelength in the soil. However, it has not been included in the inversion process for the determination of the soil characteristics from the SASW data. The material damping is estimated as 0.050 for the first layer, 0.0375 for the second layer and 0.025 for the deeper layers. This agrees with the experimental observation that material damping decreases with depth. Within the frame of a research project in cooperation with the Laboratory of Soil Mechanics of Ghent University, the estimation of the material damping from geophysical tests as the SASW and the SCPT is presently studied.

## 4.5 The validation of the vehicle's response

### 4.5.1 The predicted axle loads

Figures 4.17 and 4.18 illustrate the prediction of the front axle load at a vehicle speed $v$ equal to 30 km/h and 58 km/h, respectively. A time scale is chosen where the time $t = 0$ corresponds to the time at which the front axle of the vehicle is located at the middle of the profile.

Figures 4.17a and 4.18a show the frequency content $\hat{u}_{w/r}(\omega)$ of the unevenness as it is experienced by the rear axle. As has been shown in figure 4.4, the frequency content shifts to higher frequencies while the quasi-static value decreases for an increasing vehicle speed $v$. Figures 4.17b and 4.18b represent the FRF $\hat{h}_{f_2 u}(\omega)$ for the front axle load. Figures 4.17c and 4.18c show the frequency content $\hat{g}_2(\omega)$ of the front axle load, which is obtained as the product of the frequency content of the experienced unevenness $\hat{u}_{w/r}(\omega)$ and the FRF $\hat{h}_{f_2 u}(\omega)$. Whereas the frequency content of the axle load is mainly situated below 30 Hz for a vehicle speed of 30 km/h, this upper limit shifts to 60 Hz for a vehicle speed of 58 km/h. The dominant frequency, however, remains approximately constant and is mainly determined by the axle hop frequency of the rear axle. The contribution at the pitch and bounce frequencies is relatively small.

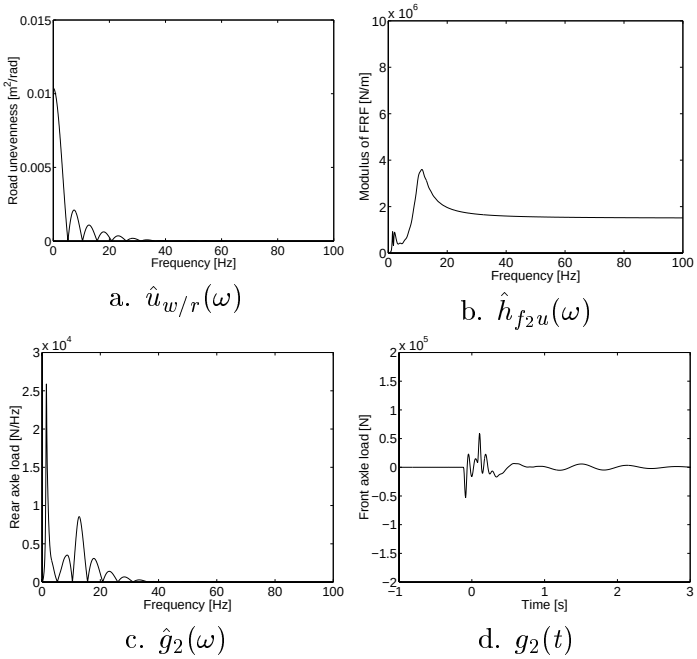


a. $\hat{u}_{w/r}(\omega)$ b. $\hat{h}_{f_2u}(\omega)$

c. $\hat{g}_2(\omega)$ d. $g_2(t)$

Figure 4.17: (a) Frequency content $\hat{u}_{w/r}(\omega)$ of the experienced unevenness, (b) FRF $\hat{h}_{f_2u}(\omega)$, (c) frequency content $\hat{g}_2(\omega)$ and (d) time history $g_2(t)$ of the predicted front axle load for a passage of the Volvo FL6 truck on the artificial profile at a vehicle speed $v = 30$ km/h.

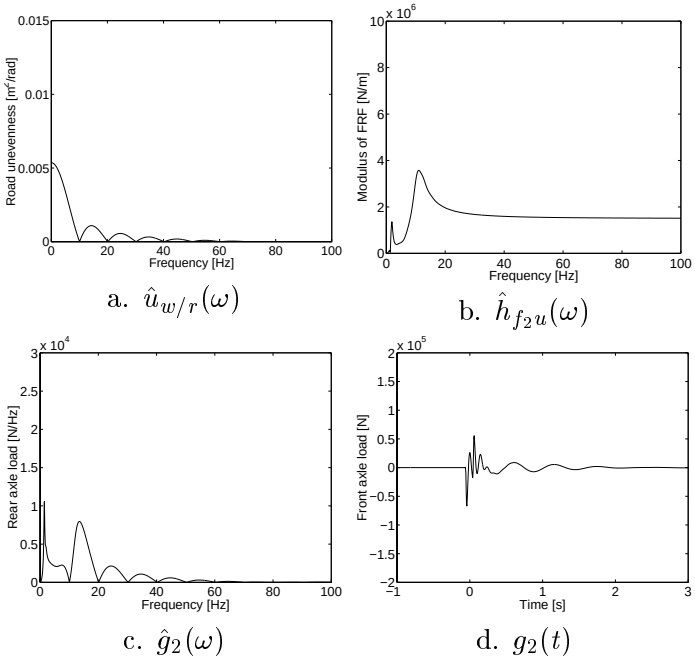


a. $\hat{u}_{w/r}(\omega)$ b. $\hat{h}_{f_2u}(\omega)$

c. $\hat{g}_2(\omega)$ d. $g_2(t)$

Figure 4.18: (a) Frequency content $\hat{u}_{w/r}(\omega)$ of the experienced unevenness, (b) FRF $\hat{h}_{f_2u}(\omega)$, (c) frequency content $\hat{g}_2(\omega)$ and (d) time history $g_2(t)$ of the predicted front axle load for a passage of the Volvo FL6 truck on the artificial profile at a vehicle speed $v = 58$ km/h.

Figures 4.17d and 4.18d finally show the time history $g_2(t)$ of the front axle load, which is obtained through an inverse FFT. The duration of the signal can be estimated from the mean length $L+l = 1.60$

m of the profile, the wheel base $w = 5.20$ m of the truck and the vehicle speed $v$. At a speed $v = 30$ km/h, a transient signal with a duration of 0.82 s is expected. At a time $t = -0.10$ s, the front axle ascends the profile, while at $t = 0.10$, the front axle descends. At $t = 0.53$ s and $t = 0.72$ s, the ascending and descending of the rear axle can hardly be observed, which illustrates that the interaction between the axles is small. After the passage of the axle on the profile, a free vibration at the pitch and bounce frequency is observed. At a speed $v = 58$ km/h, the time delay between the ascending and the descending is only 0.10 s. The peak axle load increases slightly for higher vehicle speeds. Analogous conclusions can be drawn from the results for the rear axle load.

### 4.5.2 Time history and frequency content of the axles' response

In the following, the accelerations of the axles are referred to by a label TIAz, where the character I indicates the location of the accelerometer at the front (F) or the rear (R) part of the truck. The characters A and z indicate that the acceleration of the axle in the vertical direction is considered.

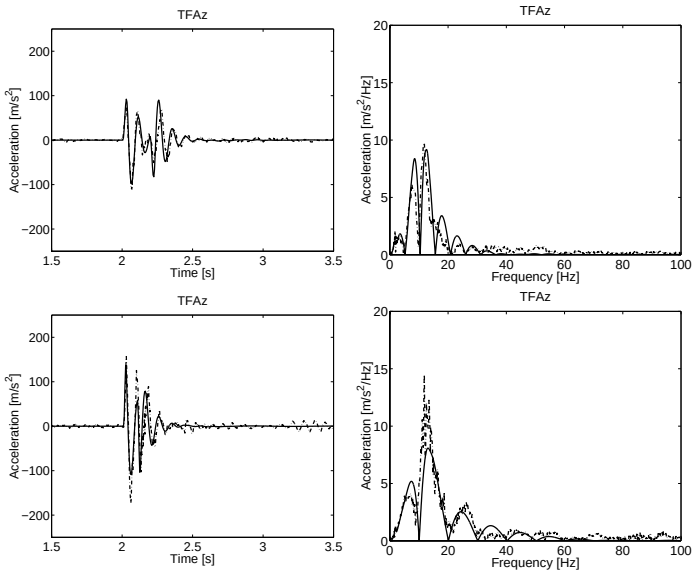


Figure 4.19: Predicted (solid line) and measured (dash-dotted line) time history (left hand side) and frequency content (right hand side) of the acceleration of the front axle for vehicle speeds $v = 30\,\mathrm{km/h}$ (top) and $v = 58\,\mathrm{km/h}$ (bottom).

Figure 4.19 shows the time history and the frequency content of the predicted and the measured accelerations of the front axle for vehicle speeds of 30 km/h and 58 km/h. Compared to figures 4.17 and 4.18, a time shift has been applied to the predicted results to plot both signals on the same horizontal time scale.

The time between the ascending and descending of one axle on the profile decreases from 0.19 s for a vehicle speed $v$ of 30 km/h to 0.10 s for $v = 58$ km/h. The impact at the ascending and descending is only visible at the lowest vehicle speed. After the axle descends the profile, a free vibration at the axle hop frequency occurs. The duration of the transient signal is well predicted, whereas the peak acceleration is underestimated. The underestimation increases with the vehicle speed $v$. The frequency content of both the predicted and the measured acceleration is dominated by the axle hop frequencies and shifts to higher frequencies for an increasing vehicle speed. As the parameters of the 2D vehicle model have been tuned using the vehicle's response at a speed of 30 km/h, it is not surprising that the axle's response at this vehicle speed is very well predicted. At higher vehicle speeds, the contribution

at the axle hop frequency is underestimated.

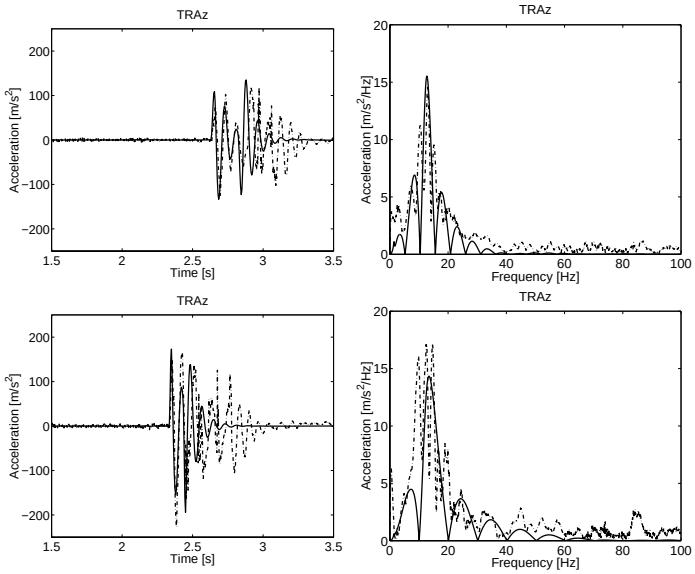


Figure 4.20: Predicted (solid line) and measured (dash-dotted line) time history (left hand side) and frequency content (right hand side) of the acceleration of the rear axle for vehicle speeds $v = 30\,\mathrm{km/h}$ (top) and $v = 58\,\mathrm{km/h}$ (bottom).

Figure 4.20 shows the time history and the frequency content of the predicted and the measured accelerations of the rear axle for vehicle speeds of 30 km/h and 58 km/h. The quality of the prediction is worse than for the front axle. Although the peak accelerations correspond well, there is a clear difference between the duration of the predicted and the measured transient acceleration signal. This confirms the experimental observation that there is a loss of contact between the rear axle and the artificial profile, that is followed by an impact when the axle touches the road [98]. This phenomenon is not taken into account by the present linear vehicle model. As a result, the lobes that correspond to the frequency content of the unevenness signal are not present in the frequency content of the measured axle load. At higher vehicle speeds, this results in an important difference between the predicted and the measured axle load at approximately 10 Hz. Furthermore, it is found that the contribution at low and high frequencies is underestimated.

### 4.5.3 Peak acceleration of the axles' response

Figure 4.21a shows the measured and predicted peak acceleration of the truck's front axle as a function of the vehicle speed. At low vehicle speeds, the correspondence between the predicted and the measured peak acceleration is relatively good. At higher vehicle speeds, the peak acceleration of the front axle is underestimated.

For an increasing vehicle speed $v$, the frequencies $f_n^0 = nv/(L+l)$ and $f_n^{\max} = 3nv/2(L+l)$, that characterize the zeros and the local maxima of the unevenness signal (figures 4.17a and 4.18a), shift to higher frequencies. As a result, the location of these frequencies changes with respect to the axle hop frequency of the front axle at 10.8 Hz. For a vehicle speed $v = 31.1$ km/h, the axle hop frequency equals the second zero $f_2^0$. As the vehicle speed increases to 41.5 km/h, the first local maximum $f_1^{\max}$ of the experienced unevenness approaches the axle hop frequency and the peak acceleration increases. For a vehicle speed between 41.5 km/h and 62.2 km/h, the axle hop frequency is situated between $f_1^{\max}$ and $f_1^0$ and the peak acceleration does not increase with the vehicle speed. The contribution at

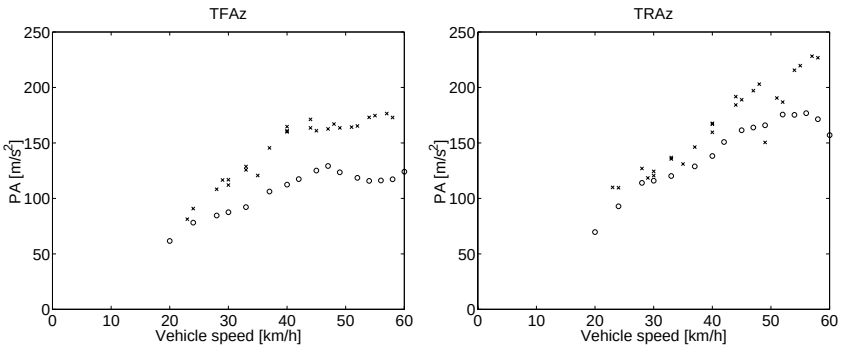


a. Peak acceleration front axle. b. Peak acceleration rear axle.

Figure 4.21: Predicted (circles) and measured (crosses) peak axle acceleration of (a) the front axle and (b) the rear axle as a function of the vehicle speed.

other frequencies should, off course, be considered as well and the trend with increasing vehicle speed is more complex. It indicates, however, how the influence of the vehicle speed depends on the dynamic characteristics of the vehicle and the longitudinal unevenness profile.

Figure 4.21b shows the measured and predicted peak acceleration of the truck's rear axle as a function of the vehicle speed. Although the loss of contact is not predicted, there is a good agreement between the predicted and the measured peak acceleration of the rear axle. For a vehicle speed of 35.7 km/h, the axle hop frequency of the rear axle at 12.4 Hz coincides with the frequency $f_2^0$. As the vehicle speed increases to 47 km/h, $f_1^{\max}$ tends to the axle hop frequency and the peak acceleration increases. For a vehicle speed between 47 km/h and 71 km/h, the axle hop frequency is situated between $f_1^{\max}$ and $f_1^0$ and the peak acceleration is not expected to increase with the vehicle speed. This trend, however, cannot be detected in the variation of the measured peak acceleration with the vehicle speed. This is due to the fact that the rear axle does not follow the unevenness. As a result, the frequency content of the rear axle's acceleration (figure 4.20) does not show lobes with zeros $f_n^0$ and $f_n^{\max}$ similar as for the unevenness (figure 4.19a).

## 4.6 The validation of the soil's response

### 4.6.1 The road-soil interaction problem

The total thickness of the road roughly corresponds to the thickness of the top layer of the soil profile (table 4.7). As in the numerical model the road is assumed to be located at the soil's surface, the influence of the top layer is discarded for the calculation of the soil's impedance. The boundary element method is therefore based on the Green's functions for a vertical impulse load at the surface of a halfspace composed of the layers 2 to 5 of the soil profile in table 4.7. This case is referred to as model 1 (figure 4.22a).

The transfer functions between the road and a point in the free field are calculated from the soil's tractions and the Green's functions. The receivers in the free field are located at the surface of the weak top layer. If the Green's functions of the soil model 1 are used for the calculation of the transfer functions, the presence of the weak top layer is neglected and it is expected that the vibration levels in the free field are underestimated.

In order to estimate the influence of the weak top layer on the free field response, the Green's functions in the first case are compared with the Green's functions for a vertical impulse load at the interface

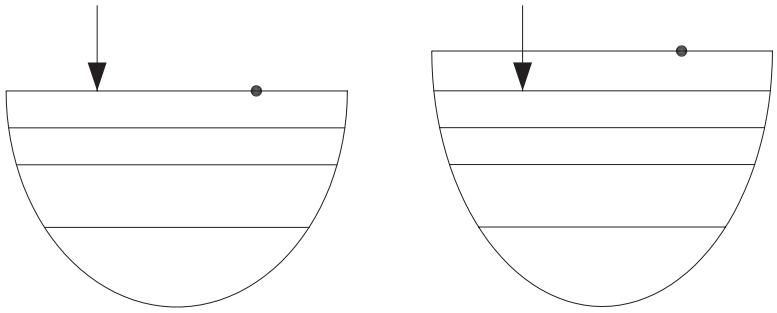

a. Soil model 1. b. Soil model 2.

Figure 4.22: (a) soil model 1 for the calculation of the soil's impedance and (b) soil model 2 for the calculation of the transfer functions.

between the layers 1 and 2 of the soil profile in table 4.7 (figure 4.22b). This case is referred to as model 2. The loading case is axisymmetric and only the in-plane components are relevant.

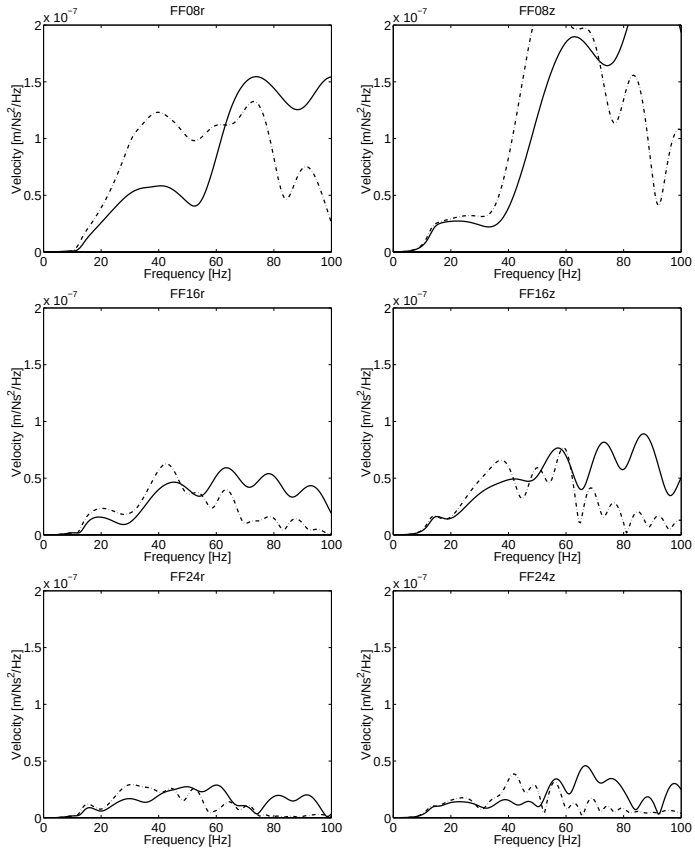


Figure 4.23: The frequency content of the radial (left hand side) and vertical (right hand side) component of the free field velocities at 8 m, 16 m and 24 m for a concentrated vertical pulse at the free surface of soil model 1 (solid line) and at the interface between the layers 1 and 2 of soil model 2 (dash-dotted line).

Figure 4.23 compares the frequency content of the free field velocities at 8 m, 16 m and 24 m. Each

signal is denoted by a label `FFij`, where `FF` denotes the free field, `i` the distance from the source and `j` the radial (r) or vertical (z) component. The radial and the vertical component generally have the same order of magnitude. The Green's functions exhibit a cut-off frequency at about 10 Hz. This phenomenon is related to the presence of the stiff halfspace at a depth of 8.20 m, under the relatively soft top layers. The shape of the Green's functions follows from the interference of waves and the reflection and transmission at the interfaces between the soil layers. Geometrical and material damping attenuate the signals at an increasing distance from the source. The attenuation at higher frequencies is relatively more important.

A comparison of the Green's functions shows that, below 60 Hz, the response is larger for the case where the weak top layer is present, while at higher frequencies, the response is larger in the absence of this layer. At limiting high frequencies, the thickness of the top layer is large with respect to the wavelength of the waves that are generated at the interface between the layers 1 and 2. Under these conditions, the displacements at the surface are small. For road traffic induced vibrations, the frequency range of interest is situated between 0 and 40 Hz. In this frequency range, there is a large difference for the radial component, while the difference is less important for the vertical component. In order to predict the horizontal component accurately, it is therefore important to account for the presence of the weak top layer. In the following, soil model 2 is used for the calculation of the transfer functions from the soil's tractions.

### 4.6.2 Time history and frequency content of the free field response

The free field velocities are calculated from the predicted axle loads (figures 4.17 and 4.18) and the transfer functions between the road and the soil by means of the Betti-Rayleigh reciprocal theorem. The time history of the free field response is obtained by means of a double inverse Fourier transform from the wavenumber $k_y$ to the longitudinal coordinate $y$ and from the circular frequency $\omega$ to the time $t$.

Figure 4.24 shows the predicted and measured time history of the components $v_x$, $v_y$ and $v_z$ of the velocity at 8 m, 16 m and 24 m from the centre of the road during a passage of the truck on the unevenness at a vehicle speed $v = 30\,\mathrm{km/h}$. All signals are shown on the same vertical scale so that the attenuation of the vibrations with distance can better be appreciated.

When the time of arrival and the amplitude of the ground vibrations are compared, it can be observed that wave propagation in the soil delays and attenuates the time signals for an increasing distance from the road axis. The time history is composed of the passage of the front axle and the rear axle on the unevenness, which are well separated in time. As expected, the components $v_x$ and $v_z$ of the free field velocities have the same order of magnitude, while $v_y$ is much smaller. The present case can be compared to the ideal case, where a vertical impact is applied at the origin of the reference system. This impact generates a Rayleigh wave at the soil's surface with an in-plane horizontal component $v_x$ and a vertical component $v_z$ of the same order of magnitude. In the present case, the impacts are not applied exactly at the origin and the in-plane component contributes to $v_y$ as well. The latter is also affected by the horizontal component of the interaction force between the road and the soil. These observations are confirmed by comments of Taniguchi and Sawada [99] on similar experiments.

The measured and predicted signals correspond well. The main difference is the duration of the transient signal that corresponds to the passage of the rear axle on the profile. This is due to the impact that follows the loss of contact between the rear axle and the road. This phenomenon is not taken into account with the linear vehicle model. The impact, however, does not generate vibration levels higher than those during the ascending of the rear axle on the profile.

The quality of the prediction varies with the distance $x$. At 8 m, the measured and predicted velocities

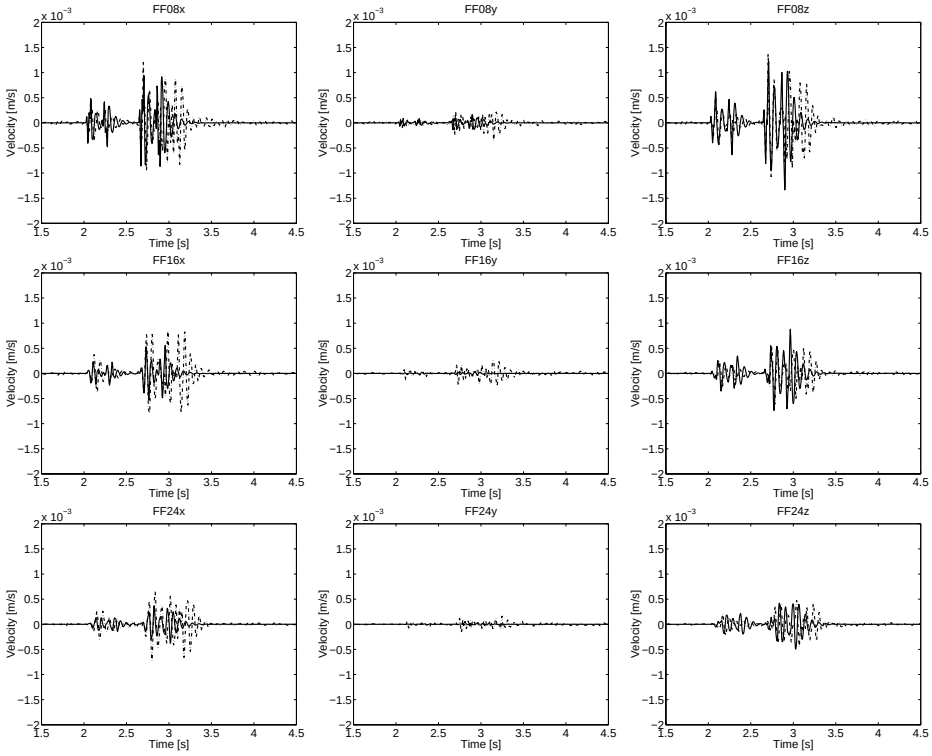


Figure 4.24: Time history of the predicted (solid line) and the measured (dash-dotted line) free field velocity at 8 m, 16 m and 24 m for a vehicle speed $v = 30\,\mathrm{km/h}$ (passage v30c).

$v_x$ and $v_z$ have the same order of magnitude. At 16 m and 24 m, the horizontal velocity $v_x$ is underestimated proportionally to the distance $x$. At all distances, $v_y$ is underestimated, which is due to the fact that the $y$-component of the interaction force between the vehicle and the road is not accounted for. Although not shown on these figures, the vertical velocity $v_z$ is also underestimated at 32 m, 40 m and 48 m from the centre of the road.

Figure 4.25 shows the predicted and measured frequency content of the free field velocity during the passage of the truck on the unevenness at a vehicle speed $v = 30\,\mathrm{km/h}$. The location of the dominant frequency between 10 Hz and 16 Hz is determined by the dominant frequency of the axle loads and the vertical resonance of the soil at this site. The spectrum is modulated at a wheel base frequency $f_w = v/w = 1.60$ Hz. The frequency content of the predicted and measured signal are mainly situated below 30 Hz and correspond well. Whereas the frequency content of $v_z$ is well predicted at all distances, $v_x$ and $v_y$ are underestimated at 16 m and 24 m. The underestimation of the frequency content is influenced by both the underestimation of the peak values and the larger duration of the measured signal.

Figures 4.26 and 4.27 show similar results for a vehicle speed $v$ equal to 58 km/h. A comparison of the time history shows that the time delay between the impact of the front and the rear axle decreases for higher vehicle speeds, while the PPV is larger at the highest vehicle speed. The quality of the prediction is good for $v_x$ and $v_z$, while the smaller component $v_y$ is underestimated. The mounting of the unevenness and the impact that takes place when the vehicle regains contact with the road generate vibrations with the same order of magnitude.

For an increasing vehicle speed, the frequency content shifts to higher frequencies. The dominant frequency is relatively unaffected and is situated between 10 Hz and 20 Hz. The wheel base frequency $f_w = v/w$ increases linearly with the vehicle speed $v$ and is equal to $f_w$= 3.10 Hz at $v = 58$ km/h.

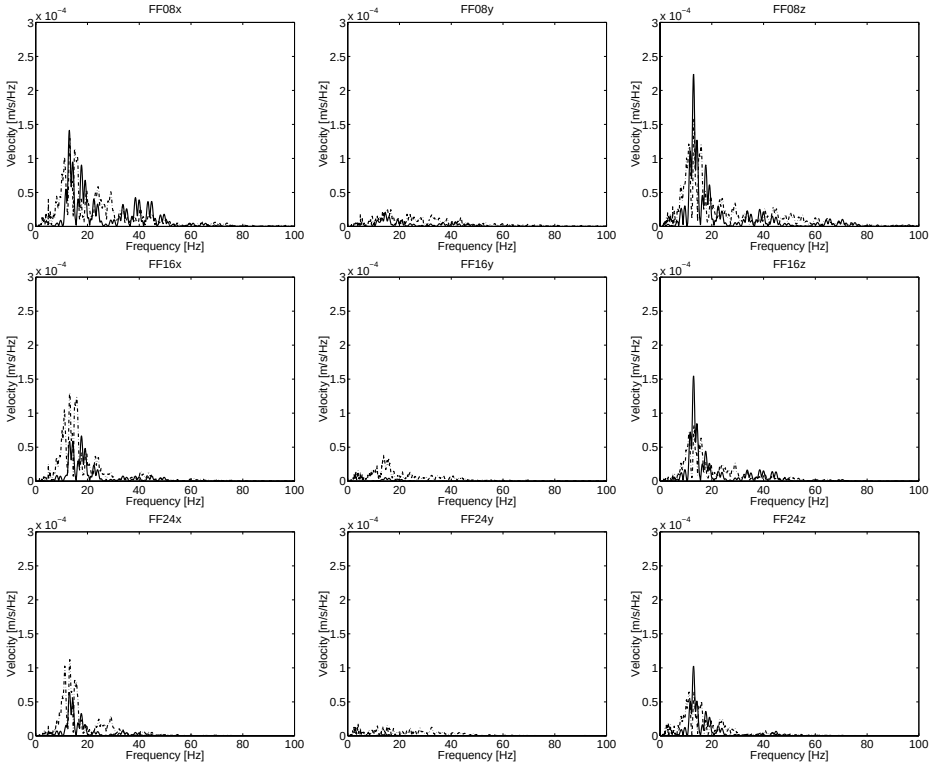


Figure 4.25: Frequency content of the predicted (solid line) and the measured (dash-dotted line) free field velocity at 8 m, 16 m and 24 m for a vehicle speed $v = 30\,\mathrm{km/h}$ (passage v30c).

The predicted and measured frequency content correspond well.

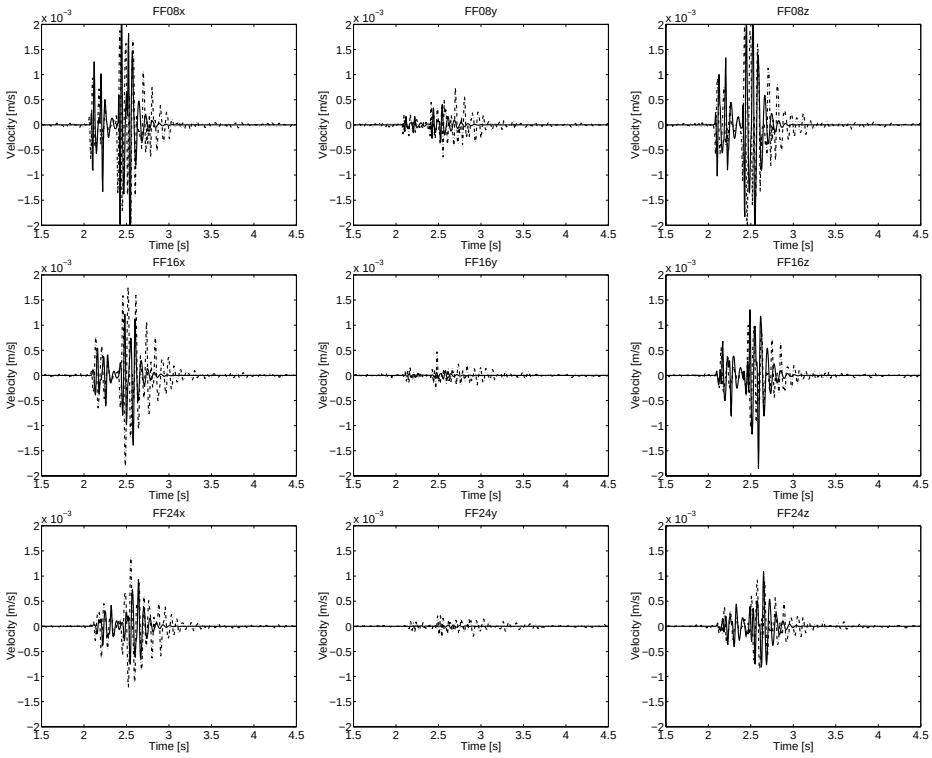


Figure 4.26: Time history of the predicted (solid line) and the measured (dash-dotted line) free field velocity at 8 m, 16 m and 24 m for a vehicle speed $v = 58\,\mathrm{km/h}$ (passage v60b).

### 4.6.3 Frequency content of the response for different vehicle speeds

Figure 4.28 shows the frequency content of the acceleration of the front and rear axle of the truck and the vertical free field velocity at 8 m and 24 m from the centre of the road for vehicle speeds $v = 30$ km/h, $v = 40$ km/h, $v = 49$ km/h and $v = 58$ km/h.

The figures illustrate how the shift of the frequency content with the vehicle speed $v$ is observed in both the measured and predicted response. The upper limit of the frequency content of the accelerations of the vehicle's axles shifts from 40 Hz for a vehicle speed $v = 30$ km/h upto 60 Hz for $v = 58$ km/h. The dominant frequency, however, does not shift significantly with the vehicle speed. The frequency content of the free field velocity at 8 m from the road's axis is very similar to the spectrum of the axle loads. The sharp cut-off frequency in the predicted frequency content at 10 Hz is not present in the measured frequency content. This is partly due to the fact that the frequency content of the acceleration of the rear axle is underestimated near 10 Hz. At 24 m, the contribution at higher frequencies is more attenuated due to material damping in the soil and the shift to higher frequencies is less pronounced. These figures show how the deviation between the measured and the predicted frequency content of the acceleration of the rear axle affects the quality of the prediction of the free field response.

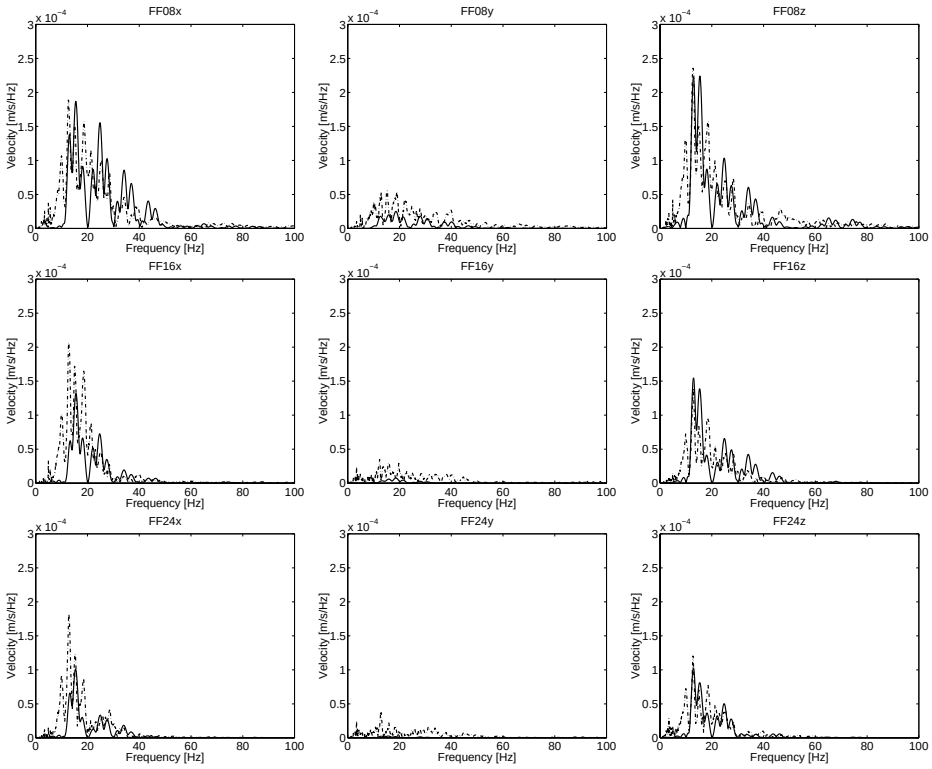


Figure 4.27: Frequency content of the predicted (solid line) and the measured (dash-dotted line) free field velocity at 8 m, 16 m and 24 m for a vehicle speed $v = 58\,\mathrm{km/h}$ (passage v60b).

### 4.6.4 Peak particle velocity of the free field response

Figure 4.29 shows the predicted and measured PPV as a function of the vehicle speed for all components at a distance $x$ of 8 m, 16 m and 24 m. Figure 4.30 shows, additionally, the PPV in the vertical direction at 32 m, 40 m and 48 m from the centre of the road. The vertical scale for the PPV is the same for all figures. These results confirm that the PPV in the $x$- and $z$-direction have the same order of magnitude, while the PPV in the $y$-direction is much smaller. The PPV generally increases with the vehicle speed. The highest vibration levels are generated by the passage of the rear axle on the unevenness. As a result, the PPV of the free field response and the peak acceleration vary in a similar way with the vehicle speed $v$.

Although the peak acceleration of the rear axle is underestimated at high vehicle speeds, the vertical PPV at 8 m and 16 m from the centre of the road is overestimated in the same case. At larger distances, the PPV is underestimated for all vehicle speeds, proportional to the distance $x$. The variation of the quality of the prediction with distance is due to an inadequate knowledge of the dynamic soil characteristics. The underestimation of the free field vibrations at larger distances from the source is probably due to an overestimation of the material damping in the top layer.

## 4.7 Conclusion

The simultaneous vehicle and free field response measurements at the 'de Hemptinne site' allow for a rigorous validation of the prediction model for free field traffic induced vibrations. The results provide a clear insight in the influence of the vehicle speed on both the vehicle's response and the free field

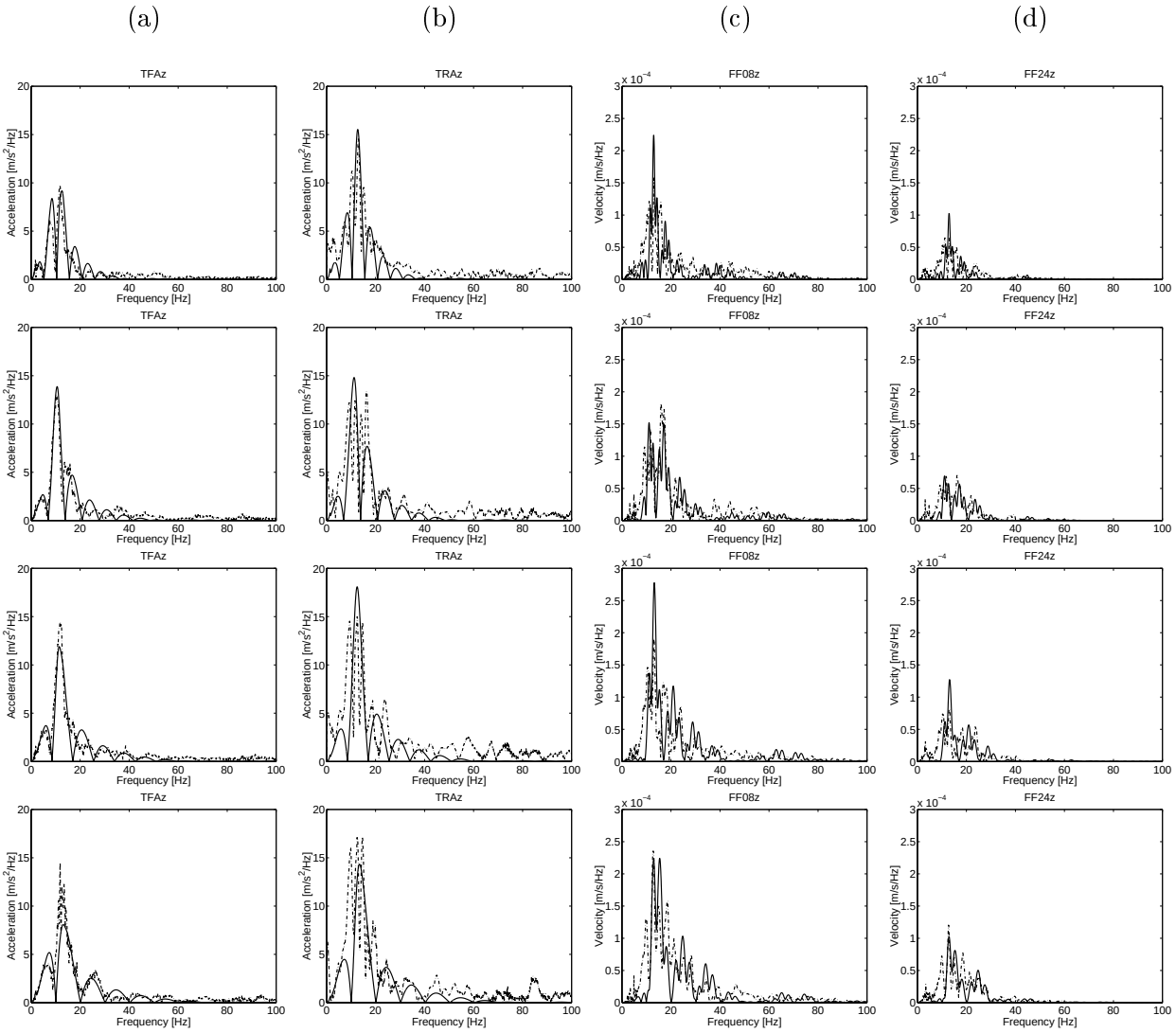


Figure 4.28: Frequency content of (a) the acceleration of the front and (b) the rear axle of the truck and frequency content of the vertical free field velocity at (c) 8 m and (d) 24 m from the center of the road for vehicle speeds $v = 30\,\mathrm{km/h}$, $v = 40\,\mathrm{km/h}$, $v = 49\,\mathrm{km/h}$ and $v = 58\,\mathrm{km/h}$ (from top to bottom).

response.

Elaborate tests have been performed to determine the parameters of the vehicle, the road and the soil in the numerical model. The parameters of a 4DOF vehicle model have been determined by means of dynamic system identification and vehicle weighings. A SASW test has been performed to identify the dynamic road characteristics. The soil's stratification and the dynamic soil characteristics are based on the complementary results of a SASW test and a SCPT. The material damping in the soil is estimated, based on the experimental observation that its value decreases with depth.

The variation of the vehicle's response and the free field response with the vehicle speed is determined by the frequency content of the unevenness and the vehicle FRF. The peak value of the reponse generally increases with the vehicle speed, while the frequency content shifts to higher frequencies. The dominant frequencies are relatively unaffected.

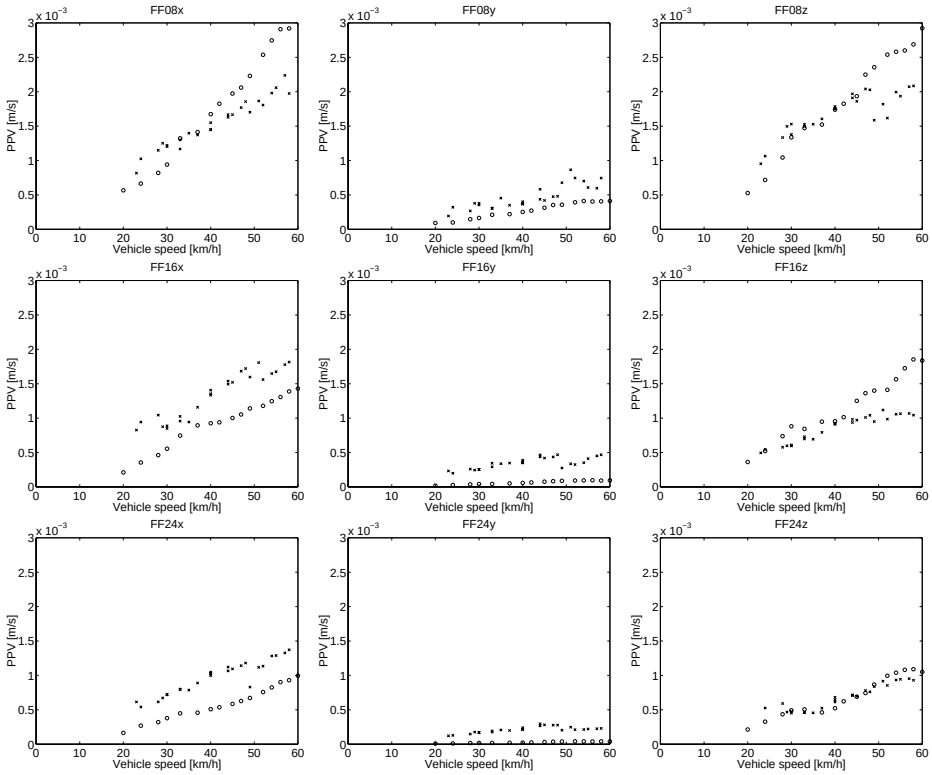


Figure 4.29: Predicted (circles) and measured (crosses) peak particle velocity of the free field response at a distance $x$ equal to 8 m, 16 m and 24 m as a function of the vehicle speed.

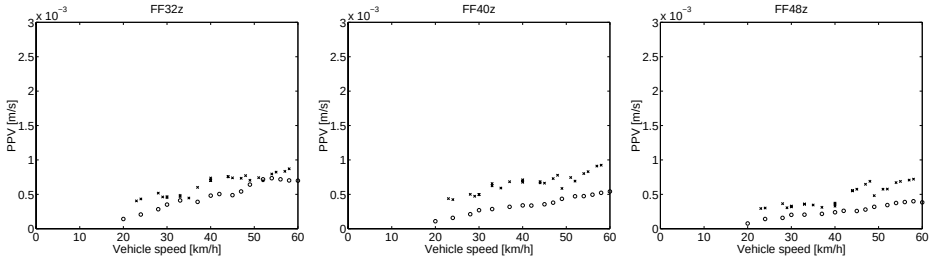


Figure 4.30: Predicted (circles) and measured (crosses) peak particle velocity of the vertical free field response at a distance $x$ equal to 32 m, 40 m and 48 m as a function of the vehicle speed.

A comparison between the predicted and measured response shows that the accelerations are well reproduced by the vehicle model. The most important difference is the loss of contact between the rear axle and the road, that cannot be predicted with the linear vehicle model.

The time histories of the ground vibrations illustrate that wave propagation in the soil delays and attenuates the free field vibrations. The present load case is similar to the one where a fixed vertical impact load is applied at the origin of the measurement line. The in-plane horizontal component $v_x$, perpendicular to the road, almost has the same order of magnitude as the vertical component $v_z$. The out-of-plane horizontal component $v_y$, parallel to the road, is much smaller. The results therefore demonstrate that the influence of the horizontal interaction force between the vehicle and the road is small. However, as only the vertical component of the interaction force between the vehicle and the road is taken into account for the prediction, the small $y$-component is underestimated. The velocity components $v_x$ and $v_z$ are well predicted with a ratio of 0.50 to 1.50 between the predicted and the

measured PPV. The quality of the prediction varies with the distance from the road's axis due to the lack of knowledge about the in situ material damping.

The results of the validation are very satisfactory and show that the presented numerical model reproduces the essential elements for the generation of traffic induced ground vibrations.

# Chapter 5

# Conclusions and further research

In this final report, the results of the DWTC research project MD/01/040 'Study of determining factors for traffic induced vibrations in buildings' (1 July 1998 - 30 June 2001) are discussed (task F.2 in the work programme). The main emphasis in this project went to the development and the use of a prediction model for free field road traffic induced vibrations.

In chapter 2, the numerical model is discussed. It is shown how the dynamic axle loads are calculated from the longitudinal road unevenness (task A.1) and the vehicle dynamics (task A.2). The road-soil interaction problem is solved with a substructure method where a beam model is used for the road (task A.3) and a boundary element method is used for the supporting soil (task A.4). The free field vibrations are calculated by means of the Betti-Rayleigh reciprocal theorem (task A.5). The high efficiency of the source module enables to perform calculations on a dense grid of receivers in the free field. Such results are required for the solution of the dynamic soil-structure interaction problem of a building, subjected to the incident wave field generated by the passage of a vehicle on an uneven road.

The results of the parametric study are presented in chapter 3 (task E.1) and translated into practical guidelines (task F.1). The height and the slope of traffic plateaus and bumps are of primary importance for the generation of traffic induced vibrations. The vibration levels that are generated by the passage of a vehicle on a joint in the road surface have the same order of magnitude as the vibration levels due to the passage on a traffic plateau with a much larger height. In the case of the joint in the road surface, the influence of the vehicle speed is small, while in the case of the plateau, its influence is large. In the case where a linear vehicle model is used for the prediction of the dynamic axle loads, the masses of the axles are more important than the gross vehicle weight. Heavy vehicles will therefore generate, both in laden and unladen state, the largest vibrations. Other important factors are the stiffness of the tyres and the damping of the suspension system. The parameters that are related to the road section do not play an important role. For a homogeneous soil, the vibration levels are inversely proportional to the soil's stiffness, while in the case of a stratified soil, the results are more complex. The soil's material damping is very important for the receivers that are at a large dimensionless distance from the source. An accurate determination of the soil's dynamic characteristics is of vital importance for the prediction of traffic induced vibrations.

Two measurement campaigns have been performed for the validation of the numerical model (task D.1). In chapter 4, the results of the second measurement campaign at the 'de Hemptinne' site in Heverlee (task C.1) are discussed. The truck's and the free field response have been measured simultaneously (task C.6) during the passage on an artificial unevenness (task C.3). The design of the unevenness has been supported by simulations with the numerical model (task B.1). Elaborate tests have been performed to determine the dynamic characteristics of the truck (task C.2), the road (task C.4) and the soil (task C.5). More than refining the existing models, the need is felt for a more

accurate determination of the dynamic soil characteristics.

The results have been presented at one national conference and seven international conferences. One paper has already been published in the journal 'Soil Dynamics and Earthquake Engineering', while four more journal papers have been accepted for publication. In appendix A, all publications are listed. Furthermore, the present work has lead to the achievement of a mobile data acquisition system with four measurement channels and a value of 25000 Euro within the frame of the 'Oros European University Millennium Award', [86, 87]. The extensive list of publications shows that the present research project has brought the Belgian research related to traffic induced vibrations to an international scientific level.

Compared to the project proposal, considerably more effort has been put in the development and the experimental validation of the source module. As a result, less attention has been spent to the development (tasks A.6 and A.7) and the validation (tasks C.7, C.8 and D.2) of a receiver module that enables the study of the determining factors for the vibrations in buildings (tasks B.2 and E.2). The dynamic interaction of the incident wave field and the structure have been studied, however, during a 6 months post-doctoral stay of Dr. Anita Uscilowska of the Institute of Mathematics of the Poznan University of Mathematics in Poznan (Polen) within the frame of the DWTC programme 'Scientific and Technology Cooperation with Central and Eastern Europe'. The results of this study are summarized in a research report [3].

# Bibliography


[1] G. R. Watts. Traffic induced vibrations in buildings. Research report 246, Transport and Road Research Laboratory, 1990.

[2] L. Lanoye and P. Bauweraerts. Trillingen langs betonwegen: stand van zaken. In *XIXe Belgisch Wegencongres*, Genval, September 2001. Belgische Wegenvereniging.

[3] A. Uscilowska, L. Pyl, and G. Degrande. Numerical modelling of traffic induced vibrations in buildings using a dynamic soil-structure interaction analysis. Technical Report BWM-2001-02, Department of Civil Engineering, Katholieke Universiteit Leuven, March 2001. DWTC Research Programme Sustainable Mobility, Research Project MD/01/040, Science and Technology Cooperation with Central and Eastern Europe. STWW Programme Technology and Economy Research Project IWT 000152.

[4] C.J. Baughan and D.J. Martin. Vibration nuisance from road traffic at fourteen residential sites. Laboratory report 1020, Transport and Road Research Laboratory, 1981.

[5] G.R. Watts. Vibration nuisance from road traffic, results of a 50 site survey. Laboratory report 1119, Transport and Road Research Laboratory, 1984.

[6] G. R. Watts. Traffic-induced ground-borne vibrations in dwellings. Research report 102, Transport and Road Research Laboratory, 1987.

[7] G.R. Watts and V.V. Krylov. Ground-borne vibrations generated by vehicles crossing road humps and speed control cushions. *Applied Acoustics*, 59:221–236, 2000.

[8] Transport Department of the Environment and UK Regions, London. Road humps and ground-borne vibrations. Technical report, Department of the Environment, Transport and Regions, London, UK, August 1996.

[9] Transport Department of the Environment and UK Regions, London. Road humps: discomfort, noise and ground-borne vibrations. Technical report, Department of the Environment, Transport and Regions, London, UK, October 2000.

[10] M.O. Al-Hunaidi and J.H. Rainer. Control of traffic induced vibration in buildings using vehicle suspension systems. *Soil Dynamics and Earthquake Engineering*, 15:245–254, 1996.

[11] M.O. Al-Hunaidi and M. Tremblay. Traffic induced building vibrations in Montréal. *Canadian Journal of Civil Engineering*, 24:736–753, 1997.

[12] G. R. Watts. Case studies of the effects of traffic-induced vibrations on heritage buildings. Research report 156, Transport and Road Research Laboratory, 1988.

[13] G. R. Watts. The effects of traffic-induced vibrations on heritage buildings, further case studies. Research report 207, Transport and Road Research Laboratory, 1989.

[14] G.R. Watts. Groundborne vibrations generated by HGVs - effects of vehicle, road and ground parameters. *Proceedings of the Institute of Acoustics*, 11(5):99–109, 1989.

[15] H.B. Sutherland. A study of the vibrations produced in structures by heavy vehicles. In *Proceedings of the 30th Annual Meeting of the Highway Research Board*, pages 406–419, 1950.

[16] D. Bocquenet, J. Girard, D. Le Houedec, and J. Picard. Les vibrations dues au trafic routier urbain: action sur l'environnement et méthodes d'isolation. Technical report, Annales de l'institut technique du bâtiment et des travaux publics, sommaire 355, novembre 1977.

[17] M. Bata. Effects on buildings of vibrations caused by traffic. *Building Science*, 6:221–246, 1971.

[18] J.H.A. Crocket. Some practical aspects of vibration in civil engineering. In *Proceedings of the symposium on vibration in civil engineering*, pages 253–271, 1965.

[19] H.J. Heller. Bauwerksetzungen bei sandigen Untergrund infolge von Erschütterungen durch Bahnverkehr. *Bauplanung - Bautechnik*, 35(2):56–61, 1981.

[20] G. R. Watts. Traffic vibration and building damage, TRRL papers presented at acoustics '87. Research report 146, Transport and Road Research Laboratory, 1988.

[21] M.E. House. Traffic induced vibrations in buildings. *The Highway Engineer*, February:6–15, 1973.

[22] G.R. Watts. The generation and propagation of vibration in various soils produced by the dynamic loading of road pavements. *Journal of Sound and Vibration*, 156(2):191–206, 1992.

[23] J. Jakobsen. Transmission of ground vibrations in buildings. *Journal of Low Frequency Noise and Vibration*, 8(3):75–80, 1989.

[24] P. Vanhonacker and E. Hemerijckx. Design of low noise embedded tracks for new tram line to Zwijndrecht. In P. Sas, editor, *Proceedings ISMA 23, Noise and Vibration Engineering*, volume III, pages 1587–1593, Leuven, Belgium, September 1998.

[25] R.C. Hill. Traffic induced vibrations in buildings. *Noise and vibration control worldwide*, 11(5):176–180, 1980.

[26] J.R. Block and B.P. Temple. The influence of vehicle and track condition on the generation of railway ground borne vibration. In *7th International Congress on Sound and Vibration*, Garmisch-Partenkirchen, Germany, July 2000.

[27] D. Cebon. Interaction between heavy vehicles and roads. SP-951, L. Ray Buckendale Lecture, SAE, 1993.

[28] T.D. Gillespie, S.M. Karamihas, M.W. Sayers, M.A. Nasim, W. Hansen, N. Ehsan, and D. Cebon. Effects of heavy-vehicle characteristics on pavement response and performance. Technical Report 353, NCHRP, Transportation Research Board, Washington D.C., 1993.

[29] M.S.A. Hardy and D. Cebon. Response of continuous pavements to moving dynamic loads. *Journal of the Engineering Mechanics Division, Proceedings of the ASCE*, 119(9):1762–1780, 1993.

[30] G. Lombaert and G. Degrande. Study of determining factors for traffic induced vibrations in buildings. First biannual report BWM-1999-01, Department of Civil Engineering, Katholieke Universiteit Leuven, January 1999. DWTC Research Programme Sustainable Mobility, Research Project MD/01/040.

[31] M. S. Mamlouk. General outlook of pavement and vehicle dynamics. *Journal of Transportation Engineering, Proceedings of the ASCE*, 123(6):515–517, 1997.

[32] Markow M.J. Analyzing the interaction between dynamic vehicle loads and highway pavements. *Transportation research record TRB*, 1196:161–169, 1988.

[33] H.E.M. Hunt. Modelling of road vehicles for calculation of traffic-induced ground vibrations. *Journal of Sound and Vibration*, 144(1):41–51, 1991.

[34] C. Liu and R. Herman. Road profiles, vehicle dynamics, and human judgement of serviceability of roads: spectral frequency domain analysis. *Journal of Transportation Engineering, Proceedings of the ASCE*, 124(2):106–111, 1998.

[35] N.L. Mulcahy, V.A. Pulmano, and R.W. Traill-Nash. Vehicle properties for bridge loading studies. *International association for bridge and structural engineering*, P-65/83(3):153–167, 1983.

[36] Eurocode on Actions Part 12. *Traffic loads on road bridges.* Working-group 5: Definition of dynamic impact factors, 1991.

[37] M.M. El Madany. Technical note: an analytical investigation of isolation systems for cab ride. *Computers and Structures*, 27(5):679–688, 1987.

[38] C.J. Dodds and J.D. Robson. The description of road surface roughness. *Journal of Sound and Vibration*, 31(2):175–183, 1973.

[39] ISO8608. *Mechanical vibration, road surface profiles.* Reporting of measured data, 1991.

[40] H. Hao and T. C. Ang. Analytical modelling of traffic-induced ground vibrations. *Journal of the Engineering Mechanics Division, Proceedings of the ASCE*, 124(8):921–928, 1998.

[41] M.O. Al-Hunaidi and J.H. Rainer. Remedial measures for traffic induced vibrations at a residential site. Part 1: Field tests. *Canadian Acoustics/Acoustique Canadiennne*, 19(1):3–13, 1991.

[42] W. Gerritsen, P. Waarts, and L. Pelgröm. Prevention of environmental vibrations from uneven roads and sleeping policemen. In P. Pereira and V. Miranda, editors, *International Symposium on the Environmental Impact of Road Pavement Unevenness*, pages 275–282, Porto, Portugal, March 1999.

[43] P. Hölscher. Omgevingstrillingen door wegverkeer over drempels. In *Wegenbouwkundige werkdagen 1998*, pages 457–465, Doornwerth, June 1998. E.CROW.

[44] L.J.W. Pelgrom, P.H. Waarts, and P.M. Wennink. Trillingen in gebouwen door onvlakheid van de weg. In *Wegenbouwkundige werkdagen 1998*, pages 423–433, Doornwerth, June 1998. E.CROW.

[45] G.E. Westera. Verkeerdrempels en trillingen. In *Geluid en trillingen in Nederland*, Rotterdam, Nederland, November 2000.

[46] R.G. Payton. An application of the dynamic Betti-Rayleigh reciprocal theorem to moving point loads in elastic media. *Quarterly of Applied Mathematics*, 21(4):299–313, 1964.

[47] G. Müller. Bewegter Streifenlast auf dem elastisch-isotropen Halbraum. *Acustica*, 72:47–53, 1990.

[48] G. Müller and H. Huber. Dynamische Bodeansprachungen infolgte bewegter Lasten. *Bauingenieur*, 66:375–380, 1991.

[49] F.C.P. de Barros and J.E. Luco. Moving Green's functions for a layered visco-elastic half-space. Technical report, Department of Applied Mechanics and Engineering Sciences of the University of California, La Jolla, 1992.

[50] F.C.P. de Barros and J.E. Luco. Response of a layered viscoelastic half-space to a moving point load. *Wave Motion*, 19:189–210, 1994.

[51] R.W. Clough and J. Penzien. *Dynamics of structures*. McGraw-Hill, New York, second edition, 1993.

[52] D. Aubry, D. Clouteau, and G. Bonnet. Modelling of wave propagation due to fixed or mobile dynamic sources. In N. Chouw and G. Schmid, editors, *Workshop Wave '94, Wave propagation and Reduction of Vibrations*, pages 109–121, Rühr University, Bochum, Germany, December 1994.

[53] M. S. Mamlouk and T.G. Davies. Elasto-dynamic analysis of pavement deflections. *Journal of Transportation Engineering, Proceedings of the ASCE*, 110(6):536–550, 1984.

[54] M.S.A. Hardy and D. Cebon. Importance of speed and frequency in flexible pavement response. *Journal of the Engineering Mechanics Division, Proceedings of the ASCE*, 120(3):463–482, 1994.

[55] W.M.G. Courage. Bronmodel wegverkeer. Technical Report 93-CON-R0056-04, Nederlandse Organisatie voor Toegepast Natuurwetenschappelijk Onderzoek, September 1993.

[56] H.E.M. Hunt. Stochastic modelling of traffic-induced ground vibration. *Journal of Sound and Vibration*, 144(1):53–70, 1991.

[57] N.N. Prognosemodel trillingshinder. Technical Report 95-2, Civieltechnisch Centrum Uitvoering Research en Regelgeving, February 1995.

[58] J.C. Wambold, L.E. Defrain, R.R. Hegmon, K. Macghee, J. Reichert, and E.B. Spangler. State of the art of measurement and analysis of road roughness. *Transportation research record*, 836:21–29, 1981.

[59] W. Alaerts, G. Lombaert, and G. Degrande. Trillingsmetingen in het gebouw van Orda-B N.V. aan de Interleuvenlaan te Leuven. Internal report BWM-1999-09, Department of Civil Engineering, Katholieke Universiteit Leuven, October 1999.

[60] G. Degrande, G. Lombaert, and J. Maeck. Trillingsmetingen in een woning Genthof 48 te Brugge. Internal report BWM-1999-02, Department of Civil Engineering, Katholieke Universiteit Leuven, March 1999.

[61] G. Lombaert, W. Alaerts, and G. Degrande. Trillingsmetingen in een woning aan de Vilvoordsebaan 59a te Winksele. Internal report BWM-1999-07, Department of Civil Engineering, Katholieke Universiteit Leuven, August 1999. DWTC Research Programme Sustainable Mobility, Research Project MD/01/040.

[62] G. Descornet and M. Boulet. Road surface design and tyre/road surface interactions. In *Tyretech '95*. Rapra Technology Ltd. and European Rubber Journal, 1995.

[63] M.O. Al-Hunaidi, W. Guan, and J. Nicks. Building vibrations and dynamic pavement loads induced by transit buses. *Soil Dynamics and Earthquake Engineering*, 19:435–453, 2000.

[64] G. Lombaert and G. Degrande. Study of determining factors for traffic induced vibrations in buildings. Second biannual report BWM-1999-04, Department of Civil Engineering, Katholieke Universiteit Leuven, July 1999. DWTC Research Programme Sustainable Mobility, Research Project MD/01/040.

[65] S. Drosner. *Beitrag zur Berechnung der dynamischen Beanspruchung von Brücken unter Verkehrslasten*. PhD thesis, Stahlbau RWTH Aachen, Aachen, Germany, 1989.

[66] K. Knothe and S.L. Grassie. Modelling of railway track and vehicle/track interaction at high frequencies. *Vehicle Systems Dynamics*, 22: 209–262, 1993.

[67] S. Müller and K. Knothe. Stability of wheelset track dynamics for high frequencies. *Archive of Applied Mechanics*, 67:353–363, 1997.

[68] N.N. Vehicle model for a DAF FT95 truck and trailer. Private communication, DAF, 1999.

[69] K.-H. Chu, V.K. Garg, and L.D. Chaman. Railway-bridge impact: simplified train and bridge model. *Journal of the Structural Division, Proceedings of the ASCE*, 105(ST9):1823–1844, 1979.

[70] K. Henchi, M. Fafard, and M. Talbot. Analyse dynamique de l'interaction pont-vehicules pour les ponts routiers. I. Aspects numériques. *Canadian Journal of Civil Engineering*, 25(1):161–173, 1998.

[71] T.-L. Wang, Huang D., and M. Shahawy. Dynamic response of multigirder bridges. *Journal of Structural Engineering*, 118(8):2222–2238, 1992.

[72] R. Dobry and G. Gazetas. Dynamic response of arbitrarily shaped foundations. *Journal of Geotechnical Engineering, Proceedings of the ASCE*, 112:109–135, 1986.

[73] J. Lysmer and F. Richart. Dynamic response of footings to vertical loading. *Journal of the Soil Mechanics and Foundation Division, Proceedings of the ASCE*, 92(SM1 or EM5):65–91, 1966.

[74] G.F. Miller and H. Pursey. The field and radiation impedance of mechanical radiators on the free surface of a semi-infinite isotropic solid. *Proceedings of the Royal Society*, A223:521–541, 1954.

[75] L.T. Wheeler and E. Sternberg. Some theorems in classical elastodynamics. *Archive for Rational Mechanics and Analysis*, 31:51–90, 1968.

[76] G. Lombaert, G. Degrande, and D. Clouteau. Deterministic and stochastic modelling of free field traffic induced vibrations. In P. Pereira and V. Miranda, editors, *International Symposium on the Environmental Impact of Road Pavement Unevenness*, pages 163–176, Porto, Portugal, March 1999.

[77] P. Flandrin. Separability, positivity and minimum uncertainty in time-frequency distributions. *Journal of mathematical physics*, 39(8):4016–4040, 1998.

[78] D.E. Newland. *An introduction to random vibrations, spectral & wavelet analysis*. Longman Scientific & Technical, Essex, England, 1994.

[79] J. Ville. Théorie et applications de la notion de signal analytique. *Cables et Transmission*, 2:61–74, 1948.

[80] E.P. Wigner. On the quantum correction for thermodynamic equilibrium. *Physical Review*, 40:749–759, 1932.

[81] J. Dom. Trillingshinder ten gevolge van wegverkeer: een parameterstudie. Master's thesis, Department of Civil Engineering, Katholieke Universiteit Leuven, 2000.

[82] Koninklijk Besluit 9 oktober 1998. *Koninklijk Besluit tot bepaling van de vereisten voor de aanleg van verhoogde inrichtingen op de openbare weg en van de technische voorschriften waaraan die moeten voldoen*. Belgisch Staatsblad 28 oktober, 1998.

[83] G. Lombaert, G. Degrande, and D. Clouteau. The influence of the soil stratification on free field traffic induced vibrations. *Archive of Applied Mechanics*, 2001. Accepted for publication.

[84] G. Lombaert, A. Teughels, and G. Degrande. Trillingsmetingen in het vrije veld op de Daf proefbaan te Sint-Oedenrode. Internal report BWM-2000-01, Department of Civil Engineering, Katholieke Universiteit Leuven, January 2000. DWTC Programma Duurzame Mobiliteit, Project MD/01/040.

[85] G. Lombaert and G. Degrande. Experimental validation of a numerical prediction model for free field traffic induced vibrations by in situ experiments. *Soil Dynamics and Earthquake Engineering*, 21(6):485–497, 2001.

[86] G. Lombaert and G. Degrande. Vehicle response measurements as a validation tool for a prediction model for free field traffic induced vibrations. Report BWM-2000-08, Department of Civil Engineering, Katholieke Universiteit Leuven, September 2000. DWTC Programme Sustainable Mobility, Project MD/01/040, OROS European University Millennium Award.

[87] G. Lombaert and G. Degrande. Vehicle response measurements as a validation tool for a prediction model for free field traffic induced vibrations. Final report. Report BWM-2001-05, Department of Civil Engineering, Katholieke Universiteit Leuven, March 2001. DWTC Programme Sustainable Mobility, Project MD/01/040, OROS European University Millennium Award.

[88] G. Lombaert and G. Degrande. Determination of the dynamic soil characteristics with the SASW method at the "de Hemptinne" site in Heverlee. Report BWM-2000-11, Department of Civil Engineering, Katholieke Universiteit Leuven, September 2000. DWTC Programme Sustainable Mobility, Project MD/01/040, OROS European University Millennium Award.

[89] G. Lombaert and G. Degrande. Studie van determinerende factoren voor trillingshinder ten gevolge van wegverkeer. Derde halfjaarlijkse rapport BWM-2000-03, Department of Civil Engineering, Katholieke Universiteit Leuven, February 2000. DWTC Programma Duurzame Mobiliteit, Project MD/01/040.

[90] B. Peeters and G. De Roeck. Reference based stochastic subspace identification in civil engineering. *Inverse Problems in Engineering*, 8(1):47–74, 2000.

[91] B. Peeters and G. De Roeck. Reference-based stochastic subspace identification for output-only modal analysis. *Mechanical Systems and Signal Processing*, 13(6):855–878, 1999.

[92] W. Haegeman. Verslag en interpretatie van de SASW proef en seismische sonderingen op de terreinen van het militair domein te Heverlee. XI.0045, Laboratorium voor Grondmechanica, Universiteit Gent, 2001.

[93] D.K. Watson and R.K.N.D. Rajapakse. Seasonal variation in material properties of a flexible pavement. *Canadian Journal of Civil Engineering*, 27(1):44–54, 2000.

[94] N.N. *Handleiding voor het dimensioneren van wegen met een bitumineuze verharding*, volume O.C.W.-A 49/83. 1983.

[95] W. Dewulf, G. Degrande, and G. De Roeck. Practical application of the SASW method. Internal report 37-BWM-03, Department of Civil Engineering, Katholieke Universiteit Leuven, June 1995. IWONL research grant CI 1/4-7672/091.

[96] S. Nazarian and M.R. Desai. Automated surface wave method: field testing. *Journal of Geotechnical Engineering, Proceedings of the ASCE*, 119(7):1094–1111, 1993.

[97] G. Degrande and W. Alaerts. Spectral version 7.01: a direct stiffness formulation for harmonic and transient wave propagation in layered dry, saturated and unsaturated poroelastic media. User's manual, Department of Civil Engineering, Katholieke Universiteit Leuven, 1999.

[98] G. Lombaert and G. Degrande. Studie van determinerende factoren voor trillingshinder ten gevolge van wegverkeer. Vierde halfjaarlijkse rapport BWM-2000-07, Department of Civil Engineering, Katholieke Universiteit Leuven, February 2000. DWTC Programma Duurzame Mobiliteit, Project MD/01/040.

[99] E. Taniguchi and K. Sawada. Attenuation with distance of traffic-induced vibrations. *Soils and Foundations*, 19(2):15–28, 1979.

[100] G. Lombaert, G. Degrande, and D. Clouteau. Numerical modelling of free field traffic induced vibrations. *Soil Dynamics and Earthquake Engineering*, 19(7):473–488, 2000.

[101] D. Clouteau, G. Degrande, and G. Lombaert. Numerical modelling of traffic induced vibrations. *Meccanica*, 2001. Accepted for publication.

[102] G. Degrande and G. Lombaert. An efficient formulation of Krylov's prediction model for train induced vibrations based on the dynamic reciprocity theorem. *Journal of the Acoustical Society of America*, 2001. Accepted for publication.

[103] D. Clouteau, G. Degrande, and G. Lombaert. Some theoretical and numerical tools to model traffic induced vibrations. In N. Chouw and G. Schmid, editors, *Proceedings of the International Workshop Wave 2000, Wave propagation, Moving load, Vibration reduction*, pages 13–27, Ruhr University, Germany, December 2000. A.A. Balkema, Rotterdam.

[104] G. Degrande and G. Lombaert. High-speed train induced free field vibrations: in situ measurements and numerical modelling. In N. Chouw and G. Schmid, editors, *Proceedings of the International Workshop Wave 2000, Wave propagation, Moving load, Vibration reduction*, pages 29–41, Ruhr University Bochum, Germany, December 2000. A.A. Balkema, Rotterdam.

[105] G. Lombaert and G. Degrande. An efficient formulation of Krylov's prediction model for train induced vibrations based on the dynamic reciprocity theorem. In G. Guidati, H. Hunt, H. Heller, and A. Heiss, editors, *7th International Congress on Sound and Vibration*, pages 2671–2678, Garmisch-Partenkirchen, Germany, July 2000.

[106] G. Lombaert and G. Degrande. A dynamic soil-structure interaction approach for the modelling of free field traffic induced vibrations. In G. Guidati, H. Hunt, H. Heller, and A. Heiss, editors, *7th International Congress on Sound and Vibration*, pages 2773–2780, Garmisch-Partenkirchen, Germany, July 2000.

[107] G. Lombaert, G. Degrande, and D. Clouteau. Road traffic induced free field vibrations: numerical modelling and in situ measurements. In N. Chouw and G. Schmid, editors, *Proceedings of the International Workshop Wave 2000, Wave propagation, Moving load, Vibration reduction*, pages 195–207, Ruhr University Bochum, Germany, December 2000. A.A. Balkema, Rotterdam.

[108] G. Lombaert and G. Degrande. Numerical modelling and in situ measurements of free field traffic induced vibrations. In *4th International Symposium SURF 2000, Pavement Surface Characteristics*, pages 451–461, Nantes, France, May 2000. PIARC, World Road Association.

[109] G. Lombaert and G. Degrande. The validation of a numerical prediction model for free field traffic induced vibrations by in situ measurements. In P. Sas and D. Moens, editors, *Proceedings ISMA 25, Noise and vibration Engineering*, pages 357–364, Leuven, Belgium, September 2000.

[110] G. Lombaert and G. Degrande. The modelling of free field traffic induced vibrations by means of a dynamic soil-structure interaction approach. In *4th International Conference on Recent Advances in Geotechnical Earthquake Engineering and Soil Dynamics*, San Diego, CA, USA, March 2001.

[111] G. Lombaert and G. Degrande. Studie van determinerende factoren voor trillingshinder in gebouwen. In *Het Transport: het Milieu en de Veiligheid*, Brussels, Belgium, March 2000. Federale Diensten voor Wetenschappelijke, Technische en Culturele Aangelegenheden.

[112] G. Degrande and G. Lombaert. Studie van determinerende factoren voor trillingshinder ten gevolge van wegverkeer. Aanvangsrapport BWM-1998-05, Department of Civil Engineering, Katholieke Universiteit Leuven, September 1998. DWTC Programma Duurzame Mobiliteit, Onderzoeksproject MD/01/040.

[113] G. Degrande and G. Lombaert. Study of determining factors for traffic induced vibrations in buildings. Summary report BWM-2000-10, Department of Civil Engineering, Katholieke Universiteit Leuven, September 2000. DWTC Research Programme Sustainable Mobility, Research Project MD/01/040.

[114] W. Dewulf, G. Lombaert, and G. Degrande. Bepaling van de dynamische grondkarakteristieken met behulp van de SASW methode op de DAF proefbaan te Sint-Oedenrode. Internal report BWM-2000-02, Department of Civil Engineering, Katholieke Universiteit Leuven, February 2000. DWTC Programma Duurzame Mobiliteit, Project MD/01/040.

[115] G. Lombaert and G. Degrande. Studie van determinerende factoren voor trillingshinder ten gevolge van wegverkeer. Vijfde halfjaarlijkse rapport BWM-2001-01, Department of Civil Engineering, Katholieke Universiteit Leuven, January 2001. DWTC Programma Duurzame Mobiliteit, Project MD/01/040.

[116] G. Lombaert and G. Degrande. Study of determining factors for traffic induced vibrations in buildings. Final report. Report BWM-2001-06, Department of Civil Engineering, Katholieke Universiteit Leuven, July 2001. DWTC Programme Sustainable Mobility, Project MD/01/040.

# Appendix A

# Publications

The developments within the frame of the DWTC project MD/01/040 have lead to a large number of publications. In the following, the reports and the publications that result from the DWTC research project MD/01/040 'Study of determining factors for traffic induced vibrations in buildings' are listed. A total of 15 research reports, 10 conference papers and 5 journal papers have been written.

# International journal papers


[1] G. Lombaert, G. Degrande, and D. Clouteau. Numerical modelling of free field traffic induced vibrations. *Soil Dynamics and Earthquake Engineering*, 19(7):473–488, 2000.

[2] D. Clouteau, G. Degrande, and G. Lombaert. Numerical modelling of traffic induced vibrations. *Meccanica*, 2001. Accepted for publication.

[3] G. Degrande and G. Lombaert. An efficient formulation of Krylov's prediction model for train induced vibrations based on the dynamic reciprocity theorem. *Journal of the Acoustical Society of America*, 2001. Accepted for publication.

[4] G. Lombaert and G. Degrande. Experimental validation of a numerical prediction model for free field traffic induced vibrations by in situ experiments. *Soil Dynamics and Earthquake Engineering*, 21(6):485–497, 2001.

[5] G. Lombaert, G. Degrande, and D. Clouteau. The influence of the soil stratification on free field traffic induced vibrations. *Archive of Applied Mechanics*, 2001. Accepted for publication.

# Conference papers


[1] G. Lombaert, G. Degrande, and D. Clouteau. Deterministic and stochastic modelling of free field traffic induced vibrations. In P. Pereira and V. Miranda, editors, *International Symposium on the Environmental Impact of Road Pavement Unevenness*, pages 163–176, Porto, Portugal, March 1999.

[2] D. Clouteau, G. Degrande, and G. Lombaert. Some theoretical and numerical tools to model traffic induced vibrations. In N. Chouw and G. Schmid, editors, *Proceedings of the International Workshop Wave 2000, Wave propagation, Moving load, Vibration reduction*, pages 13–27, Ruhr University, Germany, December 2000. A.A. Balkema, Rotterdam.

[3] G. Degrande and G. Lombaert. High-speed train induced free field vibrations: in situ measurements and numerical modelling. In N. Chouw and G. Schmid, editors, *Proceedings of the International Workshop Wave 2000, Wave propagation, Moving load, Vibration reduction*, pages 29–41, Ruhr University Bochum, Germany, December 2000. A.A. Balkema, Rotterdam.

[4] G. Lombaert and G. Degrande. An efficient formulation of Krylov's prediction model for train induced vibrations based on the dynamic reciprocity theorem. In G. Guidati, H. Hunt, H. Heller, and A. Heiss, editors, *7th International Congress on Sound and Vibration*, pages 2671–2678, Garmisch-Partenkirchen, Germany, July 2000.

[5] G. Lombaert and G. Degrande. A dynamic soil-structure interaction approach for the modelling of free field traffic induced vibrations. In G. Guidati, H. Hunt, H. Heller, and A. Heiss, editors, *7th International Congress on Sound and Vibration*, pages 2773–2780, Garmisch-Partenkirchen, Germany, July 2000.

[6] G. Lombaert, G. Degrande, and D. Clouteau. Road traffic induced free field vibrations: numerical modelling and in situ measurements. In N. Chouw and G. Schmid, editors, *Proceedings of the International Workshop Wave 2000, Wave propagation, Moving load, Vibration reduction*, pages 195–207, Ruhr University Bochum, Germany, December 2000. A.A. Balkema, Rotterdam.

[7] G. Lombaert and G. Degrande. Numerical modelling and in situ measurements of free field traffic induced vibrations. In *4th International Symposium SURF 2000, Pavement Surface Characteristics*, pages 451–461, Nantes, France, May 2000. PIARC, World Road Association.

[8] G. Lombaert and G. Degrande. The validation of a numerical prediction model for free field traffic induced vibrations by in situ measurements. In P. Sas and D. Moens, editors, *Proceedings ISMA 25, Noise and vibration Engineering*, pages 357–364, Leuven, Belgium, September 2000.

[9] G. Lombaert and G. Degrande. The modelling of free field traffic induced vibrations by means of a dynamic soil-structure interaction approach. In *4th International Conference on Recent Advances in Geotechnical Earthquake Engineering and Soil Dynamics*, San Diego, CA, USA, March 2001.

[10] G. Lombaert and G. Degrande. Studie van determinerende factoren voor trillingshinder in gebouwen. In *Het Transport: het Milieu en de Veiligheid*, Brussels, Belgium, March 2000. Federale Diensten voor Wetenschappelijke, Technische en Culturele Aangelegenheden.

# Research reports


[1] G. Degrande and G. Lombaert. Studie van determinerende factoren voor trillingshinder ten gevolge van wegverkeer. Aanvangsrapport BWM-1998-05, Department of Civil Engineering, Katholieke Universiteit Leuven, September 1998. DWTC Programma Duurzame Mobiliteit, Onderzoeksproject MD/01/040.

[2] G. Lombaert and G. Degrande. Study of determining factors for traffic induced vibrations in buildings. First biannual report BWM-1999-01, Department of Civil Engineering, Katholieke Universiteit Leuven, January 1999. DWTC Research Programme Sustainable Mobility, Research Project MD/01/040.

[3] G. Lombaert and G. Degrande. Study of determining factors for traffic induced vibrations in buildings. Second biannual report BWM-1999-04, Department of Civil Engineering, Katholieke Universiteit Leuven, July 1999. DWTC Research Programme Sustainable Mobility, Research Project MD/01/040.

[4] G. Lombaert, W. Alaerts, and G. Degrande. Trillingsmetingen in een woning aan de Vilvoordsebaan 59a te Winksele. Internal report BWM-1999-07, Department of Civil Engineering, Katholieke Universiteit Leuven, August 1999. DWTC Research Programme Sustainable Mobility, Research Project MD/01/040.

[5] G. Degrande and G. Lombaert. Study of determining factors for traffic induced vibrations in buildings. Summary report BWM-2000-10, Department of Civil Engineering, Katholieke Universiteit Leuven, September 2000. DWTC Research Programme Sustainable Mobility, Research Project MD/01/040.

[6] W. Dewulf, G. Lombaert, and G. Degrande. Bepaling van de dynamische grondkarakteristieken met behulp van de SASW methode op de DAF proefbaan te Sint-Oedenrode. Internal report BWM-2000-02, Department of Civil Engineering, Katholieke Universiteit Leuven, February 2000. DWTC Programma Duurzame Mobiliteit, Project MD/01/040.

[7] G. Lombaert, A. Teughels, and G. Degrande. Trillingsmetingen in het vrije veld op de Daf proefbaan te Sint-Oedenrode. Internal report BWM-2000-01, Department of Civil Engineering, Katholieke Universiteit Leuven, January 2000. DWTC Programma Duurzame Mobiliteit, Project MD/01/040.

[8] G. Lombaert and G. Degrande. Studie van determinerende factoren voor trillingshinder ten gevolge van wegverkeer. Derde halfjaarlijkse rapport BWM-2000-03, Department of Civil Engineering, Katholieke Universiteit Leuven, February 2000. DWTC Programma Duurzame Mobiliteit, Project MD/01/040.

[9] G. Lombaert and G. Degrande. Studie van determinerende factoren voor trillingshinder ten gevolge van wegverkeer. Vierde halfjaarlijkse rapport BWM-2000-07, Department of Civil En-

gineering, Katholieke Universiteit Leuven, February 2000. DWTC Programma Duurzame Mobiliteit, Project MD/01/040.

[10] G. Lombaert and G. Degrande. Vehicle response measurements as a validation tool for a prediction model for free field traffic induced vibrations. Report BWM-2000-08, Department of Civil Engineering, Katholieke Universiteit Leuven, September 2000. DWTC Programme Sustainable Mobility, Project MD/01/040, OROS European University Millennium Award.

[11] G. Lombaert and G. Degrande. Determination of the dynamic soil characteristics with the SASW method at the "de Hemptinne" site in Heverlee. Report BWM-2000-11, Department of Civil Engineering, Katholieke Universiteit Leuven, September 2000. DWTC Programme Sustainable Mobility, Project MD/01/040, OROS European University Millennium Award.

[12] G. Lombaert and G. Degrande. Studie van determinerende factoren voor trillingshinder ten gevolge van wegverkeer. Vijfde halfjaarlijkse rapport BWM-2001-01, Department of Civil Engineering, Katholieke Universiteit Leuven, January 2001. DWTC Programma Duurzame Mobiliteit, Project MD/01/040.

[13] G. Lombaert and G. Degrande. Vehicle response measurements as a validation tool for a prediction model for free field traffic induced vibrations. Final report. Report BWM-2001-05, Department of Civil Engineering, Katholieke Universiteit Leuven, March 2001. DWTC Programme Sustainable Mobility, Project MD/01/040, OROS European University Millennium Award.

[14] G. Lombaert and G. Degrande. Study of determining factors for traffic induced vibrations in buildings. Final report. Report BWM-2001-06, Department of Civil Engineering, Katholieke Universiteit Leuven, July 2001. DWTC Programme Sustainable Mobility, Project MD/01/040.

[15] A. Uscilowska, L. Pyl, and G. Degrande. Numerical modelling of traffic induced vibrations in buildings using a dynamic soil-structure interaction analysis. Technical Report BWM-2001-02, Department of Civil Engineering, Katholieke Universiteit Leuven, March 2001. DWTC Research Programme Sustainable Mobility, Research Project MD/01/040 Science and Technology Cooperation with Central and Eastern Europe STWW Programme Technology and Economy Research Project IWT 000152.